Probing nanoscale forces of nature in fluid

From pneumatics to biomechanics

Roslon, I.E.

DOI
10.4233/uuid:5c3cc4c4-f38a-43ce-851a-8f758769171a

Publication date
2023

Document Version
Final published version

Citation (APA)
Roslon, I. E. (2023). *Probing nanoscale forces of nature in fluid: From pneumatics to biomechanics*. [Dissertation (TU Delft), Delft University of Technology]. https://doi.org/10.4233/uuid:5c3cc4c4-f38a-43ce-851a-8f758769171a

PROBING NANOSCALE FORCES OF NATURE IN FLUID

FROM PNEUMATICS TO BIOMECHANICS

PROBING NANOSCALE FORCES OF NATURE IN FLUID

FROM PNEUMATICS TO BIOMECHANICS

Proefschrift

ter verkrijging van de graad van doctor
aan de Technische Universiteit Delft,
op gezag van de Rector Magnificus prof. dr. ir. T.H.J.J. van der Hagen,
voorzitter van het College voor Promoties,
in het openbaar te verdedigen op donderdag 21 September 2023 om 12:30 uur

door

Ireneusz Eugeniusz ROSŁOŃ

Ingenieur in Toegepaste Natuurkunde,
Technische Universiteit Delft, Nederland,
geboren te Velsen, Nederland.

Dit proefschrift is goedgekeurd door de

promotor:	Prof. dr. P.G. Steeneken
promotor:	Dr. F. Alijani

Samenstelling promotiecommissie:

Rector Magnificus	Voorzitter
Prof. dr. P. G. Steeneken	TU Delft
Dr. F. Alijani	TU Delft
Onafhankelijke leden:	
Prof. dr. J. Tamayo	IMN - CSIC, Madrid
Prof. dr. U. Staufer	TU Delft
Prof. dr. ir. H. S. J. van der Zant	TU Delft
Prof. dr. C. Dekker	TU Delft
Overig lid:	
Dr. G. Longo	ISM - CNR, Rome

Keywords: nanomechanics, 2D materials, antibiotic susceptibility testing, bacterial sensing, gas sensing

Printed by: Proefschriftmaken

Cover art: A bacterium playing the nanodrums while floating in fluid. Generated with DALL·E by I. E. Rosłoń.

ISBN 978-94-6384-475-8

An electronic version of this dissertation is available at
http://repository.tudelft.nl/.

Contents

SUMMARY

Nanoscale forces from natural phenomena are hard to measure. It is not insofar that we lack the ability to measure such small forces. On the contrary, nanotechnology offers a wide spectrum of techniques that allow us to sense at this scale. However, many natural systems are subject to a noisy environment or need to be surrounded by liquid to maintain their shape and function - which on its own account drastically limits the achievable sensitivity of measurement methods.

Graphene, a single layer of carbon atoms, shows extreme strength and flexibility at the 2D limit of miniaturization. We have rationalized that graphene membranes are a perfect candidate to play the role of flexible support for detection of minute forces in nature, that are often hidden behind the veil of the environmental noise. Graphene owes its suitability to its ultimately thin nature, its low stiffness but simultaneously high tensile strength that prevents it from breaking under high tension. The limits of sensitivity can now be pushed further so that nanoscale forces can be measured in liquid - from pneumatic forces of attoliter volumes of gas, down to the level of single living bacteria.

In this thesis the motion of graphene membranes is studied under the influence of external forces. The motion is detected by a reflectometry setup devised for the study of optomechanical systems immersed in fluid. In Chapter 1 an introduction is given to the topic and the experimental methods are described. In Chapter 2, gases are pumped through a milled nanometer orifices in graphene membranes. The pneumatic interaction and the escape of the gasses through the nanometer scale pores is studied. In Chapter 3, we probe the nanomotion of single bacteria adhered to the surface of a graphene drum. The interplay between the processes occurring at cellular level and the motion of the suspended graphene with bacteria deposited on top is investigated. In Chapter 4, we study the signals obtained when motile bacteria cross a focused laser beam. We also find, that we can enhance the signal by patterning substrates to localise the bacteria close to the laser spot. Finally, in Chapter 5 we give prospects and outlooks, both on application of graphene drum enabled nanomotion sensing for rapid drug susceptibility testing, as well as on further research that might offer new insights into biological processes that can be held accountable for bacteria nanomotion. Furthermore, we discuss developments that would allow for further improvement of the current measurement system that go beyond bacterial sensing.

SAMENVATTING

Krachten op nanoschaal van natuurfenomenen zijn moeilijk te meten. Het is niet dat we niet over het vermogen beschikken om zulke kleine krachten te meten. Integendeel, nanotechnologie biedt een breed spectrum aan technieken waarmee op deze schaal kan worden gevoeld. Veel natuurlijke systemen zijn echter onderhevig aan een ordeloze omgeving, of moeten worden omringd door een vloeistof om zo hun vorm en functie te behouden - wat op zichzelf de haalbare gevoeligheid van de meetmethoden drastisch beperkt.

Grafeen, een enkele laag koolstofatomen, vertoont extreme sterkte en flexibiliteit waarbij het zich op de 2D-limiet van miniaturisatie bevindt. Wij beschouwen grafeenmembranen als een perfecte kandidaat om de rol te spelen van flexibele receptor van de miniscule krachten in de natuur, die vaak verborgen gaan achter de sluier van het omgevingslawaai, vanwege de ultiem dunne aard van grafeen, zijn lage stijfheid maar tegelijkertijd hoge treksterkte die voorkomt dat het materiaal breekt onder hoge spanning. De grenzen van gevoeligheid kunnen verder worden verlegd om de detectie van dergelijke krachten op nanoschaal en in vloeistof mogelijk te maken - van pneumatische krachten van attoliter gasvolumes tot op het niveau van waarneming van enkele levende bacteriën.

In dit proefschrift wordt de beweging van grafeenmembranen bestudeerd onder invloed van externe krachten. De beweging wordt gedetecteerd door een lasergebaseerde interferometrische opstelling. In Hoofdstuk 1 wordt een inleiding gegeven op het onderwerp en worden de experimentele methoden beschreven. In Hoofdstuk 2 worden gassen door een nanometeropening in grafeenmembranen gepompt. De pneumatische interactie met de membranen en de ontsnappingssnelheid van de gassen door de poriën wordt bestudeerd. In Hoofdstuk 3 onderzoeken we de nanobeweging van enkele bacteriën die aan een membraan vastzitten. Het samenspel tussen de processen die op cellulair niveau plaatsvinden en de beweging van de vrijhangende grafeen membranen met daarop geplaatste bacteriën wordt onderzocht. In Hoofdstuk 4 bestuderen we de signalen die worden verkregen wanneer beweeglijke bacteriën een gefocusseerde laserstraal passeren. We ontdekken ook dat het verkregen signaal kan worden verbeterd door substraten met een patroon te gebruiken om de bacteriën dicht bij de lasersfocus te lokaliseren. Ten slotte geven we in Hoofdstuk 5 vooruitzichten voor de toepassing van nanobewegingssensoriek op basis van grafeen membranen voor het snel testen van de effectiviteit van medicijnen, als ook voor onderzoek dat nieuwe inzichten kan bieden in biologische processen in een bacterie die verantwoordelijk gehouden kunnen worden voor de nanobewegingen. Daarnaast benoemen we ontwikkelingen die verbeteringen van huidige meetsystemen mogelijk maken en die verder gaan dan bacteriële detectie.

PREFACE

THE ability to explain complex problems to another person is very fulfilling. It turns out to be very hard, as well. If one can explain something to another person, it shows that one truly understands the topic. In my view, research revolves around explaining complex phenomena in the most facile way possible.

Having a deep understanding of the topic does not do the trick by itself. A necessary element of performing research, or any kind of work, is enthusiasm. It lets you think of new ideas, explore topics you do not know yet and makes you continue when things do not work out as planned. It is essential for delivering at the best of your possibilities and being content with the work. And above all, enthusiasm is contagious. This is what I want to share with anyone who picked up this book: my enthusiasm for the topic.

Ireneusz Eugeniusz Rosłoń
Eindhoven, August 2023

1

1

Introduction

Timendi causa est nescire;
Ignorance is the cause of fear.

Lucius Seneca

Ignorance is doing the same thing over and over again;
Yet expecting different results.

Albert Einstein

Science looks to push forward boundaries, either it be into the small or the big. We try to look on smaller scale and see the building blocks of the world. Already the ancient Greek philosopher Leucippus speculated that matter might consist of inseparable particles [1], each of which he called in Greek an 'a-tomos'. It took thousands of years to find conclusive evidence that matter is indeed built from atoms, and we have formed a comprehensive theory describing how these atoms interact with each other. Since the discovery of graphene in 2004 [2], the chapter of 2D materials has been opened. These materials consist of only one layer of carbon atoms, and therefore they are the 2D counterpart of the inseparable atom. This family of materials is indeed very promising and has shown a plethora of outstanding properties and interesting physics. Among these materials, graphene stands out for its unprecedented strength, meaning it can withstand high forces and undergo high stretching without breaking or tearing.

1

GRAPHENE possesses a variety of thrilling properties, and an outstanding effort has been undertaken in the past 15 years to benefit from those in practical applications. Examples have been shown where this material has allowed us to obtain fundamental understanding of physics at nanoscale and explore new concepts of sensors. Despite all the efforts, the step to actually manufacture costumer products has proven to be more difficult than it might have seemed. Yet, the unique mechanical, electrical and optical properties of graphene bear a great promise for realizing novel sensors [3]. Though graphene is just one layer of carbon atoms, it is the strongest material known, with its Young's Modulus and tensile strength being around 1 TPa and 100-130 GPa, respectively [4, 5]. These astonishing characteristics have been utilized in the field of Nanoelectromechanical Systems (NEMS) and Microelectromechanical Systems (MEMS) and can be found in readily available applications such as pressure sensors [6], biosensors [7] and photo-detectors [8].

In this chapter an introduction is given to graphene drums, which are nanomechanical systems created by suspending a layer of graphene over a cavity. Such device geometry is used in chapters 1 and 2 for sensing. We give a brief introduction to the measurement setup that has been used to collect the data focusing on the mechanisms that are in common to all chapters. In each chapter specific alterations have been made to the setup to suit specific needs, which are discussed in further detail in the corresponding chapter. We also introduce the methods used for manufacturing chips, transferring graphene and inspecting the samples. Finally, we summarize the frame and scope of this thesis and the contents of each of the following chapters.

1.1. NANOMECHANICAL GRAPHENE DRUMS

A graphene membrane consists of a sheet of graphene suspended over a cavity, forming a microscale counterpart of a drum, a configuration first reported in 2008 [9]. This drum can be actuated such that it moves out of plane, by optothermal [10] and pneumatic forces [11], a gate potential or mechanical vibrations [12–14]. Once actuated harmonically, the deflection of the drum can be approximated by a second order driven harmonic oscillator. Due to its low out-of-plane stiffness and high in-plane strength, a graphene drum subjected to an out-of-plane force can stretch readily and deflect a few nanometer already at pN forces. Such deflections can be measured more easily than the pN force by itself, which on its part gives a window of opportunity to potential applications.

Coincidently, as the size of nanoelectromechanical systems shrinks, the interaction with sources of thermomechanical noise grow in relative amplitude [15]. Conducting experiments in cryogenic temperatures on devices with higher Q-factors helps pushing sensitivity further, but puts constrains on the application space of these devices. For a wide practical applications one cannot rely solely on low temperatures and has to face describing interactions with the environment at higher temperatures.

The environment serves not only as a source of thermomechanical noise to the membrane, but can also contain microscale objects that will alter or influence the dynamics of the graphene. Microscale objects placed near or on a suspended graphene membrane can be a source of unexplained or unexpected fluctuations in the graphene membrane, as they can alter the deflection shapes or attenuate the motion of the membrane. It is interesting to investigate such interactions, as they form new ways to probe nanoscale

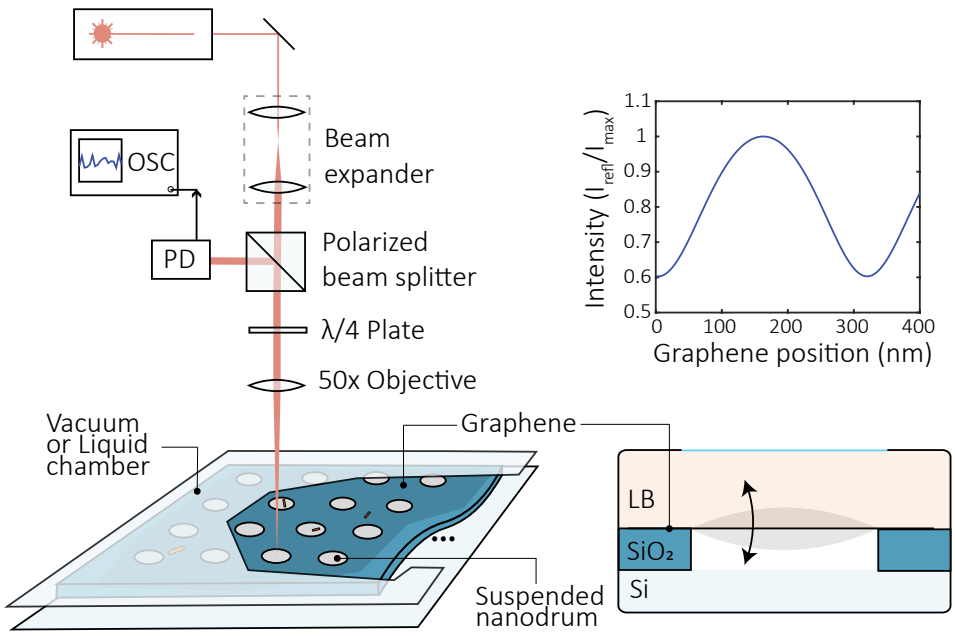

Figure 1.1: *Layout of the laser reflectometry setup used in this thesis. A helium neon laser with wavelength $\lambda = 632.8$ nm is passed through a beam expander, polarized beam splitter, $\lambda/4$ waveplate and 50X objective to be focused on the sample substrate. The reflected light is polarized such that the beam splitter only reflects the returning light onto the photodiode. The intensity of the reflected light depends on the position of the graphene, as the suspended layer passes through the standing wave created at the reflective surface. Thus the motion of the membrane can be observed by tracking the changes in the intensity of the reflected light.*

forces in nature.

In this work, graphene membranes are studied together with their interactions with nanoscale objects, leveraging the special characteristics of such systems and looking at noise enabled dynamics. Noise is indeed usually treated as a detrimental nuisance, and methods are looked after to cancel, attenuate or disregard sources of noise. But in some cases, noise can improve the information that we get from a sample – or it might be exactly the thing we are looking for. This holds for example for the tiny motion arising from live specimens [16, 17]. The following chapters describe the microscopic methods needed for observing such signals.

1.2. OPTICAL READ-OUT OF NANOMECHANICAL MOTION

The motion of graphene drums can be measured by reflectometric read-out and analyzed to compare with theoretical understanding [18]. The reflectometry setup accommodates lasers for actuation and readout of nanomechanical motion of 2D materials [19]. Figure 1.1 shows the basic configuration of the setup using a red helium neon laser for readout. The readout laser is focused on the sample substrate by an 50X objective and the reflected light intensity is measured with a photodiode. When an additional

actuation or measurement point is needed, lasers with other wavelengths can be combined into the same path with a dichroic mirror. See Chapter 2 for more details on this approach, specifically Figure 2.1. Lasers are available at powers of up to 50 mW. Samples can be placed in a vacuum chamber or measured in liquid using a cuvette.

The sample stage can be operated manually or moved by programmable electronic nanometer positioners (Attocube ACS5050) to position the sample with respect to the laser. A flip-in beamsplitter is used to image the sample with a camera under Köhler illumination. For resonant measurements, such as in Chapter 2, a homodyne detection scheme is employed to obtain the high frequency component of the signal [20]. For nanomotion experiments like in Chapters 3 and 4, the reflected light intensity is directly read from an oscilloscope. In some measurements, for instance in Chapter 4, the setup was adapted for fluorescent microscopy to locate bacteria. Each chapter of this thesis contains a separate section describing in detail the exact configuration of the measurement setup used, which was necessary for the experiments in that chapter.

1.3. FABRICATION OF CHIPS WITH CAVITIES

The graphene drums discussed in this work are suspended over cavities etched in silicon chips. The chips are prepared from 500 micron thick silicon (Si) wafers with a 285nm thick silicon dioxide (SiO_2) thermally grown oxide layer [21]. The chips are taken from the wafer by cutting with a diamond blade into smaller pieces (e.g. 5x5 mm^2). The workflow for preparation of these chips is as follows:

1. Electron beam lithography of spinned CSAR 62 (AR-P 6200-18) photoresist. Chips are developed by submersion in pentyl acetate (60'), followed by submersion in a mixture of methyl isobutyl ketone (60') and isopropyl alcohol (MIBK:IPA) and washed in IPA to obtain a pattern in the photoresist. During all steps, the liquid is agitated manually.

2. Dry Reactive Ion Etching (RIE) is used to etch the pattern in SiO_2 with the resist serving as the mask and the silicon as the stop layer. Typically, a recipe is used that employs a mixture of CHF_3 (25 sccm) and Ar (2.5 sccm) at a voltage bias of 150 V resulting in a silicon oxide etching rate of 10 nm/min.

3. Optionally: to obtain cavities deeper than 285 nm, etching is continued into the silicon employing a mixture of SF_6 (13.5 sccm) and O_2 (13.5 sccm). This results into smooth sidewalls in the silicon at an etching rate of 135 nm/min.

4. Resist is stripped with PRS-3000 and the chips are oxide plasma treated for at least 15 minutes at a power of 200W to clean residues.

1.4. GRAPHENE TRANSFER

To create suspended drums, graphene needs to be transfered onto the prepared Si/SiO_2 cavities. Mechanically exfoliated graphene is used to prepare the samples with PDMS assisted transfer. Alternatively, CVD grown graphene is transferred onto the chips when a large number of suspended drums on one chip is needed. For exfoliation, "Scotch Magic" tape is used to peel graphene from natural crystals of graphite. Once the graphite

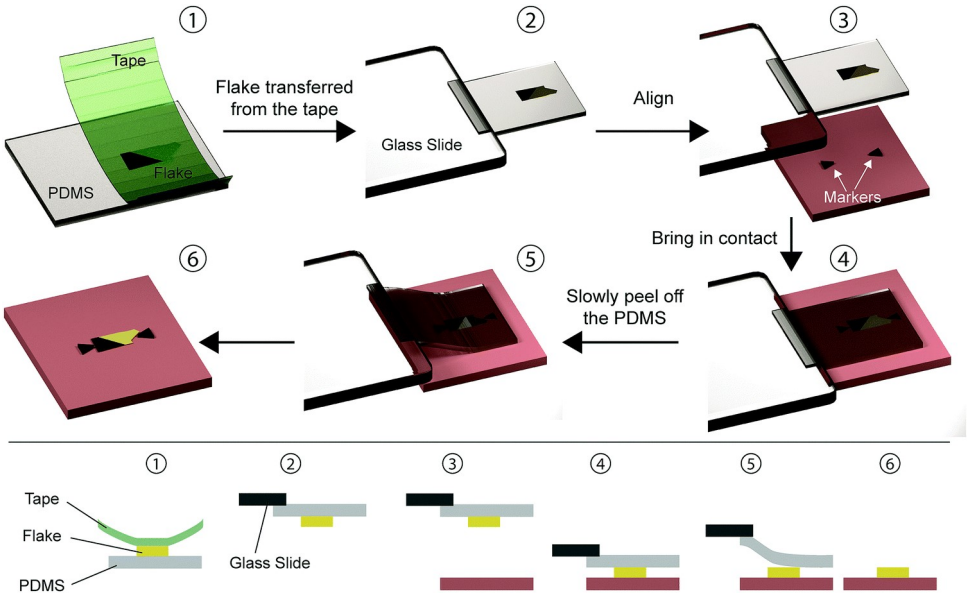

Figure 1.2: *Transfer steps required for PDMS assisted dry transfer of graphene. Graphene is exfoliated using Skotch tape and transferred upon a PDMS covered glass slide (1-2). The PDMS is aligned with the cavities on the chip and brought in contact (3-4). Then, the slide is slowly retracted to release the graphene (5-6). Steps 4 and 5 can be aided by heating and cooling the sample, such that the transfer is controlled smoothly by the thermal expansion and shrinking of the substrate material. Figure reproduced from [22] with permission.*

is sufficiently thinned down, the graphene flakes are transferred onto a square of polymethylsiloxane PDMS on a microscope slide [22]. The PDMS serves as a transparent, half-sticky carrier for the graphene flakes. Best quality flakes (thin and large) are obtained by using fresh PDMS (not older than a month), and by slightly pressing the skotch tape before decisively peeling off the tape. Some of the graphene stays on the PDMS. A microscope equipped with micromanipulators is used to position the graphene flake over the cavities, press and slowly remove the PDMS stamp. The graphene remains attached to the SiO_2 surface and creates a suspended drum. These process steps are depicted in Figure 1.2.

1.5. SAMPLE CHARACTERIZATION

After the membranes are fabricated, they are characterized using either optical microscopy, scanning electron microscopy (SEM) or atomic force microscopy (AFM). Optical microscopy is typically performed on a Keyence VHX-7000 digital microscope, where suspended drums appear slightly darker than collapsed drums. Some samples were taken to the FEI FIB/SEM Helios G4 CX combination for inspection, electron beam induced deposition (EBID) and focused ion beam milling (FIB). Atomic force microscopy is performed to find height profiles and contaminants on samples.

1.6. FRAME AND SCOPE

This research is carried out as a part of the ENIGMA project (Exploring Nonlinear dynamics in Graphene Nanomechanical systems) funded by the European Research Council, aiming at providing a full understanding of the nonlinearities of graphene membranes, improving characterization methods and developing **better and more sensitive devices**. For clarity, and to prevent misunderstanding, I highlighted the part that this thesis is mainly about: developing sensing methods and devices that are in some sense better or more sensitive than state-of-the-art. To achieve this, I study how forces in nature impact the motion of graphene drums. In particular, there are three topics that can be distinguished in this thesis:

1. Graphene drums subjected to opto-thermal heating and pneumatic effects
2. Bacterial nanomotion sensing with graphene drums
3. Optical interaction of laser light with bacteria

Various scientific questions are posed in the course of this research, of which some are answered completely, and some partially. Can the escape speed of gases be determined by the mechanical motion of graphene? Can different biological processes be distinguished via the motion of atomically thin membranes? In which way does the position of a bacterium affect motion transduction and interaction with the probing laser light? We developed new optical methods to investigate these questions. We also analyzed the data and conceived new theoretical models to describe our findings. The results advance our understanding of these topics, and the knowledge that was acquired in writing this thesis paves the way for future applications.

1.7. OUTLINE OF THE THESIS

In chapter 2, the motion of graphene membranes with nanoscale pores in gaseous environment is discussed. The suspended graphene membranes are perforated by holes ranging in size from 10-400 nm such that the gasses trapped inside the cavity can escape when pressurized. A model is developed that describes the motion of a graphene drum subject to photothermal and pneumatic actuation. It is shown that these devices can be used to probe the flow of gas through nanoscopic channels.

In chapter 3, I probe the motion of single bacteria that are attached to the graphene surface in a liquid environment. The nanomotion from the live bacteria sets the graphene drums in motion by mechanical actuation. We find that activity of the bacterial flagella is a main contributor to the nanomotion we observe, although it is not the only cause of the nanomotion. Furthermore, we show that it is possible to distinguish susceptible from resistant bacteria within one hour of administrating the antibiotic by observing changes in nanomotion amplitude.

In chapter 4, the optical properties of bacteria near a reflective surface are measured and analyzed. We find that bacteria near a reflective surface can be observed better than freely swimming in bulk, and that they can be localized using traps that are only a few hundred nm deep. It is further found that a bacterium crossing a tightly focused laser beam absorbs and diffracts up to 20% of the incoming laser light.

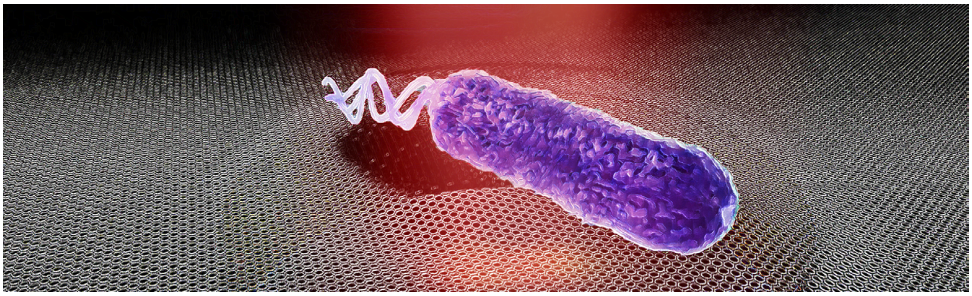

Figure 1.3: *Artist's impression of a bacterium on a graphene drum illuminated by the light of a red laser.*

At last, chapter 5 contains an outlook on opportunities and challenges for application of graphene drums as rapid antibiotic sesnsitivity testing devices. It discusses important developments to be made to increase the throughput and sensitivity of tests with this platform. The chapter is concluded with a perspective on the possible applications beyond bacterial sensing.

BIBLIOGRAPHY

[1] B. Pullman, *The atom in the history of human thought*. Oxford University Press, USA, 2001.

[2] S. Novoselov, "The nobel prize in physics 2010 honours two scientists, who have made the decisive contributions to this development.," 2010.

[3] D. G. Papageorgiou, I. A. Kinloch, and R. J. Young, "Mechanical properties of graphene and graphene-based nanocomposites," *Progress in materials science*, vol. 90, pp. 75–127, 2017.

[4] G.-H. Lee, R. C. Cooper, S. J. An, S. Lee, A. Van Der Zande, N. Petrone, A. G. Hammerberg, C. Lee, B. Crawford, W. Oliver, *et al.*, "High-strength chemical-vapor–deposited graphene and grain boundaries," *science*, vol. 340, no. 6136, pp. 1073–1076, 2013.

[5] Y. Hwangbo, C.-K. Lee, S.-M. Kim, J.-H. Kim, K.-S. Kim, B. Jang, H.-J. Lee, S.-K. Lee, S.-S. Kim, J.-H. Ahn, *et al.*, "Fracture characteristics of monolayer CVD-graphene," *Scientific reports*, vol. 4, no. 1, p. 4439, 2014.

[6] H. Tian, Y. Shu, X.-F. Wang, M. A. Mohammad, Z. Bie, Q.-Y. Xie, C. Li, W.-T. Mi, Y. Yang, and T.-L. Ren, "A graphene-based resistive pressure sensor with record-high sensitivity in a wide pressure range," *Scientific reports*, vol. 5, no. 1, p. 8603, 2015.

[7] Z. Wang, Z. Hao, C. Yang, H. Wang, C. Huang, X. Zhao, and Y. Pan, "Ultra-sensitive and rapid screening of acute myocardial infarction using 3D-affinity graphene biosensor," *Cell Reports Physical Science*, vol. 3, no. 5, p. 100855, 2022.

[8] W. Liu, J. Lv, L. Peng, H. Guo, C. Liu, Y. Liu, W. Li, L. Li, L. Liu, P. Wang, *et al.*, "Graphene charge-injection photodetectors," *Nature Electronics*, vol. 5, no. 5, pp. 281–288, 2022.

[9] A. K. Geim, "Graphene: status and prospects," *science*, vol. 324, no. 5934, pp. 1530–1534, 2009.

[10] H. Liu, S. B. Basuvalingam, S. Lodha, A. A. Bol, H. S. van der Zant, P. G. Steeneken, and G. Verbiest, "Nanomechanical resonators fabricated by atomic layer deposition on suspended 2D materials," *arXiv preprint arXiv:2212.08449*, 2022.

[11] D. Davidovikj, D. Bouwmeester, H. S. Van Der Zant, and P. G. Steeneken, "Graphene gas pumps," *2D Materials*, vol. 5, no. 3, p. 031009, 2018.

[12] M. Lee, J. R. Renshof, K. J. van Zeggeren, M. J. Houmes, E. Lesne, M. Šiškins, T. C. van Thiel, R. H. Guis, M. R. van Blankenstein, G. J. Verbiest, *et al.*, "Ultrathin piezoelectric resonators based on graphene and free-standing single-crystal BaTiO3," *Advanced Materials*, vol. 34, no. 44, p. 2204630, 2022.

[13] H. Liu, M. Lee, M. Šiškins, H. van der Zant, P. Steeneken, and G. Verbiest, "Tension tuning of sound and heat transport in graphene," *arXiv preprint arXiv:2204.06877*, 2022.

[14] M. Šiškins, E. Sokolovskaya, M. Lee, S. Mañas-Valero, D. Davidovikj, H. S. Van Der Zant, and P. G. Steeneken, "Tunable strong coupling of mechanical resonance between spatially separated feps3 nanodrums," *Nano Letters*, vol. 22, no. 1, pp. 36–42, 2021.

[15] H. C. Postma, I. Kozinsky, A. Husain, and M. Roukes, "Dynamic range of nanotube- and nanowire-based electromechanical systems," *Applied Physics Letters*, vol. 86, no. 22, p. 223105, 2005.

[16] I. E. Rosłoń, A. Japaridze, P. G. Steeneken, C. Dekker, and F. Alijani, "Probing nanomotion of single bacteria with graphene drums," *Nature Nanotechnology*, vol. 17, no. 6, pp. 637–642, 2022.

[17] G. Longo, L. Alonso-Sarduy, L. M. Rio, A. Bizzini, A. Trampuz, J. Notz, G. Dietler, and S. Kasas, "Rapid detection of bacterial resistance to antibiotics using afm cantilevers as nanomechanical sensors," *Nature nanotechnology*, vol. 8, no. 7, pp. 522–526, 2013.

[18] D. Davidovikj, J. J. Slim, S. J. Cartamil-Bueno, H. S. Van Der Zant, P. G. Steeneken, and W. J. Venstra, "Visualizing the motion of graphene nanodrums," *Nano letters*, vol. 16, no. 4, pp. 2768–2773, 2016.

[19] A. Keşkekler, O. Shoshani, M. Lee, H. S. van der Zant, P. G. Steeneken, and F. Alijani, "Tuning nonlinear damping in graphene nanoresonators by parametric–direct internal resonance," *Nature communications*, vol. 12, no. 1, p. 1099, 2021.

[20] R. J. Dolleman, S. Houri, A. Chandrashekar, F. Alijani, H. S. Van Der Zant, and P. G. Steeneken, "Opto-thermally excited multimode parametric resonance in graphene membranes," *Scientific Reports*, vol. 8, no. 1, p. 9366, 2018.

[21] M. Lee, *Applied and fundamental studies of vibrating 2D membranes.* Delft-Leiden: Casimir PhD Series, 2021.

[22] R. Frisenda, E. Navarro-Moratalla, P. Gant, D. P. De Lara, P. Jarillo-Herrero, R. V. Gorbachev, and A. Castellanos-Gomez, "Recent progress in the assembly of nanodevices and van der waals heterostructures by deterministic placement of 2D materials," *Chemical Society Reviews*, vol. 47, no. 1, pp. 53–68, 2018.

2

2

HIGH-FREQUENCY GAS EFFUSION THROUGH NANOPORES IN SUSPENDED GRAPHENE

Hope is the only thing stronger than fear.
A little hope is effective.
A lot of hope is dangerous.

Suzanne Collins

Porous, atomically thin graphene membranes have interesting properties for filtration and sieving applications. Here, graphene membranes are used to pump gases through nanopores using optothermal forces, enabling the study of gas flow through nanopores at frequencies above 100 kHz. At these frequencies, the motion of graphene is closely linked to the dynamic gas flow through the nanopore and can thus be used to study gas permeation at the nanoscale. By monitoring the time delay between the actuation force and the membrane mechanical motion, the permeation time-constants of various gases through pores with diameters from 10-400 nm are shown to be significantly different. Thus, a method is presented for differentiating gases based on their molecular mass and for studying gas flow mechanisms. The presented microscopic effusion-based gas sensing methodology provides a nanomechanical alternative for large-scale mass-spectrometry and optical spectrometry based gas characterisation methods.

This chapter has been published in the journal Nature Communications **11**, 6025 (2020)
The published article is adapted to fit into the context of this thesis.

ALTHOUGH graphene in its pristine form is impermeable, its atomic thickness causes it to be very permeable when perforated [1–3]. This is an advantageous property that has recently been exploited for filtration and separation purposes [4–13]. For sub-nm pore sizes, it has been shown to result in molecular sieving [14–16] and osmotic pressure [17] across graphene membranes. Besides filtration and separation, selective permeability might also provide a route toward sensing applications. In contrast to chemical [18] and work-function based [19] gas sensing principles, the advantage of permeation based sensing is that it does not rely on chemical or adhesive bonds of the gas molecules, which can be irreversible or require thermal or optical methods to activate the desorption of the bound gas molecules [20].

Here, we demonstrate that graphene membranes can be used to pump gases through nanopores at high frequencies, and that the motion of the graphene can be used as a probe of the gas dynamics. When gas molecules flow through pores that are smaller than the gas mean free path length, but larger than their kinetic diameter, their permeation is in the effusive regime. According to Graham's law [21], the effusion time constant τ_{eff} of gas escaping from a cavity of volume V is proportional to the square root of the gas molecular mass M and can be written in terms of the total effusive area A, the temperature T and the universal gas constant R:

$$\tau_{\text{eff}} = \frac{V}{A}\left(\frac{2\pi M}{RT}\right)^{1/2}. \tag{2.1}$$

By using graphene membranes to pump gases [22] through focused ion beam (FIB) milled nanopores [23], we realize an attoliter effusive flow through an orifice. The permeation rate is determined from the frequency (ω) dependent response function z_ω / F_ω which is used to determine the gas-specific time-delay τ_{gas} between the optothermal actuation force F_ω and the membrane displacement z_ω. We show that the permeation time-constants can be engineered by altering the number of pores, their cumulative area and by adding a flow resistance in the form of a gas channel in series with the pore.

Figure 2.1a and 2.1b show a scanning electron microscope (SEM) top-view of a graphene microdrum with a nanopore. Dumbbell-shaped cavities are etched in a silicon substrate with a 285 nm SiO_2 layer using reactive ion etching and covered by a two layer stack of graphene, creating drums with a diameter of 5 μm that are connected by a channel of 0.6 μm wide and 5 μm long. The bilayer graphene layer covers the full area of the dumbbell shaped cavity and gas that is trapped in the volume underneath the graphene can escape through the milled perforations. The frequency response curves of the membranes are measured using a laser interferometry setup (see Figure 2.1c and Methods).

2.1. OPERATION PRINCIPLE

We now discuss how the frequency dependent mechanical response of the graphene drum to the modulated laser actuation can be used to characterize the gas permeation rate through the porous membranes. In vacuum, the graphene membrane is solely actuated by thermal expansion, as a consequence of the temperature variations induced by the modulated blue laser. This effect has been extensively studied by Dolleman *et al.* [24] to characterize the heat transport from membrane to substrate. The temperature at

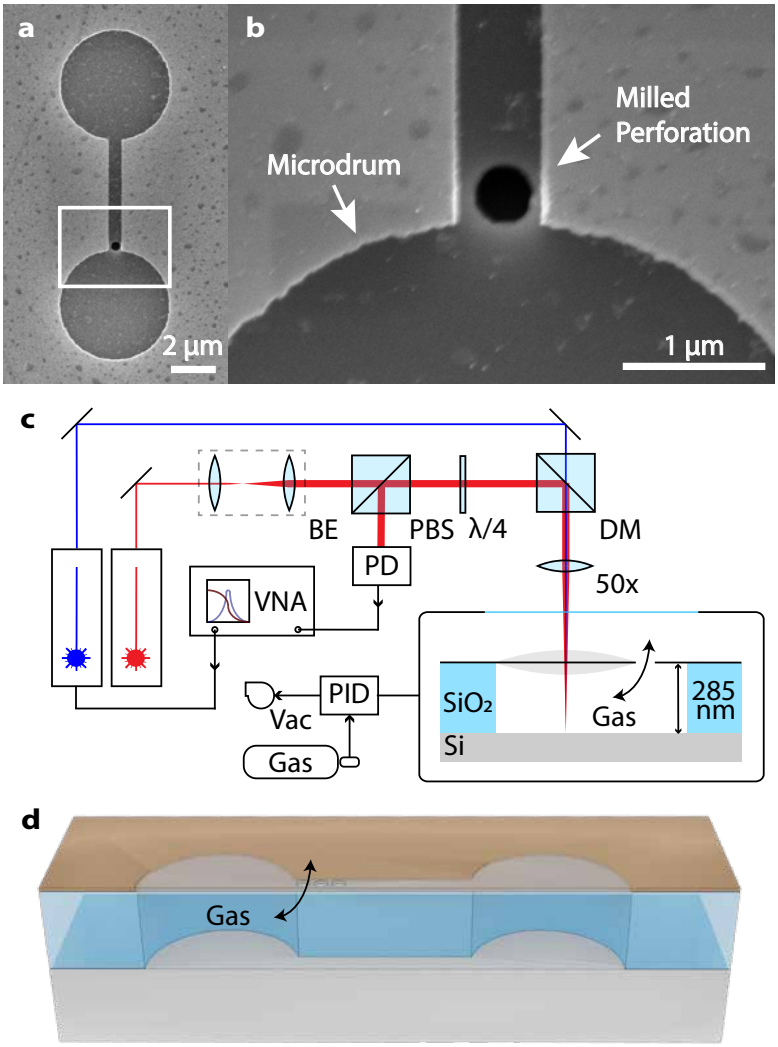

Figure 2.1: *Suspended graphene device and measurement setup.*
a) Electron microscope image of a dumbbell shaped cavity covered by bilayer graphene. b) A nanopore with a diameter of 400 nm is milled in the graphene by an ion beam in the channel that connects the two micro drums. c) Interferometry setup used to actuate and detect the motion of the graphene micro drums. The red laser passes subsequently through the beam expander (BE), the polarized beam splitter (PBS) and the quarter-wave plate ($\lambda/4$), after which it is combined with the blue laser using a dichroic mirror (DM) and focused on a micro drum using a 50x objective. The readout is performed by a high-frequency photodiode (PD) that is connected to the Vector Network Analyser (VNA). The VNA modulates the power of the blue laser that actuates the membrane. Gas pressure inside the vacuum chamber is controlled by a PID controller. d) Schematic of the device geometry and gas effusion path.

the centre of the membrane $T(t) = T_{ext} + \Delta T$, where T_{ext} is the ambient temperature, can be approximately described by a first order heat equation, where the optothermal laser power $\mathscr{P}_{AC} e^{i\omega t}$ is absorbed by the graphene membrane and thermal transport towards the substrate is approximated by a single thermal time constant $\tau_{th} = R_{th} C_{th}$ corresponding to the product of the membrane's thermal resistance and thermal capacitance:

$$\frac{d\Delta T}{dt} = -\frac{\Delta T}{\tau_{th}} + \frac{\mathscr{P}_{AC}}{C_{th}} e^{i\omega t}. \tag{2.2}$$

In the presence of gas, the pressure difference across the orifice $\Delta P = P - P_{ext}$ between the cavity pressure P and the ambient pressure P_{ext} can also be described by a differential equation. There are three contributions to the time derivative of the pressure $d\Delta P/dt$: gas permeation, motion of the membrane and laser heating of the gas in the cavity:

$$\frac{d\Delta P}{dt} = -\frac{\Delta P}{\tau_{gas}} + \gamma \frac{dz}{dt} + \frac{\mathscr{P}_{AC}}{C_{gas}} e^{i\omega t}. \tag{2.3}$$

Gas permeation out of the membrane with a time constant τ_{gas} gives a contribution $-\Delta P/\tau_{gas}$. Compression of the gas by the downward deflection z of the membrane results in a term $\gamma dz/dt$, where γ is a constant of proportionality. Heating of the gas due to power absorption of the modulated laser can be described by a term $\frac{\mathscr{P}_{AC}}{C_{gas}} e^{i\omega t}$, where C_{gas} is a constant relating thermal power to gas expansion.

A third differential equation is used to describe the mechanics of the membrane, which at low amplitudes experiences a force contribution proportional [24, 25] to the pressure difference $F_P = \beta \Delta P$ and an effective thermal expansion force $F_T = \alpha \Delta T$:

$$m_{eff} \frac{d^2 z}{dt^2} + c \frac{dz}{dt} + kz = \alpha \Delta T + \beta \Delta P. \tag{2.4}$$

Here, we describe the fundamental mode of motion at the centre of the membrane by a single degree of freedom forced harmonic oscillator with effective mass m_{eff}. The resulting system of three differential equations (2.2-2.4) is solved analytically for frequencies significantly below the resonance frequency $\omega_{res} = \sqrt{k/m_{eff}}$, where terms proportional to d^2z/dt^2 and dz/dt can be neglected, to obtain the complex frequency response $z_\omega/\mathscr{P}_{AC}$ of the membrane. A full derivation, solution and numerical simulation of the three differential equations can be found in the Annex. The real and imaginary parts of the solution relate to the components of the displacement z_ω that are in-phase and out-of-phase with respect to the laser power modulation. The imaginary part of this expression is:

$$Im(z_\omega) = a \frac{\omega \tau_{th}}{1 + \omega^2 \tau_{th}^2} + b \frac{\omega \tau_{gas}}{1 + \omega^2 \tau_{gas}^2}. \tag{2.5}$$

This equation is used to fit to the experimental data with a, b, τ_{th} and τ_{gas} as fit parameters. At frequencies close to the reciprocal permeation time $\omega_{gas} = 1/\tau_{gas}$ the imaginary part of the displacement displays a minimum, similar to the effect observed near $\omega_{th} = 1/\tau_{th}$ for the thermal actuation [24]. In the following, these extrema in the imaginary part of the frequency response will be used for characterizing permeation and thermal time-constants.

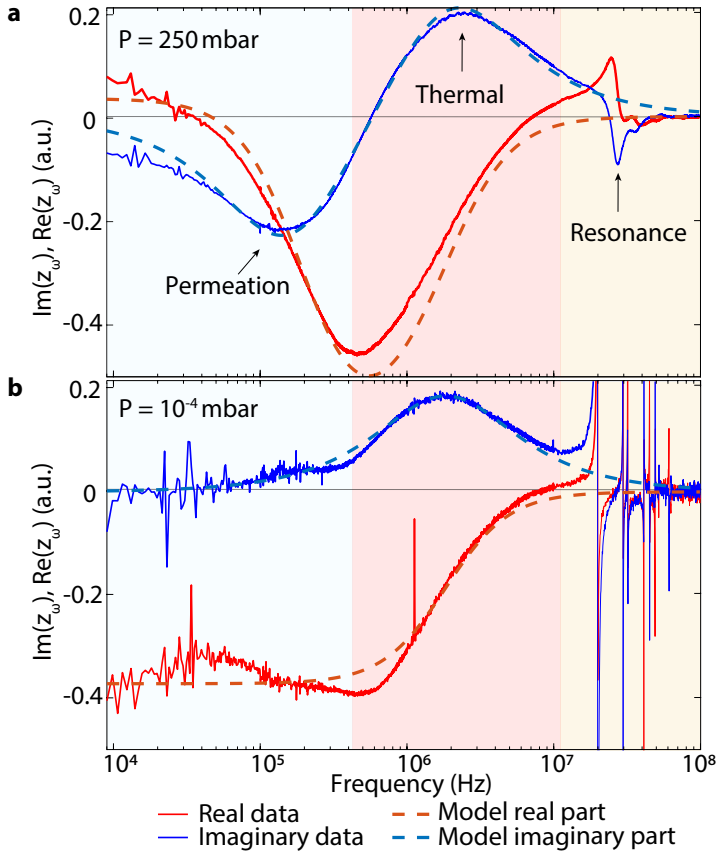

Figure 2.2: *Graphene membrane motion z_ω (phasor) in gas and vacuum.*
a) Frequency response of the micro drum shown in Figure 2.1 in nitrogen gas at $P = 250$ mbar showing the real (in phase, red curve) and imaginary (90 degree phase shift, blue curve) parts of the signal, $\mathrm{Im}(z_\omega)$, $\mathrm{Re}(z_\omega)$. Dashed curves indicate the fitted model response. b) Measurement on the same micro drum at $P < 10^{-4}$ mbar shows that the permeation peak diminishes in vacuum and the maximum of the thermal peak shifts by 10% from 2 MHz to 1.8 MHz.

2.2. RESPONSE IN GAS

A typical frequency response curve z_ω of a micro drum at a pressure $P = 250$ mbar in nitrogen gas is shown in Figure 2.2a. The mechanical resonance occurs in the MHz domain, here at $f = 25.9$ MHz with $Q = 4.2$. Below the mechanical resonance, the imaginary response $\mathrm{Im}(z_\omega)$ shows a characteristic dip-peak shaped curve for which the extrema are at 160 kHz and 2 MHz. These are assigned to the extrema of equation (2.5) corresponding to fit parameters $\tau_{\mathrm{th}} = 1/(2\pi \cdot 2\,\mathrm{MHz}) = 81$ ns and $\tau_{\mathrm{gas}} = 1/(2\pi \cdot 160\,\mathrm{kHz}) = 991$ ns.

To prove that one of the extrema is related to gas permeation, we study the dependence of the extrema on pressure. The measurements in high vacuum show only one extremum in the imaginary response, corresponding to a thermal time $\tau_{\mathrm{th}} = 87$ ns, as shown in Figure 2.2b. The disappearance of the dip at vacuum is a clear indicator that the dip is a result of gas interaction with the motion of the drum. Without a nanopore, the dip does not appear in any of the tested gases at any pressure (see Figure 2.11). This is evidence that the dip is actually a result of permeation through the nanopore. A small extremum is observed at $2 \cdot 10^5$ Hz in high vacuum such as in Figure 2.2b, which is attributed to electrical cross-talk as discussed in [26]. This feature cannot be distinguished in Figure 2.2a and is neglected in further analysis. The reference samples without perforations show only one thermal extremum with a similar time-constant τ_{th} to the perforated membranes. The second extremum, a dip in $\mathrm{Im}(z_\omega)$, only appears for perforated membranes, and does not appear in high vacuum. Therefore, it is concluded that the dip in $\mathrm{Im}(z_\omega)$ at 160 kHz in Figure 2.2a is due to gas permeation with permeation time $\tau_{\mathrm{gas}} = 1/(2\pi \cdot 160\,\mathrm{kHz}) = 991$ ns.

The permeation time constants τ_{gas} are extracted for a range of gases varying in molecular mass M from 4 u (He) to 130 u (SF_6) in Figure 2.3a. Figure 2.3b shows that the permeation time constant closely follows Graham's effusion law with $\tau_{\mathrm{gas}} \propto \sqrt{M}$, as expected for gas transport through the nano pores. The slope of the linear effusion model is fitted to the data, and the grey area shows the 95% confidence interval of the fitted slope. This agreement demonstrates that the porous graphene membranes can be used to distinguish gases based on their molecular mass. A significant deviation between measurement and theory is only observed for He, which could be due to fitting inaccuracies related to the proximity of the thermal time-constant and mechanical resonance frequency peaks to the gas permeation related peak.

Tuning of permeability The gas permeation time τ_{gas} can be tuned by varying the cumulative pore area, either by changing the number of pores or their size. This tuning can be useful, since too short time constants may lead to overlap between the τ_{gas} and τ_{th} peaks or even with the resonance peaks, whereas long permeation rates could be problematic in view of acquisition times.

Figure 2.4a demonstrates τ_{gas} tuning in drums with increasing number n of 200 nm pores. The permeation time τ_{gas} is inversely proportional to the cumulative pore area A. The average reduction of τ_{gas} by a factor 2.26 ± 0.5 when doubling the number of pores from 1 to 2 is additional evidence that this time-constant is related to the permeation rate. The change in the permeation time by a factor higher than two when doubling the number of pores might be caused by the fact that the two pores are located closer

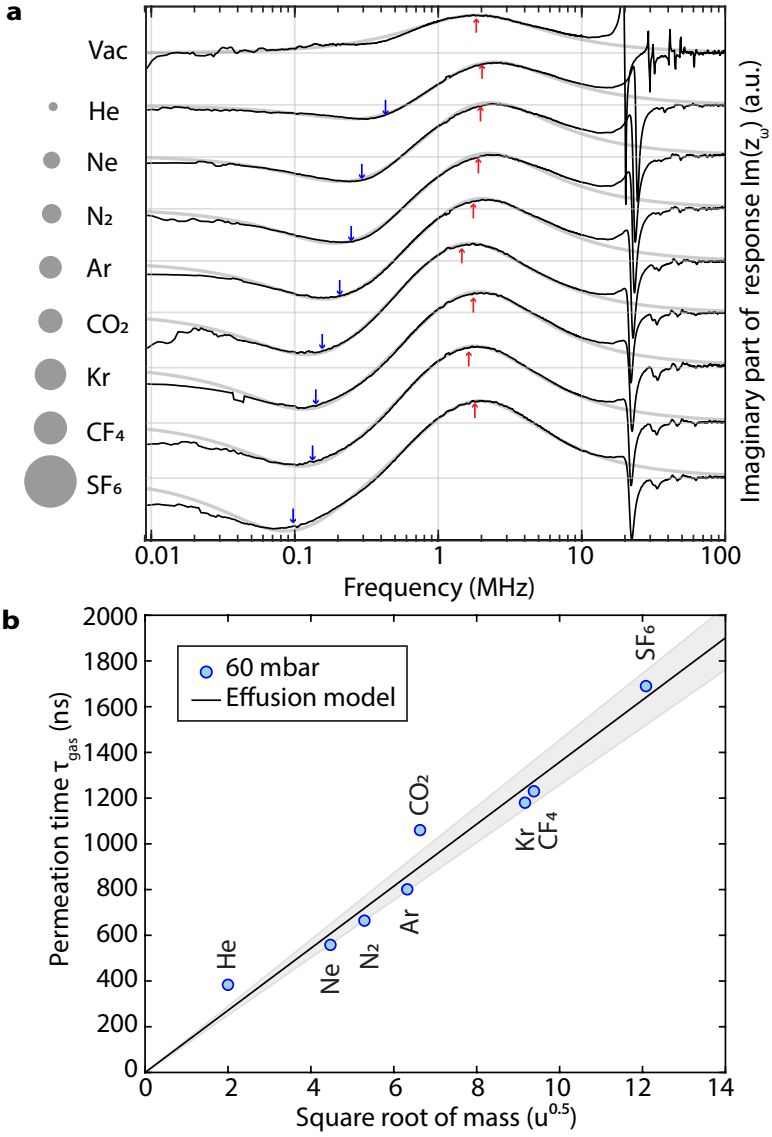

Figure 2.3: *Dependence of τ_{gas} on gas molar mass.*
a) Measurements performed in high vacuum and in various gases at $P = 60$ mbar on a micro drum with a 400 nm pore. Equation (2.5) (grey line) is fitted to the imaginary part of the measurement data (black line) and the red and blue arrows indicate the values obtained for τ_{th} and τ_{gas}, respectively. The areas of the circles represent the relative mass of the gas particles. b) The permeation time τ_{gas} increases linearly with the square root of the particle mass as predicted by Graham's law. The black line shows a fit of the measured values of τ_{gas} to equation 2.1 with $V/A = 2.71 \cdot 10^{-6} \pm 1.7 \cdot 10^{-7}$ m. The 95% confidence interval is shaded grey.

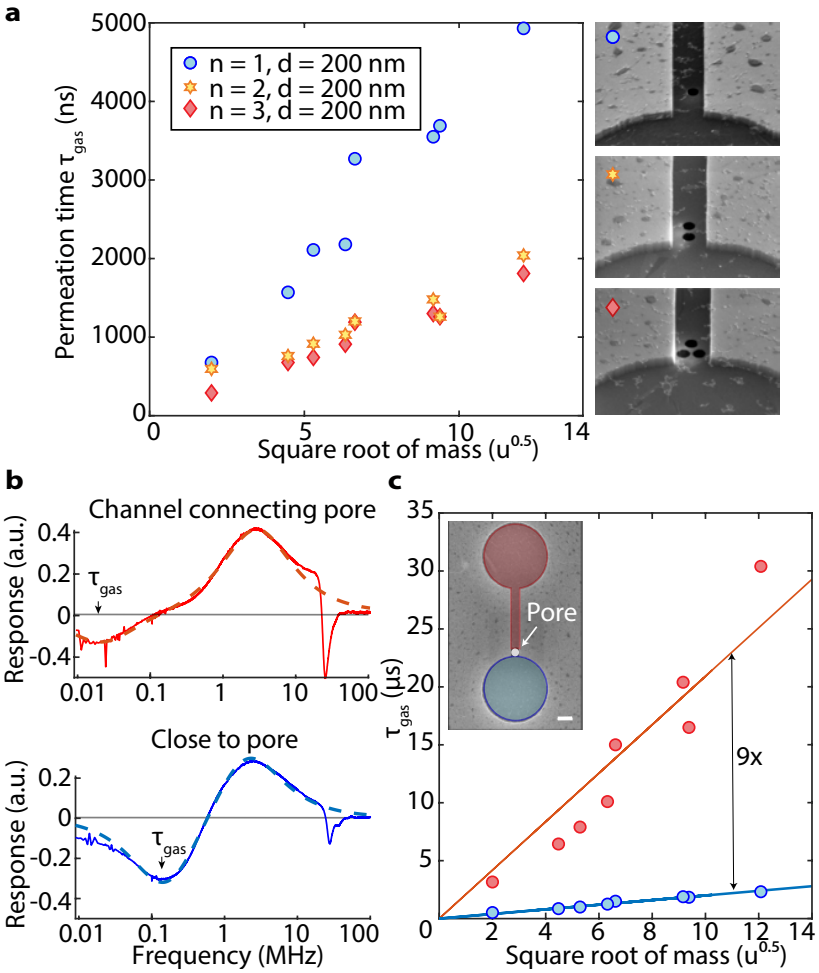

Figure 2.4: *Tuning of the gas permeation time.*
a) Comparison of measurements between three different drums with increasing number of 200 nm pores. The permeation time τ_{gas} reduces with the cumulative pore area A, but saturates at 3 pores. b) Measurements of $\text{Im}(z_\omega)$ with the laser aimed at the drum next to the pore and at the drum connected by a channel to the pore, respectively the blue and the red drum in the SEM inset in c, showing a large tuning of τ_{gas}. c) The gas permeation time of the drum close to the perforation is 9 times shorter than of the drum far away from the perforation. Inset: SEM image (false colour) of the two graphene drums connected by a channel with a 400 nm circular pore, scalebar = 1 μm. All measurements in this figure are performed at $P = 60$ mbar.

to the drum than the single pore, leading to a higher permeation rate. When increasing the number of pores to 3, the time-constant does not drop accordingly but by a factor 2.63 ± 0.2, indicating that other effects than pore effusion limit the permeation rate. The permeation area of 3 holes ($A = 9.4 \cdot 10^4$ nm^2) is 55% of the cross-section of the channel between the drums ($A = 17 \cdot 10^4$ nm^2). Therefore, the channel entrance acts as a significant additional obstacle for gas permeating through the pore, an effect that is further explored in the next paragraph. The pore placement in the channel and mechanical device-to-device variations could also be factors affecting the permeation time.

Gas kinetics in a channel. We investigate the gas kinetics further by placing the holes further away from the graphene drum, at the other end of the channel that connects both drums. The SEM inset of Figure 2.4c shows a pore inside the channel, that is close to the blue drum, but far from the red drum. The rectangular, graphene-covered channel, with dimensions of $5 \times 0.6 \times 0.285$ μm^3, is in series with the pore for the red drum. It is found from Figure 2.4c that the permeation time is 9 times longer for the red drum that is in series with the channel. The difference in permeation time is a measure of the transmission probability ψ_r for gas atoms to pass through the rectangular channel. In the ballistic regime, the conductance and time-constant are given as the product of the time-constant of the aperture (the pore) and the transmission probability of the channel ψ_r so that $\tau_{\text{gas,close}} = \psi_r \times \tau_{\text{gas,far}}$. The transmission probability through a rectangular channel can be calculated using the Smoluchowski formula [27] for which an useful approximation [28, 29] is given by:

$$\psi_r = \frac{16}{3\pi^{3/2}} \frac{a}{l} \ln\left(4\frac{b}{a} + \frac{3}{4}\frac{a}{b}\right), \tag{2.6}$$

where $a = 285$ nm and $b = 600$ nm are the cross-sectional dimensions and $l = 5\,\mu$m is the length in the direction of gas flow. This formula predicts a 12% transmission probability for our geometry, in close agreement with the experimental value of 11% that is found from the ratio between the slopes of the blue and red solid lines in Figure 2.3. We can conclude that ballistic transport is taking place in this nano channel.

Flow regimes. The size of individual pores determines whether viscous Sampson or molecular Knudsen flow is taking place [30]. Figure 2.5 compares time-constants τ_{gas} in devices with equal cumulative area $A = 4\pi \cdot 10^4$ nm^2 and different pore diameters. At $P = 125$ mbar all devices show a linear relation between the square root of mass and the permeation time according to Graham's law. In contrast, at higher pressures where the mean free path length λ becomes smaller than the pore diameter d (Kn = $\lambda/d < 1$), in particular for the larger molecular masses and large pore sizes, the linear dependence disappears. In the transitional region between Knudsen and Sampson flow, classical effusion no longer correctly describes the flow and viscosity effects lead to larger values of τ_{gas} than predicted by Graham's law. This increase is in line with studies on pipe and channel flows, [31] which show a maximum in the permeation time near Kn=1 where the transition from Knudsen to Sampson flow occurs.

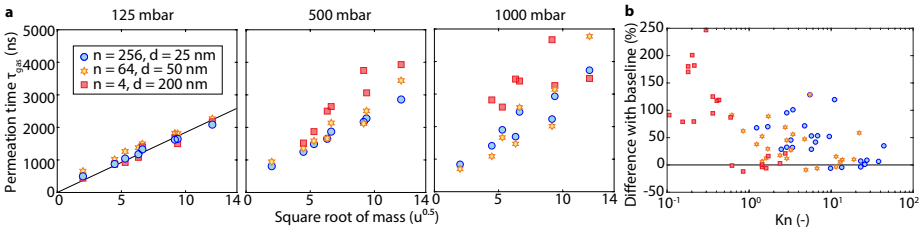

Figure 2.5: *Transition from Knudsen to Sampson flow.*
To compare different Knudsen numbers, the pore diameter d and number of pores n are varied, maintaining constant total pore area. Permeation times are shown in the transitional region between Knudsen and Sampson flow at a Kn range of 0.1-100. a) At P = 125 mbar all devices follow Graham's law, as indicated by a fit to a straight line through the origin. At higher pressures, the measurements deviate from a straight line. b) The difference with respect to the black baseline in a) is calculated for all measurements shown in a). As Kn drops below 1, the permeation time increases and Graham's law does no longer describe the values of τ_{gas} correctly.

Thermal transport. Besides permeation, thermodynamic sensing can be achieved by observing changes in the thermal time constant in a fashion similar to Pirani gas sensors. In general the gas conducts heat better at higher pressures, and it does so also for molecules with a smaller molecular mass and higher molecular velocity. However, by analysing the values of τ_{th} that are determined from measurements like in figure 2.3a, it appears that the thermal conductivity of the gases is a less precise route toward gas sensing than the permeation based method shown in Figure 2.3b. Further experimental results for the thermal time constant can be found in the Annex.

2.3. DISCUSSION

We have studied the effect of nanopores on the dynamics of graphene membranes. When gas is admitted to the nanodrums, it is found that a time delay appears between the membrane position and force (Fig. 2.2a), and that it does not only depend on the size and number of pores (Fig 2.4a), but also on the type of gas (Fig. 2.3). This time delay is not observed in drums without nanopores (Fig. 2.11). It is therefore attributed to permeation of gas through the nanopores and thus provides a method for studying nanoscale gas kinetics based on measuring the permeation time-constant τ_{gas} of gases through pores in bilayer graphene membranes. The method is based on high-frequency pumping of gases through nanopores. Due to the nanometer pore sizes, permeation is governed by effusion, such that permeation rates are inversely proportional to the square root of the molecular mass of the gas. By optothermal driving, the gas in the cavity below the graphene membrane is pressurized and pumped through the porous membrane. At angular driving frequencies close to the inverse of the permeation time constant ($\omega = 1/\tau_{gas}$), a dip in the imaginary part of the frequency response appears which is used to characterize the gas species based on their effusion speed. By changing the number of pores and pore diameter using FIB, the time constants can be adjusted to a desired range. The presented measurement method is used to study gas flow through a microchannel at the transition from Knudsen to Sampson flow, where we observe an increase in the permeation time. This work shows that the extreme flexibility and per-

meability of suspended porous membranes of 2D materials can be used as an interesting platform for studying kinetics of gases at the nanoscale.

2.4. METHODS

Sample fabrication. Dumbbell-shaped cavities are etched in a silicon substrate with a 285 nm SiO_2 layer using reactive ion etching, creating cavities with a diameter of 5 μm that are connected by a channel of 0.6 μm wide and 5 μm long. A stack of two chemical vapour deposited (CVD) monolayers of graphene is transferred over the cavity with a dry transfer method by Applied Nanolayers B.V. and subsequently annealed in an argon furnace. Nanoscale circular pores with diameters varying from 10 nm to 400 nm are milled through the suspended CVD graphene using a focused gallium beam FEI Helios G4 CX [10]. Pores are created in the channel instead of the drum, as directly milling on the drum reduced signal quality. In the annex, experiments on a circular single-layer graphene drum with perforations created directly on the drum and the mechanical deformations introduced by milling of nanopores are discussed.

Laser interferometry. Two lasers are focused with a 1.5 μm spot size on the sample in a PID controlled pressure chamber. A red laser (λ_{red} = 632.8 nm) is used for detection of the amplitude and phase of the mechanical motion, where the position-dependent optical absorption of the graphene results in an intensity modulation of the reflected red laser light, that is detected by a photodiode [32]. A power-modulated blue laser (λ_{blue} = 405 nm), which is driven by a vector network analyser (VNA) at frequencies from 9 kHz to 100 MHz, optothermally actuates the membrane motion [33]. The incident red and blue laser powers are 2 mW and 0.3 mW, respectively. A calibration measurement, in which the blue laser is directly illuminating the photodiode, is used to eliminate systematic parasitic delays in the system [24].

2.5. ANNEX

MODEL DERIVATION

In this section we derive the model for the complex amplitude of the membrane. The temperature at the center of the membrane $T(t)$ can be approximately described by a first order heat equation:

$$\frac{\mathrm{d}\Delta T}{\mathrm{d}t} = -\frac{\Delta T}{\tau_{\text{th}}} + \frac{\mathscr{P}_{\text{AC}}}{C_{\text{th}}} e^{i\omega t}, \tag{2.7}$$

where the optothermal laser power $\mathscr{P}_{\text{AC}} e^{i\omega t}$ is absorbed by the graphene membrane and thermal transport towards the substrate is determined by a single thermal time constant $\tau_{\text{th}} = R_{\text{th}} C_{\text{th}}$ corresponding to the product of the membrane's thermal resistance and thermal capacitance.

In the presence of gas, the pressure difference $\Delta P = P - P_{\text{ext}}$ between the cavity pressure P and the ambient pressure P_{ext} can also be described by a differential equation.

There are three contributions to the time derivative of the pressure $\mathrm{d}\Delta P/\mathrm{d}t$: gas permeation, motion of the membrane and laser heating of the gas in the cavity.

$$\frac{\mathrm{d}\Delta P}{\mathrm{d}t} = -\frac{\Delta P}{\tau_{\mathrm{gas}}} + \gamma\frac{\mathrm{d}z}{\mathrm{d}t} + \frac{\mathscr{P}_{\mathrm{AC}}}{C_{\mathrm{gas}}}e^{i\omega t} \tag{2.8}$$

Gas permeation out of the membrane with a time constant τ_{gas} gives a contribution $-\Delta P/\tau_{\mathrm{gas}}$. Compression of the gas by the downward deflection z of the membrane results in a term $\gamma \mathrm{d}z/\mathrm{d}t$, where for small z and cavity depth g, it can be shown from Boyle's law that $\gamma = \eta P_{ext}/g$, where η is a factor that depends on the deformed shape of the membrane ($\eta = 1$ for a piston like membrane motion). Heating of the gas due to power absorption of the modulated laser can be described by a term $\frac{\mathscr{P}_{\mathrm{AC}}}{C_{\mathrm{gas}}}e^{i\omega t}$, where $1/C_{\mathrm{gas}} = \mathrm{d}P/\mathrm{d}U$ is the pressure increase per absorbed laser heat energy U. For a gas at constant volume V, the temperature induced pressure change is given by the ideal gas law as $\mathrm{d}T/\mathrm{d}P = \frac{V}{Nk_B}$, where N is the number of gas molecules and k_B is Boltzmann's constant. The temperature change for a certain absorbed amount of heat is given by $\mathrm{d}U/\mathrm{d}T = c_v m$, where c_v is the specific heat and m the mass of the gas molecules. Thus it is found that the power induced gas pressure increase is characterized by the constant $C_{\mathrm{gas}} = \mathrm{d}U/\mathrm{d}T \times \mathrm{d}T/\mathrm{d}P = VmC_v/NK_B$.

A third differential equation is used to describe the mechanics of the membrane, which at low amplitudes experiences a force contribution proportional [25] to the pressure difference $F_P = \beta\Delta P$ and an effective thermal expansion force $\alpha\Delta T$. We approximate the fundamental mode of motion of the center of the membrane by a forced harmonic oscillator with effective mass m_{eff} to obtain:

$$m_{eff}\frac{\mathrm{d}^2 z}{\mathrm{d}t^2} + c\frac{\mathrm{d}z}{\mathrm{d}t} + kz = \alpha\Delta T + \beta\Delta P. \tag{2.9}$$

The resulting system of 3 differential equations (2.7-2.9) is solved analytically for frequencies below the resonance frequency, where terms proportional to $\mathrm{d}^2z/\mathrm{d}t^2$ and $\mathrm{d}z/\mathrm{d}t$ can be neglected, to obtain the complex frequency response of the membrane. For frequencies well below the resonance frequency the induced amplitude can be approximated by:

$$z_\omega \approx \alpha\Delta T_\omega + \beta\Delta P_\omega. \tag{2.10}$$

This can be substituted into equation 2.8 to arrive at:

$$\frac{d\Delta P}{dt} + \frac{\Delta P}{(1-\beta\gamma)\tau_{\mathrm{gas}}} = \frac{\gamma\alpha}{(1-\beta\gamma)}\frac{d\Delta T}{dt} + \frac{\mathscr{P}_{\mathrm{AC}}}{(1-\beta\gamma)C_P}e^{i\omega t}. \tag{2.11}$$

This expression still depends on the temperature ΔT of the membrane. A solution to the temperature ΔT of the membrane following equation 2 in the main text, as found by Dolleman *et al.*, is given by:

$$\Delta T_\omega = \frac{R_{th}\mathscr{P}_{AC}}{i\omega\tau_{th}+1}e^{i\omega t}. \tag{2.12}$$

This solution is used to arrive at:

$$\frac{d\Delta P}{dt} + \frac{\Delta P}{(1-\beta\gamma)\tau_{\mathrm{gas}}} = \frac{\gamma\alpha R_{\mathrm{th}}\mathscr{P}_{\mathrm{AC}}}{(1-\beta\gamma)}\frac{i\omega e^{i\omega t}}{i\omega\tau_{\mathrm{th}}+1} + \frac{\mathscr{P}_{\mathrm{AC}}}{(1-\beta\gamma)C_P}e^{i\omega t}. \tag{2.13}$$

Next, we assume $\gamma = 0$, which holds true for small membrane deflections. We now arrive at:

$$\frac{d\Delta P}{dt} + \frac{\Delta P}{\tau_{\text{gas}}} = \frac{\mathscr{P}_{\text{AC}}}{C_P} e^{i\omega t}. \tag{2.14}$$

By solving this differential equation a solution for ΔP is found:

$$\Delta P_\omega = \frac{\tau_{\text{gas}}}{C_P} \frac{\mathscr{P}_{AC}}{i\omega\tau_{gas} + 1} e^{i\omega t}. \tag{2.15}$$

By inserting expressions 2.12 and 2.15 into formula 2.10, the complex amplitude z_ω can be obtained:

$$z_\omega e^{i\omega t} = \frac{\alpha R_{\text{th}} \mathscr{P}_{\text{AC}}}{i\omega\tau_{\text{th}} + 1} e^{i\omega t} + \frac{\tau_{\text{gas}}}{C_P} \frac{\beta \mathscr{P}_{\text{AC}}}{i\omega\tau_{\text{gas}} + 1} e^{i\omega t}. \tag{2.16}$$

The imaginary part of the complex amplitude is calculated:

$$\text{Im}(z_\omega) = \frac{\alpha\tau_{\text{th}} R_{\text{th}} \mathscr{P}_{\text{AC}}}{1 + \omega^2\tau_{\text{th}}^2} + \frac{\tau_{\text{gas}}}{C_P} \frac{\beta\tau_{\text{gas}} \mathscr{P}_{\text{AC}}}{1 + \omega^2\tau_{\text{gas}}^2}. \tag{2.17}$$

This is the same as equation 2.5 in the main text that is used for fitting, where $a = \alpha R_{\text{th}} \mathscr{P}_{\text{AC}}$ and $b = \frac{\beta\tau_{\text{gas}} \mathscr{P}_{\text{AC}}}{C_P}$.

NUMERICAL SIMULATION

The system of 3 differential equations (2.7-2.9) is numerically simulated using an analogy to the currents running in an electric circuit. The circuit consists of a thermal, a mechanical and a pneumatic domain, as shown in Figure 2.6. The domains are discussed one by one. Simulations have been performed using Simulink.

Mechanical The mechanical motion of the membrane is represented by a driven damped harmonic oscillator. The equation of motion for the membrane is represented by an RLC circuit in Figure 2.6 with a resistor $R_m = c$, an inductor $L_m = m$ and a capacitor $C_m = 1/k$, driven by two voltage controlled voltage sources, $V_{th} = \alpha\Delta T$ and $V_{gas} = \beta\Delta P$. The equation of motion is written next to the expression for the electric potential in this circuit:

$$m\frac{d^2z}{dt^2} + c\frac{dz}{dt} + kz = \alpha\Delta T + \beta\Delta P,$$
$$L_m\frac{d^2q}{dt^2} + R_m\frac{dq}{dt} + \frac{q}{C_m} = V_{\text{th}} + V_{\text{gas}}.$$

Comparison shows that the charge q on the capacitor in this circuit can represent the deflection z of the membrane. In the schematic the voltage over the capacitor, $V_C = \frac{q}{C_m}$, is taken as an output for readout.

Thermal The optothermal drive actuating the membrane is represented by an AC voltage source. It controls the voltage controlled current source driving a parallel RC circuit,

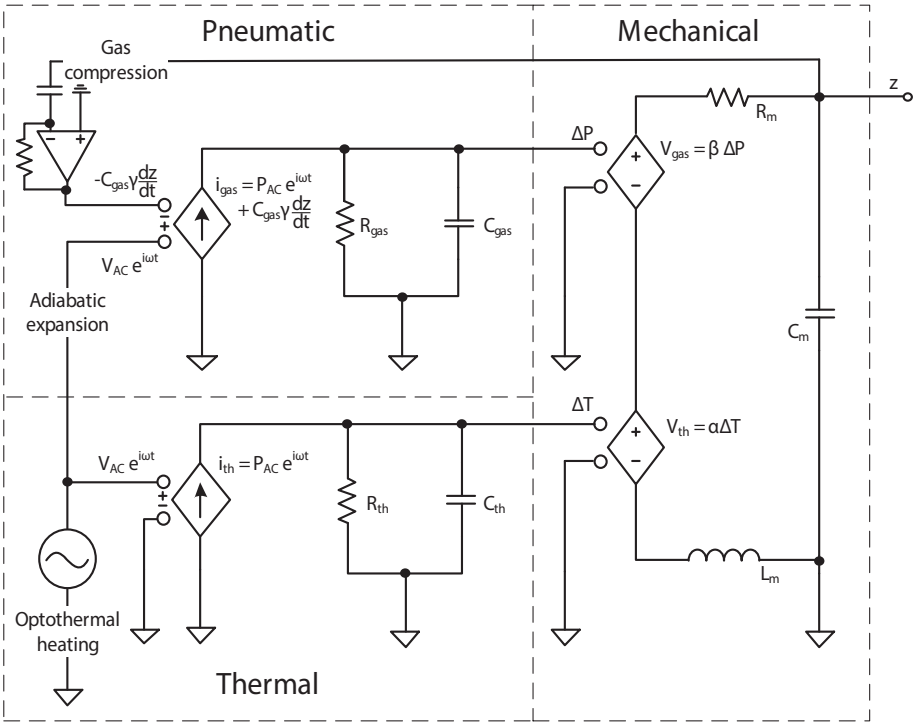

Figure 2.6: Equivalent electric model for the porous membrane.

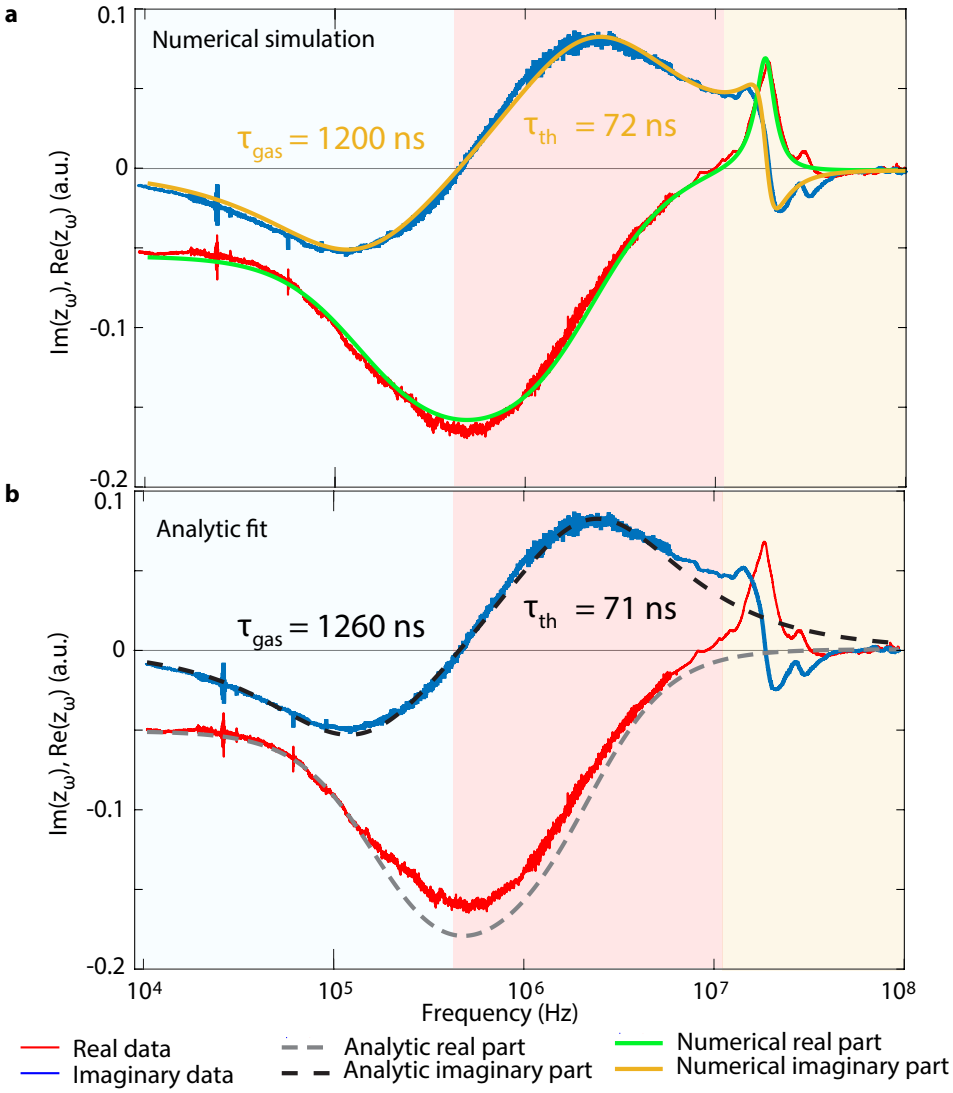

Figure 2.7: Comparison of the numerical simulation to the analytic formula. a) The governing differential equations (2.7 - 2.9) are solved numerically using Simulink (green and yellow), yielding a nearly perfect fit to the measured frequency response curves (blue and red) of the porous membrane including the first resonance peak. b) A fit using the analytic formula (dashed lines), yielding nearly the same fitting parameters as with the numerical simulation.

resembling the thermal flux delivered to the graphene with heat capacity C_{th} and thermal boundary resistance R_{th}. The equation for the membrane temperature is written next to the equation for the currents running through this circuit:

$$\frac{d\Delta T}{dt} + \frac{\Delta T}{\tau_{\text{th}}} = \frac{\mathscr{P}_{\text{AC}}}{C_{\text{th}}} e^{i\omega t},$$
$$C_{\text{th}} \frac{dV_C}{dt} + \frac{V_C}{R_{\text{th}}} = i_{\text{th}}.$$

Comparison shows that the voltage across the capacitor V_C can represent the temperature of the membrane T. Thermal expansion sets the membrane in motion. Therefore, this voltage controls the source driving the circuit in the mechanical domain.

Pneumatic The optothermal drive causing adiabatic expansion of the gas is represented by an AC voltage source. Moreover, the movement of the membrane compresses the gas. The voltage over the capacitor in the mechanical domain kz controls a voltage controlled voltage source which is connected to a derivator to change the signal into the effective compression $-C_{\text{gas}}\gamma\frac{dz}{dt}$. A voltage controlled current source drives an RC circuit consisting of a capacitor C_{gas} and a resistor R_{gas} in parallel. This circuit resembles the pressure in the cavity with corresponding effective pressure capacity and permeation resistance. The equation for the pressure in the cavity is written next to the equation for the currents running through this circuit:

$$\frac{d\Delta P}{dt} + \frac{\Delta P}{\tau_{\text{gas}}} = \frac{\mathscr{P}_{\text{AC}}}{C_{\text{gas}}} e^{i\omega t} + \gamma\frac{dz}{dt},$$
$$C_{\text{gas}} \frac{dV_C}{dt} + \frac{V_C}{R_{\text{gas}}} = i_{\text{gas}} + \gamma\frac{dV_z}{dt}.$$

Comparison shows that the voltage across the capacitor V_C can represent the pressure inside the cavity P. The force exerted by the gas sets the membrane in motion. Therefore, this voltage controls the source driving the circuit in the mechanical domain.

The frequency response of a device is numerically simulated. Figure 2.7a compares shows data from a device in nitrogen gas with 64 × 50 nm pores with fitting parameters $\tau_{\text{gas}} = 1200$ ns and $\tau_{\text{th}} = 72$ ns. For comparison, a fit of the analytic solution to the same data is shown in 2.7b. The analytic solution yields $\tau_{\text{gas}} = 1260$ ns and $\tau_{\text{th}} = 71$ ns. The difference between numerical simulation and analytic fit is 5%, and the numerical simulation includes the primary resonance peak.

THERMAL TIME CONSTANT

It is interesting to also investigate the thermal time constant for the different gases at varying pressures. The presence of gas in the cavity opens a new thermal conduction pathway for the membrane and the thermal time constant is therefore expected to decrease as compared to the vacuum measurement. In view of the small dimensions of the gap between the membrane and the substrate the Knudsen formula is used to calculate the effective thermal conductivity k_{eff} of the gas:

$$\frac{k_{\text{eff}}}{k_0} = \frac{1}{1+2\beta\text{Kn}}. \tag{2.18}$$

Here, k_0 is the thermal conductivity of the gas and β a constant with a value of about 1.5 that depends on the accommodation coefficient [34, 35]. Both conduction to the substrate and through the gas contribute to the final thermal time-constant:

$$\tau_{\text{th}}^{-1} = \tau_{\text{th,vac}}^{-1} + \frac{\xi k_{\text{eff}}}{\rho c_p h_g d}. \tag{2.19}$$

Here, h_g, ρ and c_p are the radius, height, density and thermal capacity of the graphene membrane, and d is the cavity depth. A measurement in vacuum is performed to find the thermal equilibration time $\tau_{\text{th,vac}} = 87$ ns, which is comparable to values reported in literature for single layer graphene, [24] suggesting that similar boundary effects are limiting thermal conduction. The constant ξ is a transmission coefficient arising from temperature slip on the solid-gas interface [36]. Figure 2.8 shows that the gas indeed provides a new heat conduction pathway, decreasing the thermal time constant as effective thermal conductivity increases. From the data a value of $\xi = 0.17$ is found to fit our experiments.

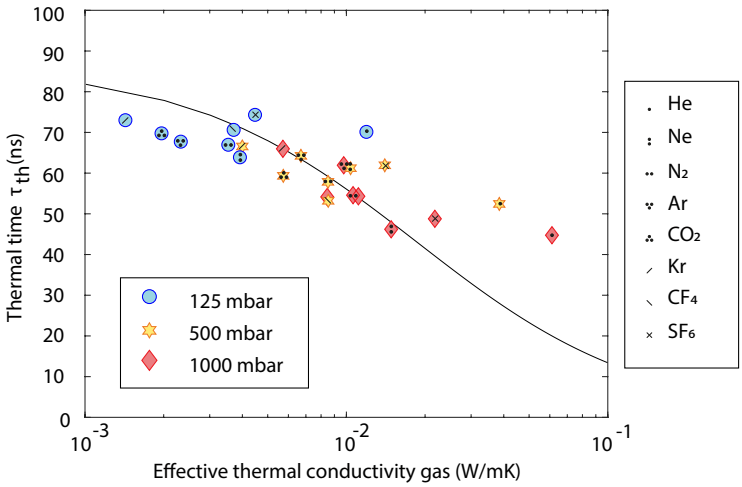

Figure 2.8: The gas offers a new pathway for heat to escape from the membrane, in consequence lowering the thermal time τ_{th} as the effective thermal conductivity of the gas increases. The black line is a fit to equation 2.19 with fit parameter $\xi = 0.17$.

Gas sensing can be achieved by observing changes in the thermal time constant in a fashion similar to Pirani gas sensors. In general the gas conducts heat better at higher pressures, and it does so also for molecules with a smaller molecular mass and higher molecular velocity. However, it appears that thermal conductivity of the gases is a less precise route toward gas sensing than the permeation based method discussed in the main text.

MEASUREMENTS ON SINGLE-LAYER CIRCULAR GRAPHENE MICRO DRUM WITH NANOPERFORATIONS

Smaller perforations with sizes below one nanometer could enable molecular sieving and enhance responsivity of these devices. With this purpose, some single layer graphene drums have been exposed to highly energetic ion bombardment with $129Xe^{23+}$ 0.71 MeV/u, with a flux ranging from $5.09 \cdot 10^7$ to $5.09 \cdot 10^9$ ions per square centimeter at the SME beamline of GANIL (Caen, France). This is similar to the treatment described by Madauß et al.[7] Characterization of the nano indentations on the drum is performed using AFM. The nanopore sizes are distributed normally with mean 14 nm. This experiment is of interest since it shows that our gas sensing principle works using a single layer circular membrane with defects which could potentially lead to applications benefiting from molecular sieving.

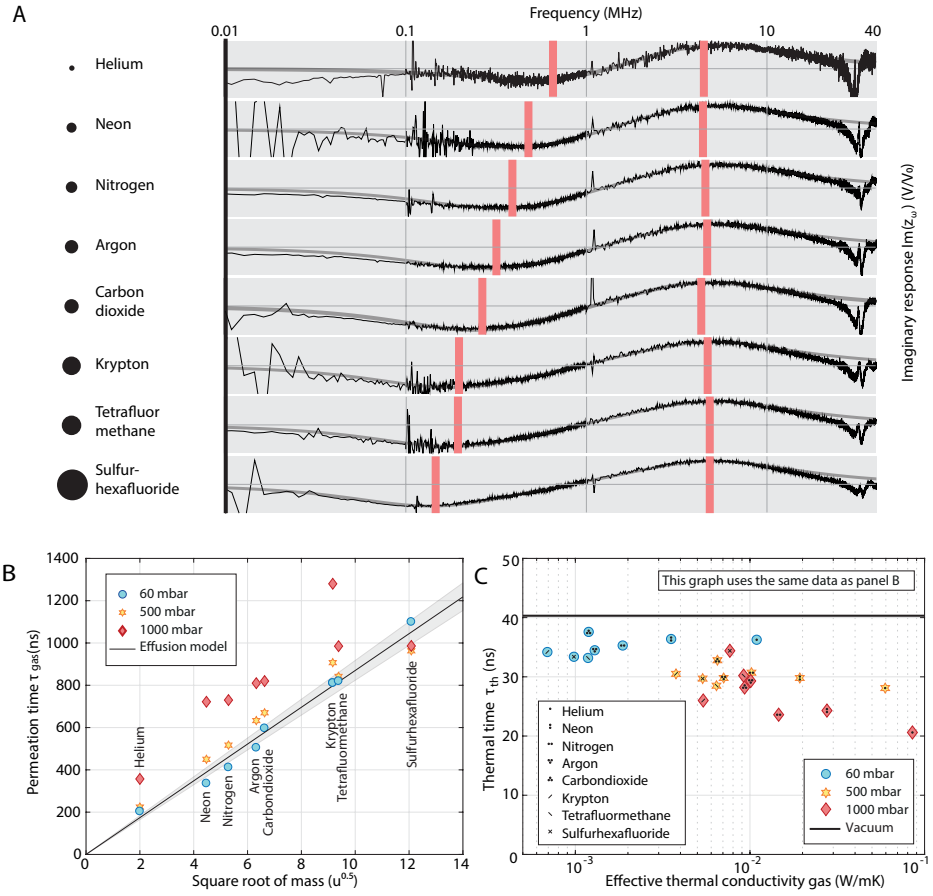

Figure 2.9: Measurements on a circular SLG drum show the same dip-peak characteristic shape as the dumbbell shaped devices. a) Data (black line) and fit to model (grey line) with the values found for τ_{th} and τ_{gas} indicated by pink marks. b) Permeation time constants follow Graham's law. The black line is a fit to the data at P = 60 mbar. c) Thermal time constants become lower with higher effective thermal conductivity.

CHARACTERIZATION OF MECHANICAL DEFORMATIONS INTRODUCED BY MILLING NANOPERFORATIONS AND CONTAMINATION

Milling pores in the graphene membranes can introduce mechanical deformations that affect the motion and read-out of the graphene. Introducing defects directly onto the surface of DLG membrane causes wrinkling with an amplitude of up to 15 nm and reduces signal quality. In the dumbbell geometry wrinkling is reduced by milling pores in the channel rather than directly on the drum, causing only a slight depression in the milled area as can be seen in Figure 2.10. The signal quality from samples perforated in the channel is considerably better compared to drums that are directly perforated. The AFM images also allow to quantify the amount of polymer contamination from the graphene transfer process. In general, contaminants are up to a few nm thick with a few big spots that are less than 15 nm thick. However, we do not expect contaminants to have a large impact on our measurements. The permeation time-constant is measured at frequencies much below the resonance frequency, where the membrane mass does not play a big role, and the permeation time constant is independent on the mass or stiffness of the membrane.

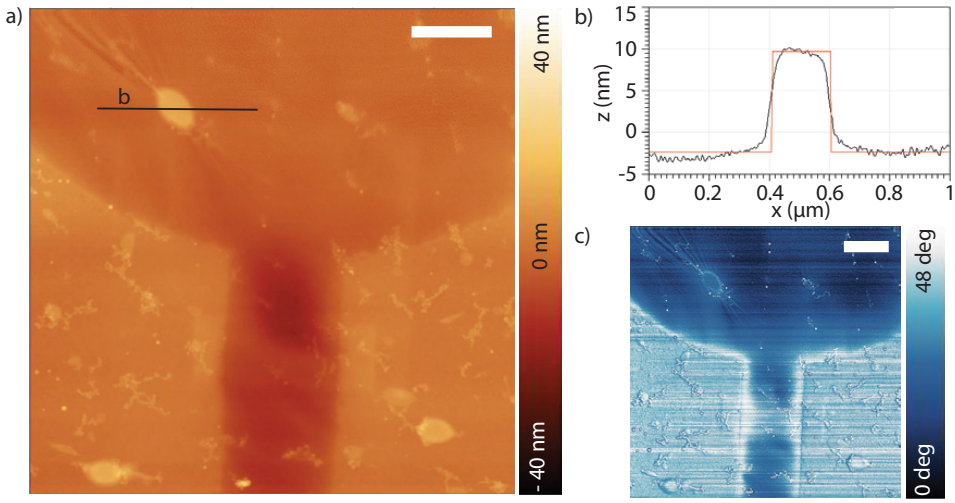

Figure 2.10: AFM characterization of the samples. a) AFM image of DLG sample with perforations at the channel entrance (n=256 and d=25nm). b) Line scan (black) over a large contamination with fitted height 12 nm (red). c) Phase channel AFM image of the same area as in a. Scalebars are 500 nm long.

DATASET ON GRAPHENE DRUM WITHOUT PERFORATIONS

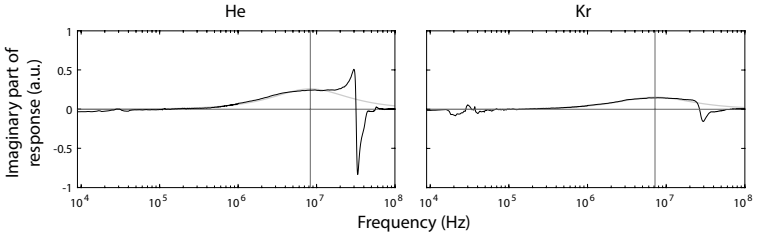

Figure 2.11: Data (black line) and fit to model (grey line) for He and Kr gas at P = 125 mbar measured on an unperforated, pristine sample. Vertical lines indicate the fitted position of the thermal peaks. Without perforations, we do not observe the permeation related dip.

ADDITIONAL DATASET

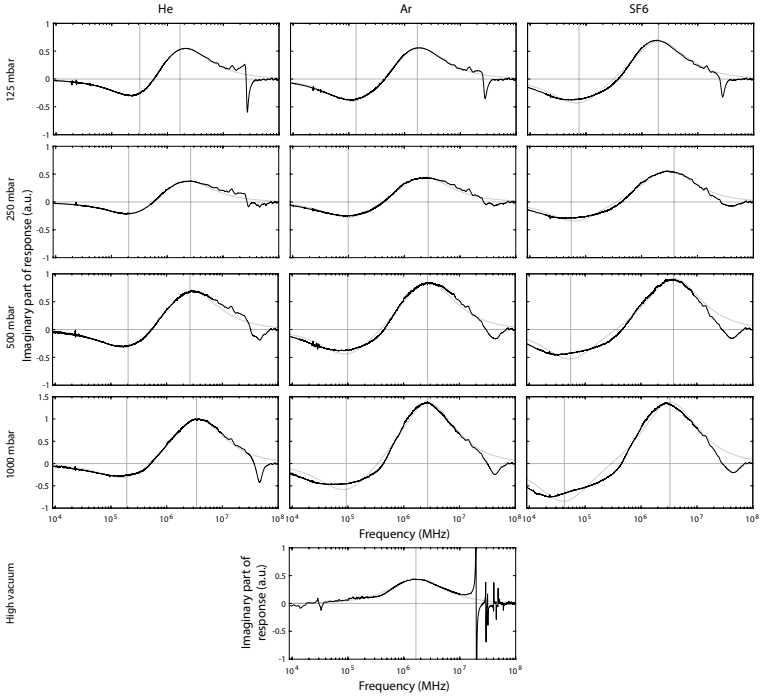

Figure 2.12: Data (black line) and fit to model (grey line) for 3 gasses at 4 different pressures measured on a sample with 256 pores of diameter 25 nm. Vertical lines indicate the fitted position of the permeation and thermal peaks. For comparison, a measurement on the same device in high vacuum is included. In high vacuum, we do not observe the permeation related dip.

BIBLIOGRAPHY

[1] P. Sun, Q. Yang, W. Kuang, Y. Stebunov, W. Xiong, J. Yu, R. R. Nair, M. Katsnelson, S. Yuan, I. Grigorieva, *et al.*, "Limits on gas impermeability of graphene," *Nature*, vol. 579, no. 7798, pp. 229–232, 2020.

[2] J. S. Bunch, S. S. Verbridge, J. S. Alden, A. M. Van Der Zande, J. M. Parpia, H. G. Craighead, and P. L. McEuen, "Impermeable atomic membranes from graphene sheets," *Nano Letters*, vol. 8, no. 8, pp. 2458–2462, 2008.

[3] O. Leenaerts, B. Partoens, and F. Peeters, "Graphene: A perfect nanoballoon," *Applied Physics Letters*, vol. 93, no. 19, p. 193107, 2008.

[4] Z. Yuan, J. D. Benck, Y. Eatmon, D. Blankschtein, and M. S. Strano, "Stable, temperature-dependent gas mixture permeation and separation through suspended nanoporous single-layer graphene membranes," *Nano letters*, vol. 18, no. 8, pp. 5057–5069, 2018.

[5] S. Huang, M. Dakhchoune, W. Luo, E. Oveisi, G. He, M. Rezaei, J. Zhao, D. T. Alexander, A. Züttel, M. S. Strano, *et al.*, "Single-layer graphene membranes by crack-free transfer for gas mixture separation," *Nature communications*, vol. 9, no. 1, p. 2632, 2018.

[6] L. Wang, M. S. Boutilier, P. R. Kidambi, D. Jang, N. G. Hadjiconstantinou, and R. Karnik, "Fundamental transport mechanisms, fabrication and potential applications of nanoporous atomically thin membranes," *Nature nanotechnology*, vol. 12, no. 6, pp. 509–522, 2017.

[7] L. Madauß, J. Schumacher, M. Ghosh, O. Ochedowski, J. Meyer, H. Lebius, B. Band'Etat, M. E. Toimil-Molares, C. Trautmann, and R. Lammertink, "Fabrication of nanoporous graphene/polymer composite membranes," *Nanoscale*, vol. 9, no. 29, pp. 10487–10493, 2017.

[8] R. Joshi, P. Carbone, F.-C. Wang, V. G. Kravets, Y. Su, I. V. Grigorieva, H. Wu, A. K. Geim, and R. R. Nair, "Precise and ultrafast molecular sieving through graphene oxide membranes," *Science*, vol. 343, no. 6172, pp. 752–754, 2014.

[9] S. C. O'Hern, M. S. Boutilier, J.-C. Idrobo, Y. Song, J. Kong, T. Laoui, M. Atieh, and R. Karnik, "Selective ionic transport through tunable subnanometer pores in single-layer graphene membranes," *Nano Letters*, vol. 14, no. 3, pp. 1234–1241, 2014.

[10] K. Celebi, J. Buchheim, R. M. Wyss, A. Droudian, P. Gasser, I. Shorubalko, J.-I. Kye, C. Lee, and H. G. Park, "Ultimate permeation across atomically thin porous graphene," *Science*, vol. 344, no. 6181, pp. 289–292, 2014.

[11] H. W. Kim, H. W. Yoon, S.-M. Yoon, B. M. Yoo, B. K. Ahn, Y. H. Cho, H. J. Shin, H. Yang, U. Paik, and S. Kwon, "Selective gas transport through few-layered graphene and graphene oxide membranes," *Science*, vol. 342, no. 6154, pp. 91–95, 2013.

[12] F. A. Nezhad, N. Han, Z. Shen, Y. Jin, Y. Wang, N. Yang, and S. Liu, "Experimental and theoretical exploration of gas permeation mechanism through 2D graphene (not graphene oxides) membranes," *Journal of Membrane Science*, vol. 601, p. 117883, 2020.

[13] A. Guirguis, J. W. Maina, X. Zhang, L. C. Henderson, L. Kong, H. Shon, and L. F. Dumée, "Applications of nano-porous graphene materials–critical review on performance and challenges," *Materials Horizons*, vol. 7, no. 5, pp. 1218–1245, 2020.

[14] J. Zhao, G. He, S. Huang, L. Villalobos, M. Dakhchoune, H. Bassas, and K. Agrawal, "Etching gas-sieving nanopores in single-layer graphene with an angstrom precision for high-performance gas mixture separation," *Science advances*, vol. 5, no. 1, p. eaav1851, 2019.

[15] D. Cohen-Tanugi and J. C. Grossman, "Water desalination across nanoporous graphene," *Nano Letters*, vol. 12, no. 7, pp. 3602–3608, 2012.

[16] K. Sint, B. Wang, and P. Král, "Selective ion passage through functionalized graphene nanopores," *Journal of the American Chemical Society*, vol. 130, no. 49, pp. 16448–16449, 2008.

[17] R. J. Dolleman, S. J. Cartamil-Bueno, H. S. van der Zant, and P. G. Steeneken, "Graphene gas osmometers," *2D Materials*, vol. 4, no. 1, p. 011002, 2016.

[18] W. Yuan and G. Shi, "Graphene-based gas sensors," *Journal of Materials Chemistry A*, vol. 1, no. 35, pp. 10078–10091, 2013.

[19] S. G. Chatterjee, S. Chatterjee, A. K. Ray, and A. K. Chakraborty, "Graphene–metal oxide nanohybrids for toxic gas sensor: a review," *Sensors and Actuators B: Chemical*, vol. 221, pp. 1170–1181, 2015.

[20] T. Wang, D. Huang, Z. Yang, S. Xu, G. He, X. Li, N. Hu, G. Yin, D. He, and L. Zhang, "A review on graphene-based gas/vapor sensors with unique properties and potential applications," *Nano-Micro Letters*, vol. 8, no. 2, pp. 95–119, 2016.

[21] T. Graham, "XXVIII. on the motion of gases," *Philosophical Transactions of the Royal Society of London*, no. 136, pp. 573–631, 1846.

[22] D. Davidovikj, D. Bouwmeester, H. S. van der Zant, and P. G. Steeneken, "Graphene gas pumps," *2D Materials*, vol. 5, no. 3, p. 031009, 2018.

[23] M. Schleberger and J. Kotakoski, "2D material science: Defect engineering by particle irradiation," *Materials*, vol. 11, no. 10, p. 1885, 2018.

[24] R. J. Dolleman, S. Houri, D. Davidovikj, S. J. Cartamil-Bueno, Y. M. Blanter, H. S. van der Zant, and P. G. Steeneken, "Optomechanics for thermal characterization of suspended graphene," *Physical Review B*, vol. 96, no. 16, p. 165421, 2017.

[25] D. Davidovikj, F. Alijani, S. J. Cartamil-Bueno, H. S. van der Zant, M. Amabili, and P. G. Steeneken, "Nonlinear dynamic characterization of two-dimensional materials," *Nature Communications*, vol. 8, no. 1, p. 1253, 2017.

[26] R. J. Dolleman, D. Lloyd, M. Lee, J. S. Bunch, H. S. Van Der Zant, and P. G. Steeneken, "Transient thermal characterization of suspended monolayer MoS2," *Physical Review Materials*, vol. 2, no. 11, p. 114008, 2018.

[27] M. v. Smoluchowski, "Zur kinetischen theorie der transpiration und diffusion verdünnter gase," *Annalen der Physik*, vol. 338, no. 16, pp. 1559–1570, 1910.

[28] P. Clausing, "The flow of highly rarefied gases through tubes of arbitrary length," *Journal of Vacuum Science and Technology*, vol. 8, no. 5, pp. 636–646, 1971.

[29] R. G. Livesey, *Flow of Gases Through Tubes and Orifices*. Wiley NJ, 1998.

[30] M. S. Boutilier, N. G. Hadjiconstantinou, and R. Karnik, "Knudsen effusion through polymer-coated three-layer porous graphene membranes," *Nanotechnology*, vol. 28, no. 18, p. 184003, 2017.

[31] S. Tison, "Experimental data and theoretical modeling of gas flows through metal capillary leaks," *Vacuum*, vol. 44, no. 11-12, pp. 1171–1175, 1993.

[32] A. Castellanos-Gomez, R. van Leeuwen, M. Buscema, H. S. van der Zant, G. A. Steele, and W. J. Venstra, "Single-layer mos2 mechanical resonators," *Advanced Materials*, vol. 25, no. 46, pp. 6719–6723, 2013.

[33] R. J. Dolleman, S. Houri, A. Chandrashekar, F. Alijani, H. S. van der Zant, and P. G. Steeneken, "Opto-thermally excited multimode parametric resonance in graphene membranes," *Scientific Reports*, vol. 8, no. 1, p. 9366, 2018.

[34] G. Reichenauer, U. Heinemann, and H.-P. Ebert, "Relationship between pore size and the gas pressure dependence of the gaseous thermal conductivity," *Colloids and Surfaces A: Physicochemical and Engineering Aspects*, vol. 300, no. 1-2, pp. 204–210, 2007.

[35] V. Antonetti, A. Bar Cohen, and A. Bergles, *Fluid Flow Databook*. Genium Publishing, 1981.

[36] D. Singh, X. Guo, A. Alexeenko, J. Y. Murthy, and T. S. Fisher, "Modeling of subcontinuum thermal transport across semiconductor-gas interfaces," *Journal of Applied Physics*, vol. 106, no. 2, p. 024314, 2009.

3

3

PROBING NANOMOTION OF SINGLE BACTERIA WITH GRAPHENE DRUMS

Assembled in a crowd, people lose their powers of reasoning, and their capacity for moral choice.

Aldous Huxley

Motion is a key characteristic of every form of life [1]. Even at the microscale, it has been reported that colonies of bacteria can generate nanomotion on mechanical cantilevers [2], but the origin of these nanoscale vibrations has remained unresolved [3, 4]. Here, we present a novel technique using drums made of ultrathin bilayer graphene, where the nanomotion of single bacteria can be measured in its aqueous growth environment. A single E. coli cell is found to generate random oscillations with amplitudes of up to 60 nm, exerting forces of up to 6 nN to its environment. Using mutant strains which differ by single gene deletions that affect motility, we are able to pinpoint the bacterial flagella as the main source of nanomotion. By real-time tracing of changes in nanomotion upon administering antibiotics, we demonstrate that graphene drums can perform antibiotic susceptibility testing with single-cell sensitivity. These findings deepen our understanding of processes underlying cellular dynamics, and pave the way towards high throughput and parallelized rapid screening of the effectiveness of antibiotics in bacterial infections with graphene devices.

This chapter has been published in the journal Nature Nanotechnology **17**, 637–642 (2022).
The published article is adapted to fit into the context of this thesis.

LIVING cells exhibit nanomechanical vibrations as a result of the biological processes that govern their growth, function, and reproduction [5]. This nanomotion is an intriguing phenomenon of unravelled origin that has been observed in a wide variety of living organisms, including neuronal cells [6], erythrocytes, yeasts [6, 7], and bacteria [4]. Numerous hypotheses have been proposed for the underlying driving mechanism, such as motion of organelles, internal redistribution of cell membranes [9] and the action of ion pumps [3], but consensus has not been reached [4]. This relates to the fact that non-invasive probing of biomechanics at the microscale is highly challenging, which has stimulated the development and application of techniques like atomic force microscopy [10–12] (AFM), optical and magnetic tweezers [13], flow cytometry [14], and optical tracking of cells [15, 16]. In particular for bacterial cells, micromechanical cantilevers have emerged as powerful tools for detecting vibrations of adhered cell populations (100-1000 bacteria) in a liquid environment [4]. It was shown that the nanomotion of these populations rapidly decreases in the presence of antibiotics, which holds great promise for the development of rapid antibiotic susceptibility testing technologies [2]. Both for probing fundamental biomechanical processes and for development of nanomotion-based antibiotic susceptibility tests in medical diagnostics, it is crucial to elucidate the microscopic origins of nanomotion.

Here, we present a novel single-cell technique based on suspended graphene drums [17], which greatly enhances the sensitivity of nanomechanical sensing compared to previous cantilever-based methods. The ultra-high sensitivity of the technique allowed us to clarify the mechanism that lies at the root of bacterial nanomotion by probing various strains of Escherichia coli (*E. coli*). The small mass, high stiffness, and micron-sized area of a suspended graphene drum enables detecting nanomotion at even the single bacterium level. Using arrays of these drums, we compare the vibrations produced by different *E. coli* strains. In particular, we investigate the contributions of the bacterial cell wall synthesis, flagella, rotor, and ion pump to nanomotion, and demonstrate that flagellar motion is the main source of nanomotion in these bacteria. Moreover, by tracing the nanomotion in the presence of antibiotics, we show that this novel ultrasensitive graphene-based platform enables antibiotic susceptibility tests with single-bacterium sensitivity. This opens new routes towards faster, label-free detection of antimicrobial resistance at the single-cell level with potential applications in drug screening and rapid diagnostics.

3.1. GRAPHENE DRUMS FOR PROBING A SINGLE BACTERIUM

The experiments were performed using drums made of ultrathin (<1 nm) bilayer CVD graphene that covered circular cavities with a diameter of 8 μm and a depth of 285 nm that were etched in SiO_2. A silicon chip with an array of thousands of these graphene-covered cavities was placed inside a cuvette containing *E. coli* in Lysogeny Broth (LB) medium, where APTES was used to bind the bacteria to the graphene surface (see Annex and Methods). The nanomotion of a bacterium resulted in a deflection of the suspended membrane, which was measured using laser interferometry [18], see Figure 3.1a. The bacterium induced a time-dependent deflection $z(t)$ at the center of the suspended graphene drum, which can be determined from the modulation of the intensity of the reflected light [19]. To quantitatively compare the nanomotion of different drums, we

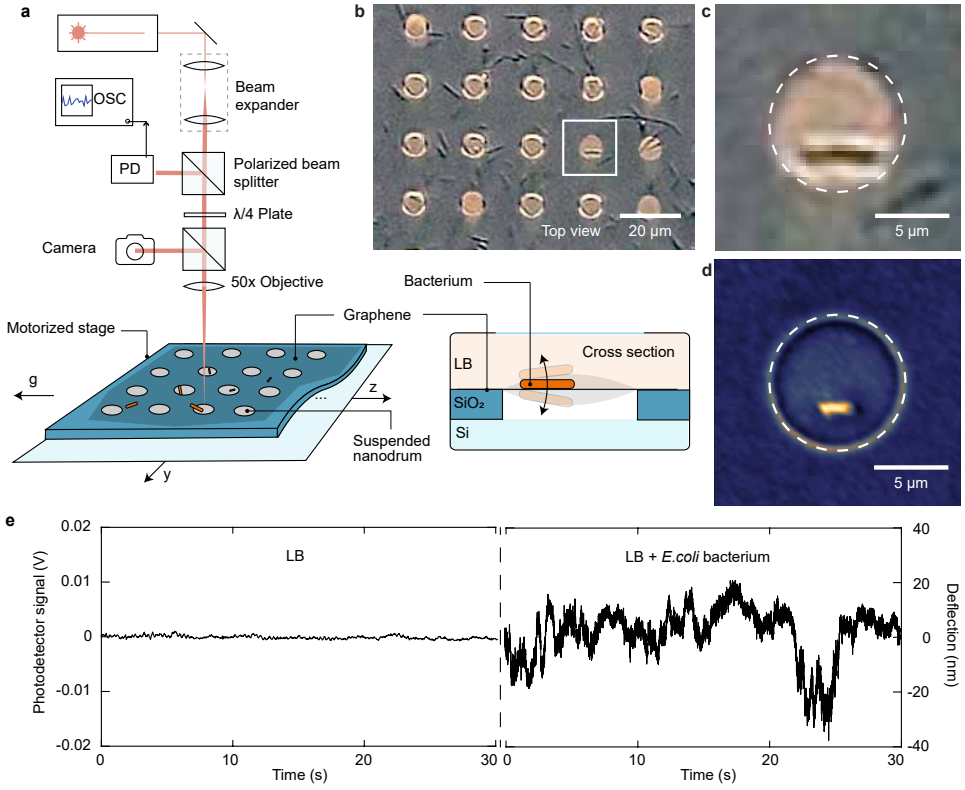

Figure 3.1: *Detection of nanomotion of single bacteria by graphene drums.*
a) Schematic of the interferometric measurement setup used to record the nanomotion. b) Optical microscope image of an array of suspended drums with adhered *E. coli*. c) Zoom of the area indicated by a white square in panel b, showing a dividing bacterium on top of a graphene drum. d) SEM image of an *E. coli* on a suspended graphene drum. e) Recorded deflection of a suspended graphene drum immersed in LB without a bacterium (left), compared to the signal from a graphene drum with a bacterium present (right).

acquired $z(t)$ traces over 30 second periods to obtain the variance $\sigma^2 = \langle z^2(t) \rangle$, or the motion amplitude σ, which we used as a measure of the magnitude of the nanomotion.

Drums containing a single live bacterium (Figure 3.1b-d) displayed large displacements $z_{\max}$ of up to 60 nm, with a time averaged motion amplitude of up to $\sigma = 20$ nm, that clearly exceed the deflection of drums without bacteria and signal from cells deposited on the Si/SiO_2 substrate away from the drums, which yielded a background $\sigma = 2$ nm (see Figure 3.1e and Annex). The large oscillation amplitudes can be associated with the movement of the suspended drum and originate from bacterial biophysical processes. To characterize the motion further, we recorded the signal of a single bacterium for more than 1 hour. It is apparent that fluctuations were present that show similarities over different timescales, see Figure 3.2a. Fluctuations were also observed on timescales ranging from seconds to hours. Figure 3.2b displays the power spectral density of the motion (black line), compared to the background signal of an empty drum. The spectra

have a $1/f^{\alpha}$ frequency dependence, with a mean value of $\alpha = 1.8 \pm 0.1$ ($n = 277$ graphene drums; Figure 3.2c). The difference between drums with and without a single bacterium can also be clearly perceived by listening to audio recordings that were generated by converting the interferometric traces to a sound track. These results are consistent with power spectral densities found for bacterial colonies on AFM cantilevers [20], and show that the nanomotion generated by even a single *E. coli* bacterium lacks a specific periodicity but instead involves a wide range of frequencies.

3.2. IMPACT OF FLAGELLAR MOTILITY ON NANOMOTION

While various origins of nanomotion have been proposed [3, 4], we speculate that flagellar motility constitutes the major source. To clarify its role on the bacterial forces generated, we compare the nanomotion of four *E. coli* strains (Figure 3.3a) that were genetically modified to have varying levels of motility: a hyper-motile strain with a larger number of flagella compared to wildtype, a minimally motile strain that lacks the regulatory IS1 element for the flagellum synthesis [21, 22], a non-motile strain with disabled flagellar motors, and a flagella-less strain where the motors are functional but flagella are lacking. As a fifth case, we studied the overall influence of ion pumps on the nanomotion by administering cadaverine, a drug, that blocks ionic transport through the cell membrane [23] and thus reduces cell motility.

The histograms in Figure 3.3b compare the motion of hyper-motile bacteria before and after exposure to cadaverine. The motion amplitude σ is observed to be substantially lowered after adding the drug (the median reduced from $\sigma = 13.4$ nm to 7.0 nm before and after administering cadaverine, respectively), indicating that the bacterial motion was strongly reduced, although it did not get fully quenched. The level of motility was observed to have a large influence on the magnitude of the nanomotion signal, as shown in Figure 3.3c. We observed that the nanomotion from the strains with both functional flagella and motors (median of $\sigma = 13.4$ nm for hyper-motile and $\sigma = 12.6$ nm for minimally-motile strains) was significantly larger than from strains in which either the motor was disabled or the flagella was removed (median variance $\sigma = 5.3$ nm for non-motile, and $\sigma = 2.6$ nm for flagella-less strains). We conclude that the observed differences in nanomotion are mainly induced by the activity of flagella, since the nanomotion disappeared in the flagella-less strain and the amplitude clearly correlates with the activity of the flagella.

3.3. ANTIBIOTIC SUSCEPTIBILITY TESTS ON SINGLE BACTERIA

Subsequently, we explored if antibiotic susceptibility tests can be performed on single *E. coli* bacteria by monitoring nanomotion of graphene drums. To test the efficacy of different antibiotics, we measured the nanomotion variance σ^2 of each drum for 30 seconds, both before and 1 hour after administering an antibiotic above its minimum inhibitory concentration (MIC). Figure 3.4a shows the 6 different antibiotics that we tested and their mode of action. For the antibiotics rifampicin, ciprofloxacin, DNP, and chloramphenicol, a decrease in the nanomotion was observed (Figure 3.4b-f and Table 1). Initially, a median motion amplitude $\sigma = 7$ nm is observed for the AB1157 *E. coli* strain, but quickly after administering the antibiotic the amplitudes drop to median values around

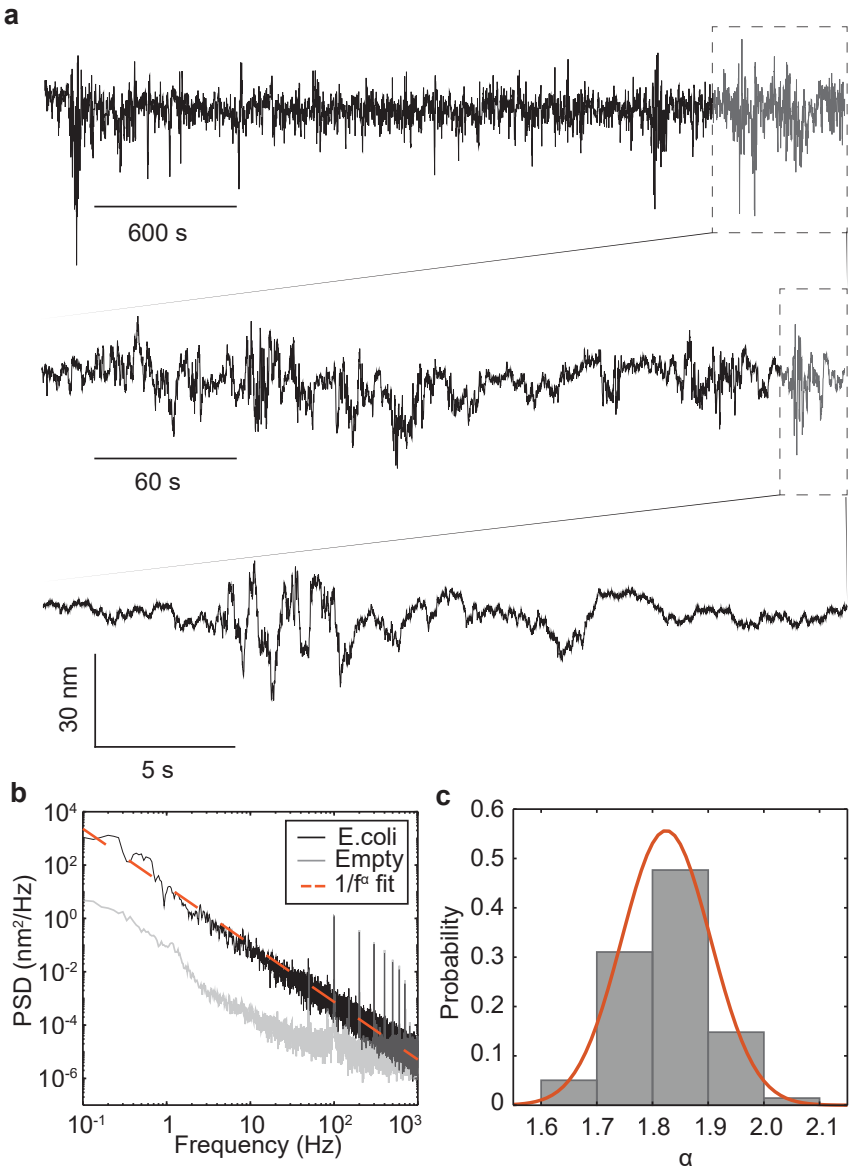

Figure 3.2: *Motion of a single bacterium.*
a) Deflection $z(t)$ versus time for a graphene drum with a single *E. coli* in LB, recorded for one hour. By zooming in on the part indicated in grey, while maintaining the same y-axis scale, it is observed that fluctuations are present over a wide range of timescales. b) Amplitude power spectral density (PSD) of the time-trace shown in 3.2a, of a live bacterium (black) and for the baseline from an empty drum (grey). Dashed orange line is a fit to $1/f^{\alpha}$ spectrum with $\alpha = 2.1$. The background spectrum is significantly lower and shows enhanced noise at frequencies below 1 Hz and a flatter noise spectrum above 100 Hz. Peaks appear at harmonics of 50 Hz due to mains interference. c) Probability distribution of α from fitting $1/f^{\alpha}$ noise. Orange line represents a Gaussian fit to the distribution, yielding an average value of $\alpha = 1.8 \pm 0.1$ (mean $\pm$ S.D.) ($n = 277$ samples).

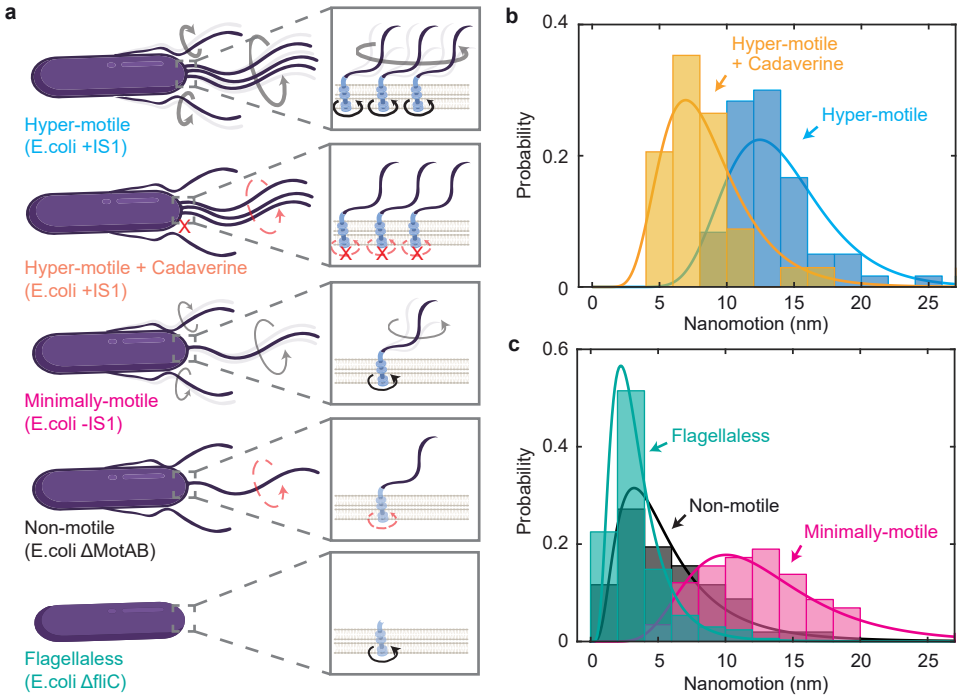

Figure 3.3: *Impact of flagellar motility on nanomotion.*
a) To study the influence of motility on nanomotion, the following strains are compared: hypermotile, hypermotile with motility impaired by cadaverine, minimally motile by a genetic blocker, non-motile by gene deletion, and flagella-less. Red cross indicates a blocked ion pump and red dashed arrow indicates a disabled motor. b) Histogram of the motion amplitude σ of hyper-motile bacteria before (blue, $n = 60$) and after (yellow, $n = 34$) administering cadaverine, showing reduction of nanomotion. c) Motion σ of minimally-motile *E. coli* (purple, $n = 58$) is compared to the non-motile strain (black, $n = 103$) and the flagella-less strain (turquoise, $n = 169$). The non-motile and flagella-less strains showed significantly lower motion than the minimally motile strain. Lines represent lognormal fits to the distributions.

σ = 3 nm. The cells are not viable after antibiotic treatment, as the motion does not increase back to its original level when the antibiotic is flushed out with LB (see Annex, similar to earlier reports [2]). These results show that one can use graphene drums for testing antibiotic susceptibility based on nanomotion.

To test whether graphene drums are able to distinguish resistant cells, we used *E. coli* cells with chromosomal KanR resistance gene [24] . When these cells were exposed to kanamycin, we observed no change in the motion amplitude (σ 5 nm) (Figure 3.4d). However, when we subsequently exposed the same cells to chloramphenicol, we did observe a decrease in the signal with respect to the initial nanomotion (down to σ = 1.8 nm). Additionally, we treated *E. coli* cells with A22 which alters cell wall synthesis. We used sub-MIC concentrations of the drug, such that the bacteria lose their typical rod shape and become rounded (see Annex) without killing the cells or impairing their division and motility [25–28]. In contrast to the effect of the other antibiotics, the variance of cells grown in presence of A22 was found to be similar to that of the untreated cells, and disruption of the cell-wall synthesis was not observed to result in a reduction in the nanomotion.

Besides detecting differences in nanomotion between strains, or after administering antibiotics, the graphene platform also offers the possibility of real-time probing of the decrease in vibration amplitude, providing on-the-fly information on the route to bacterial death. From long-time trace measurements such as Figure 3.4e (and Annex), we found that most of the nanomotion fades within the first hour after exposure to antibiotics. We also note that after adding the antibiotic the power spectral density (PSD) drops down to the level of an empty drum (Annex).This experiment demonstrates the potential of graphene devices as an indicator of bacterial physiology, and opens new routes for determining the temporal response of bacteria to antibiotics at single cell level.

3.4. CONCLUSIONS

We present an ultrasensitive platform that uses graphene drums to measure nanomotion of single bacterial cells. Single *E. coli* bacteria were observed to produce peak fluctuations of up to 60 nm in amplitude, that correspond to forces of up to 6 nN as inferred from the graphene membrane stiffness of $k \approx 0.1$ N/m (see Methods). These forces are larger than the typical forces generated by a single molecular motor [29] ($F \approx 10$ pN) or a single flagellar motor [30, 31] ($F \approx 100$ pN), indicating that multiple molecular motors and flagella contribute collectively to the observed force. By comparing the nanomotion of different strains of bacteria, we conclude that flagellar motion is the major contributing factor to the nanoscale vibrations. It is worth noting though, that flagellar motility is not the only source of nanomotion, as it was observed even in flagella-less *E. coli* and natural atrichous *B. subtillis* (see Figure 3.9), albeit at significantly lower amplitude.

Our platform expands upon the available tools for single-cell analysis, such as high-resolution fluorescence microscopy, and sets a new benchmark for sensitivity with respect to the available nanomotion method using cantilevers. Single-cell data have many useful properties; they allow for the identification and study of persister cells, that are related to the emergence of antibiotic resistance [32] within a population, and can be obtained at a lower specimen concentration. In contrast to fluorescence microscopy, nanomotion detection is a label-free technique, and thus can be applied directly on

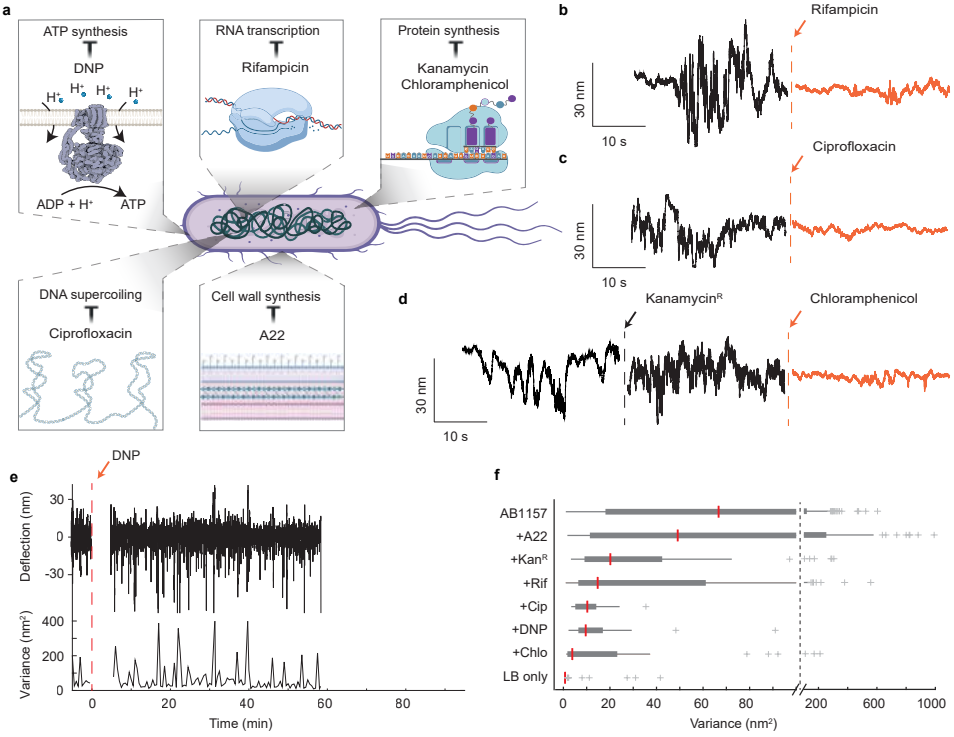

Figure 3.4: *Single-cell antibiotic sensitivity screening using graphene.*
a) Schematic of antibiotics used in this work and their respective mode of action. b,c) Recorded motion of a drum with *E. coli* before (black) and after exposure to antibiotics (orange). d) Recorded motion of a drum with a kanamycin-resistant *E. coli* bacterium before (black), and after 1 hour of exposure to kanamycin, and subsequently after 1 hour of exposure to chloramphenicol. e) Recorded deflection (upper trace) that starts 6 minutes after DNP drug injection at t=0 min (vertical orange dashed line). A moving average is used to calculate the variance (below) using a window of 30'. f) Box plot for all measurements after administering the corresponding drug to the *E. coli* strain AB1157 ($n = 277$), +A22 ($n = 108$), +kanamycin ($n = 33$), +rifampicin ($n = 83$), +ciprofloxacin ($n = 36$), +DNP ($n = 27$), +chloramphenicol ($n = 33$), as well as for empty control drums in LB ($n = 80$). Box plot indicates the 25th, 50th (red line is the median) and 75th percentiles, whereas whiskers extend to maximum 1.5 times the interquartile distance. Outliers are indicated by a cross.

clinical samples for antibiotic sensitivity screening. Whereas cantilevers can be used to resolve nanomotion in a large aggregate of at least several hundreds of bacteria [4], a graphene drum accommodates single bacteria and its different geometry results in a reduced damping and thermal noise, allowing smaller forces to still be distinguished from the noise floor. Graphene is strong, inert, thin and couples well to light, which makes it stand out among 2D materials as a support material for nanomotion sensing and is well-suited to be massively parallelized.

Recent reports call for the development of effective diagnostic tools to detect antimicrobial resistance and slow down the emergence of multi-drug resistant bacteria by prescribing the correct drug [33]. Our antibiotic susceptibility experiments demonstrated that the graphene drum sensing platform can trace the effect of antibiotics on bacterial nanomotion in real-time. This opens the way to fast, label-free susceptibility testing down to the single bacterial level. In comparison to other techniques for detecting antibiotic susceptibility [34], the method presented here stands out in terms of sensitivity and speed, offering for the first time the capability to quantify the nanomotion at the level of individual bacteria within a timeframe of 30 seconds. The small size of the graphene drums enables high-throughput sensing, allowing, in principle, millions of cells to be monitored in parallel in the presence of antibiotics. Similar benefits might apply in the field of personalised medicine, where the right antibiotic can be rapidly selected based on the nanomotion response.

Furthermore, directed evolution experiments may benefit from this technique as a fast selection and screening method [35], as the density of over 10.000 nanomotion sensors/mm2 can result in a greatly increased throughput as compared to 96-well plates or petri-dish culturing. With the significant reduction in size and increase in sensitivity presented in this work, nanomotion detection potentially can evolve into an important non-invasive monitoring tool in cell biology and provide new routes for rapid screening tests in personalized medicine and drug development.

3.5. METHODS

Amplitude calibration Here we describe how the drum deflection $z(t)$ was obtained from the reflected intensity variations $I(t)$ of the red laser that was reflected by the photodiode voltage $V_{\mathrm{pd}}(t)$. We first define the reflection coefficient $R(t) = I(t)/I_0$, where I_0 is the incident light intensity and $I(t)$ is the reflected light intensity. The reflection coefficient $R(t)$ depends on the optical characteristics of the cavity formed between the graphene and the silicon and the position $z(t)$ of the graphene membrane. Light passes subsequently through three media with the following refractive indices: LB media with $n_{\mathrm{LB}} = 1.34 - 0.0007i$, graphene with $n_{\mathrm{gr}} = 2.7 - 1.6i$, air with $n_{\mathrm{air}} = 1$, and finally the light was reflected from the silicon mirror $n_{\mathrm{si}} = 4.2 - 0.06i$, where i is the imaginary unit. Together, the semi-transparent graphene layer and the reflective silicon form a Fabry-Pérot cavity. The reflected light is modulated by the graphene drum moving through the optical field, and the reflection coefficient $R = I/I_0$ can be described by the following equation [38]:

$$R = [(r_1 + r_2 e^{-i\delta_1} + r_3 e^{-i\delta_2} + r_1 r_2 r_3 e^{-i\delta_1+\delta_2}))/(1 + r_1 r_2 e^{-i\delta_2} + r_1 r_3 e^{-i\delta_1+\delta_2}) + r_2 r_3 e^{-i\delta_2})]^2, \tag{3.1}$$

Table 3.1: Efficacy of antibiotics measured 1 hour after exposure. Median value of the variance before and after exposure are compared, and the probability (p-value) that the drug has no effect on the nanomotion variance is evaluated using a two-tailed rank test. For all antibiotics except A22, a two-tailed Wilcoxon signed rank test is performed for paired measurements before and after exposure to the antibiotic. For A22, a two-tailed Wilcoxon rank sum test is performed with respect to *E. coli* AB1157. Superscript R indicates antibiotic resistance and significance is expressed using the asterisk convention.

Antibiotic	Number of drums measured (n)	Median variance before exposure (nm^2)	Median variance 1 h after exposure (nm^2)	p-value
A22	108	66.7	49.1	0.83ns
Kanamycin^R	33	32.3	20.2	0.11ns
Rifampicin	83	92.6	14.7	$\leq$ 0.0001****
Ciprofloxacin	36	18.8	10.3	0.00030***
DNP	27	94.8	9.6	$\leq$ 0.0001****
Chloramphenicol	33	32.3	3.4	0.0091**

Table 3.2: Table describing the types and concentrations of antibiotics used (see also Figure 3.4a)

Antibiotic	**Target**	**Mechanism**	**Concentration**
A22	Cell wall synthesis	Inhibits MreB filament polymerization	5 µg/ml
Kanamycin	Translation	Binds ribosome and interferes in elongation of polypeptide chain elongation	50 µg/ml
Chloramphenicol	Translation	Binds to ribosome and inhibits binding of tRNA	34 µg/ml
Ciprofloxacin	DNA Supercoiling homeostasis	Traps topoisomerase and DNA in a complex, inhibits DNA rejoining after cleavage	15 µg/ml
Cadaverine	Ion transport	Induces closure of porins and inhibits ion transport over the membrane	50 mM
Rifampicin	Transcription	Binds to RNAP and blocks the elongating RNA molecule	50 µg/ml
DNP	H+ gradient across the membrane	Inhibits ATP synthesis	2 mM

where $r_1 = (n_{LB} - n_{gr})/(n_{LB} + n_{gr})$, $r_2 = (n_{gr} - n_{air})/(n_{gr} + n_{air})$ and $r_3 = (n_{air} - n_s i)/(n_{air} + n_s i)$, and the exponent δ is the phase difference that the light of wavelength λ acquires while travelling through a medium of thickness t. In this case $\delta_1 = (2\pi n_{gr} t_{gr})/\lambda$ and $\delta_2 = (2\pi n_{air} t_{air})/\lambda$, with $t_{air} = g + z(t)$. The reflectivity of the cavity depends on the number of graphene layers and the cavity depth, as plotted in Extended Data Figure 1a, where the reflectivity for bilayer graphene is indicated by a red line. The design cavity depth is 285 nm, however the drums bulged down by typically 60 nm under pressure of the liquid as can be seen in the liquid AFM image (Figure 3.15. Therefore, we consider that the effective cavity depth was g=225 nm. Then, we normalized the reflectivity by dividing it over R at a cavity depth of 225 nm (R_0), to find the slope around that point, which equals $\phi = d(R(t)/R_0)/dz = -0.0038\ \text{nm}^{-1}$, as indicated in Extended Data Figure 1b.

Data was gathered by an oscilloscope measuring the voltage $V_{pd}(t)$ from the photodiode that is proportional to the reflected light intensity and is operated in its linear range. The gathered time trace was normalized by division over its average, $V_{norm} = V_{pd}(t)/ < V_{pd}(t) >$, and a linear fit was subtracted from the data to eliminate the effects of drift during the measurement. Using the calibration factor ϕ, the deflection $z(t)$ was calculated as $z(t) = [V_{pd}(t)/ < V_{pd}(t) > -1]/\phi$.

While the current nanomotion detection technique works well for qualitative analysis of changes in the bacterial nanomotion in time, there are several approximations made in the conversion from the nanomotion-induced light-intensity variations detected by the photodiode to a nanomotion amplitude in nm. First of all, the nanomotion generated by a bacterium may depend on its position on the drum, which could cause experimental variations. In our calculations of the force, we assume that a single bacterium is centered on the drum. Moreover, in the optical model, the cavity underneath the graphene is assumed to be filled by air. The use of bilayer graphene minimizes the chances that small defects cause leakage and liquid AFM measurements (see Figure 3.15) also showed that the graphene membranes bulge down, which is to be expected if the cavity is air filled. Finally, the bacterium is attached to the surface of the graphene and is likely to be in the laser beam path. The refractive index of an *E. coli* bacterium [39, 40] ($n = 1.33$) is very close to that of the LB medium ($n = 1.34$), causing the bacteria to be nearly transparent and therefore we estimate this to have negligible impact on the nanomotion amplitude determination.

Estimation of the stiffness and noise floor of a graphene drum We estimate the stiffness k_1 of the circular graphene drum with area $A = 50\ \mu\text{m}^2$ based on the deflection z at the centre of the membrane with respect to a flat configuration induced by uniform liquid pressure P in the cuvette. Hooke's law prescribes that the stiffness can be found by equating forces: $k_z = PA$. The graphene drum is immersed 1 cm below the surface of the liquid and is therefore under a uniform pressure of 100 Pa. Under these conditions the graphene is found to deflect 60 nm downward, as measured by liquid AFM (see annex). By inserting these values in the equation above, we find $k = 0.14$ N/m. Our estimate of the stiffness of graphene drums corresponds to values reported in literature [41–43], which typically range from 0.05 to 1 N/m.

Next, we estimate the amplitude noise floor of the empty graphene drums to estimate the minimum detectable nanomotion level. The mean square force noise on

a harmonic oscillator with a damping constant c is given by $\langle F^2 \rangle = 4k_B TcBW$, where k_B is Boltzmann's constant, T is the temperature and BW is the measurement bandwidth. Far below the resonance frequency, the variance in the amplitude is given by $\sigma_{empty} = \langle F^2 \rangle / k^2$, which is proportional to c. For a circular graphene drum, the damping constant c (N·s/m) can be roughly approximated from Stokes' law, assuming a spherical particle moving through a fluid, $c = 6\pi\mu R$, where for our drum the radius $R = 4$ micron and $\mu = 0.001$ Pa·s for water at 20 °C, which yields $c = 7.5 \cdot 10^{-8}$ N s/m. In the case of cantilevers [44], typical damping constants are $c \approx 1 \cdot 10^{-6}$ N s/m. Thus the empty drums have a damping constant, and nanomotion variance, that is over a factor 10 lower than that of AFM cantilevers, resulting in a higher signal-to-noise ratio, which facilitates single-cell motion detection.

3.6. ANNEX

OPTICAL CHARACTERIZATION

Chips with graphene drums, dimensions 5x5 mm^2, were first inspected under a microscope. Not all drums were successfully suspended after fabrication of the device and transfer of the graphene. The drums which were intact could be recognized as they showed up darker than collapsed drums under a blue filter, as can be seen in Figure 3.5a. Once the position of intact drums in the array was known, the chip was fixed inside a cuvette and the growth medium containing bacteria was added. The chip is placed in horizontal position, such that the bacteria sediment on the surface of the chip. Approximately 20 minutes of deposition was required to obtain an average coverage of 1 bacterium per drum in our setup with a growth medium at $OD_{600} = 0.2 - 0.3$. Once this time had elapsed, the chip was placed vertically to stop deposition of more bacteria. The sample was again inspected under the microscope to check if the bacteria are well adhered. Figure 3.5b shows an example of an array of graphene drums with adhered cells. The sample was then placed in the laser interferometry setup in which the nanomotion can be observed by focusing the laser spot on one of the drums.

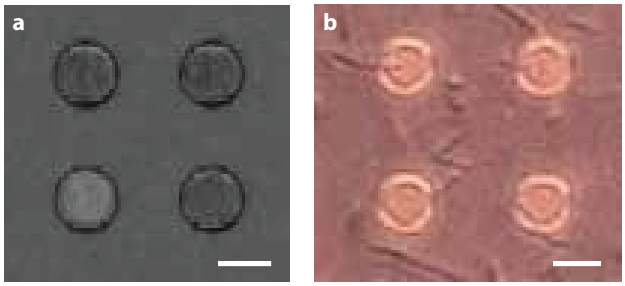

Figure 3.5: The array of graphene drums was inspected optically before and after deposition of the bacteria. a) Intact drums can be recognized as they show up darker than collapsed drums under a blue filter. Only the intact drums were measured. b) An array of membranes with *E.coli* after deposition. The chip was placed in upright position within the liquid chamber, to ensure that the bacteria are well attached and no more bacteria attach on the surface. Scalebars are 10 μm long.

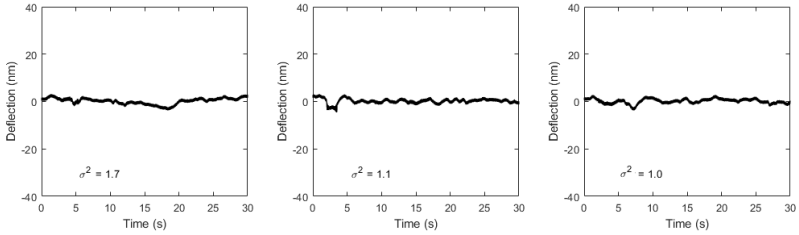

Figure 3.6: Measurement of nanomotion on drums without bacteria in LB.

CONTROL EXPERIMENTS ON DRUMS WITHOUT BACTERIA

We performed control experiments to establish whether the bacteria are the source of the nanomotion. First, a experiment was performed without bacteria on an array of suspended drums in LB growth medium. We detected a motion amplitude below $\sigma^2 = 4$ nm^2 on these drums, which is the noise floor for our measurements and is referred to in the main text as baseline. We tested the noise values within two batches in LB only (without bacteria). For the first batch we measured $\sigma^2 = 2 \pm 0.7$ nm^2 (mean ± standard error of the mean of σ^2, n = 80). In the second batch we measured $\sigma^2 = 3 \pm 0.5$ nm^2 (n = 85). Three typical traces are shown in Figure 3.6. We also performed a second type of control experiments to establish that the graphene drums are needed to transduce and read the nanomotion. In this experiment the laser was focused on AB1157 bacteria attached to the Si/SiO_2 substrate, outside of the suspended area. Here, we also detected a motion amplitude below $\sigma^2 = 4$ nm, much lower than the signals from bacteria on suspended graphene. Three typical traces are shown in Figure 3.7.

EXTENDED MEASUREMENT DATA - STRAINS

To study the influence of motility on the observed nanomotion, we studied six cases: hypermotile, hyper-motile with motility impaired by cadaverine, minimally motile by ge-

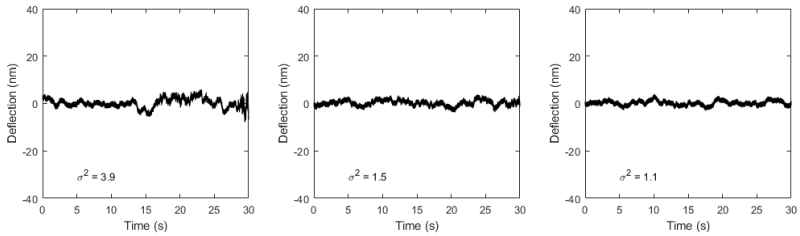

Figure 3.7: Measurement of nanomotion measured with the laser focused on a bacterium on the substrate, outside of the suspended area.

netic blocker, non-motile by gene deletion, flagellaless *E. coli*, and naturally non-motile *B. subtillis*. Here, we show typical traces for each of these cases as a supplement to the data presented in Figure 3.3 in the main text.

The various *E. coli* strains used in this work are listed in Table 3.3. The median value of the nanomotion measured varied between strains. The motility of a strain was inferred from the biofilm formation on an agar plate [45], and is listed in the column *Motility* for comparison. The motility correlates with the magnitude of nanomotion we found in this study. This is consistent with the notion that motility is indeed an important contributor to the observed nanomotion. Finally, we performed measurement on gram-positive, non-motile *B.subtillis*, which moves with a median nanomotion variance of 8 nm^2 (n=10). Three typical traces are shown in Figure 3.9.

Table 3.3: List of bacterial strains used in this research and their description.

Strain	**Description**	**Motility**	**Median variance (nm^2)**	**Number of samples (-)**
AB1157	Normal	Low	67	277
MG1655 (+IS1)	Hyper-motile	High	170	60
MG1655 (-IS1)	Minimally-motile	Medium	158	58
MG1655 (motAB)	Non-motile	None	28	103
MG1655 (fliC)	Flagellaless	None	8	169
B.subtillis	Bacillus	None	8	10

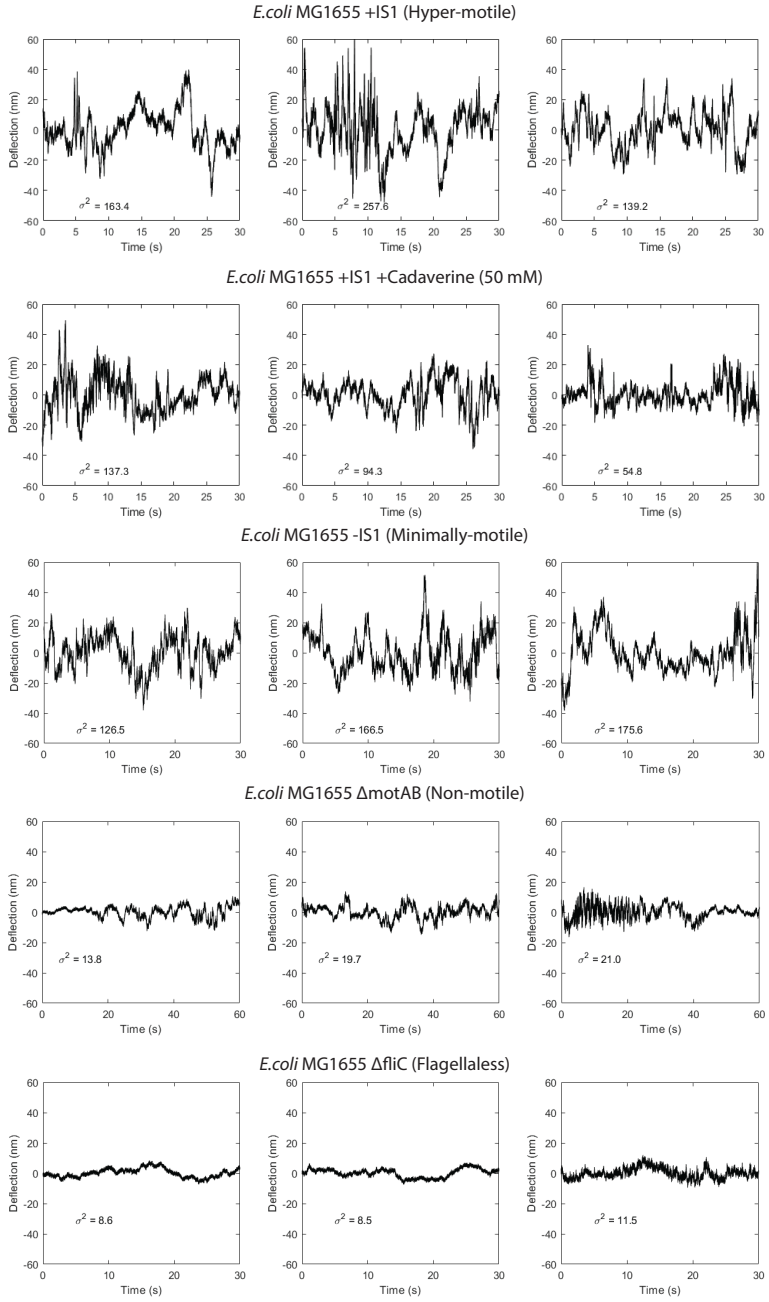

Figure 3.8: Impact of motility on observed nanomotion, extended graphs to Figure 3.3 in the main text. Each graph shows a measurements performed on single *E. coli*.

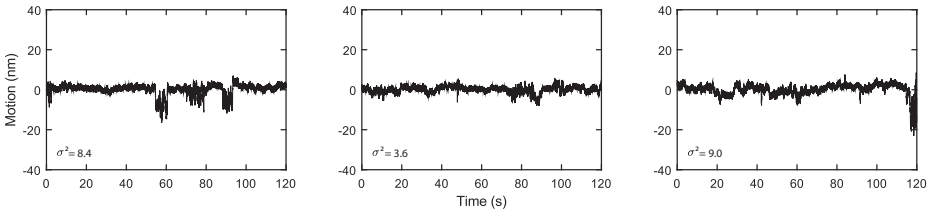

Figure 3.9: Nanomotion of gram-positive non-motile *B.subtillis*, that shows median nanomotion $\sigma^2 = 8$ nm^2. Each graph shows a measurement performed on single *B.subtillis*.

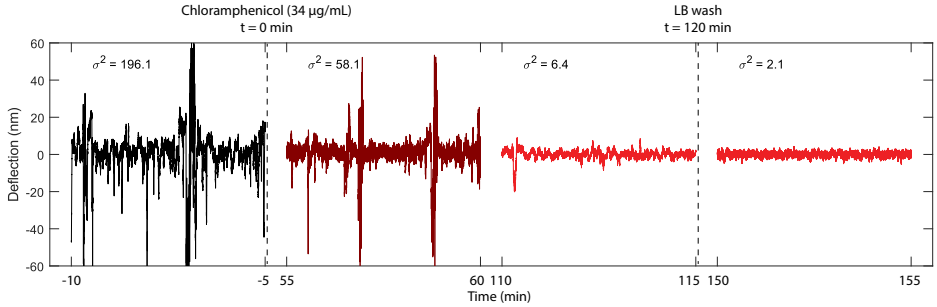

Figure 3.10: Cell are not viable after treatment with antibiotics. Each trace represents a measurement of 5 minutes performed on the same drum containing an MG1655 *E. coli*, initially (black), 1 and 2 hours after administering antibiotic (colored dark red and red), and 1 hour after flushing with LB (red). The red traces show much lower signal, which does not become higher after flushing out the antibiotic and replacing with fresh LB, which proofs that the cells lost viability. The chamber was flushed with 10 times the chamber volume to ensure that the antibiotics were cleared out from the liquid.

EXTENDED MEASUREMENT DATA - ANTIBIOTICS

To ensure that the bacteria are not viable after antibiotic treatment, we have performed a measurement in which the the chamber is flushed with fresh LB after treatment with an antibiotic. First, we recorded the motion of hyper-motile *E. coli* and treated it with chloramphenicol, observing the motion decay. Then, we removed the antibiotic by flushing 10 times the chamber volume with fresh LB. After the LB flush, the nanomotion does not increase again, which can be observed in Figure 3.10. This experiment shows that the bacteria are not viable after antibiotic treatment.

Furthermore, time traces are presented for *E. coli* treated with A22. The variance was found to be similar to that of the untreated cells (Figure 3.11). This means that disrupting cell wall synthesis does not kill the cell, and unlike all the other physiological processes that were blocked by the antibiotics it did not result in a significant change in the nanomotion. We note that in the case of A22, the cells were grown in the presence of the antibiotic before deposition on the graphene, and the alteration of the cell wall synthesis was first confirmed by optical microscopy as the bacteria are clearly rounded and have lost their typical rodshape, however, the cells still grow and divide.

In this supplement we also include extended data to Figure 3.4 in the main text, showing three more nanomotion traces for each of the antibiotics used on *E. coli* AB1157.

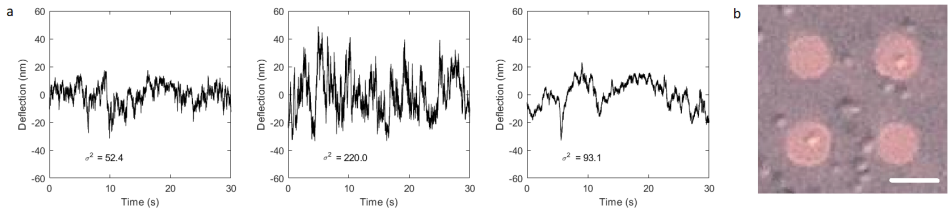

Figure 3.11: Impact of cell wall synthesis on observed nanomotion, extended graphs to Figure 3.4 in the main text. a) Each graph shows a measurements performed on *E. coli* pre-treated with A22. Nanomotion is similar to that of untreated *E. coli* AB1157, which indicates that the antibiotic did not kill the bacterium. Moreover, it tells that correct cell wall synthesis is not required to record nanomotion. b) Optical microscope imaging shows that the *E. coli* has lost its typical rod-shape after treatment with A22 and is now round. Scalebar is 10 μm.

Each graph in Figure 3.12 represents two measurements performed on the same drum, before and after administering antibiotics. It is evident that for antibiotics to which *E. coli* is sensitive, the amplitude of oscillations decreases after exposition to the drug. We also see a clear difference between live and dead bacteria in the PSD, as shown in Figure 3.13.

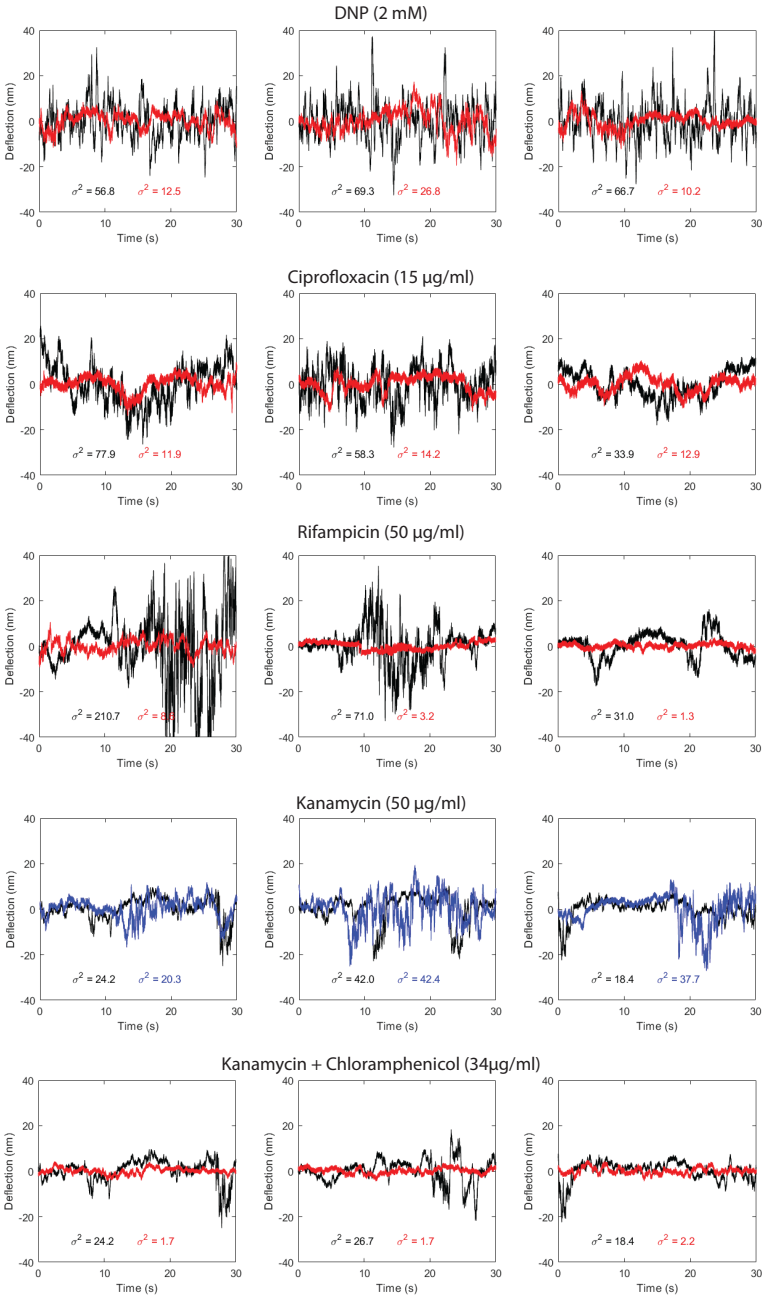

Figure 3.12: Single cell antibiotic sensitivity testing using graphene. Each graph shows two measurements performed on the same drum on *E. coli*, initially (black), and 1 hour after administering antibiotic (colored red and blue). The red traces show much lower signal, whereas blue traces do not show significant difference with respect to the original trace.

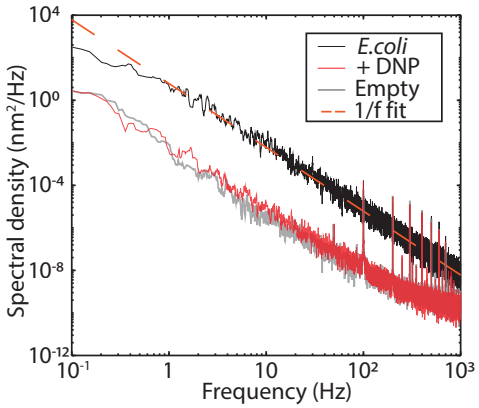

Figure 3.13: Amplitude power spectral density (PSD) of a bacterium treated with DNP (red) with respect to the data for a live bacterium (black) and for the baseline from an empty drum (grey). After treatment with DNP, the PSD of the dead bacterium drops down to the background noise level. This figure is similar to Figure 3.2b in the main text.

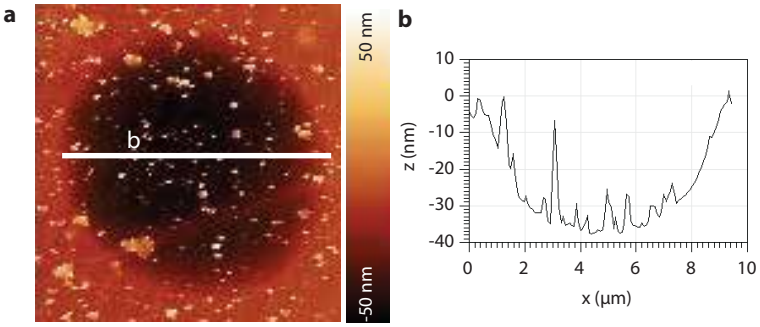

Figure 3.14: Liquid AFM characterization of a graphene drum a) AFM image of the sample. b) Line scan across the drum, as indicated by a white line in a), shows a maximum deflection of 35 nm.

LIQUID AFM MEASUREMENT

The graphene drums were also characterized in liquid using atomic force microscopy (AFM). As shown in Figure 3.14, the drums were intact and were bulging down by pressure. We find that the drums deflect by typically 35 to 60 nm, depending on the sample. Figure 3.15 shows a bacterium adhered to the surface of the suspended graphene drum.

MEASUREMENT ON EXFOLIATED GRAPHENE

For comparison to the CVD bilayer graphene used in all other experiments in this study, we show here a long measurement on an exfoliated graphene flake (thickness <10 nm). The nanomotion was recorded during 10 minutes before administering DNP at a concentration of 2 mM at the point indicated in Figure 3.16. After a few minutes that are needed for settlement and re-alignment, measurements were continued. After 30 minutes from drug injection, the amplitude of nanomotion begins to decrease. This experi-

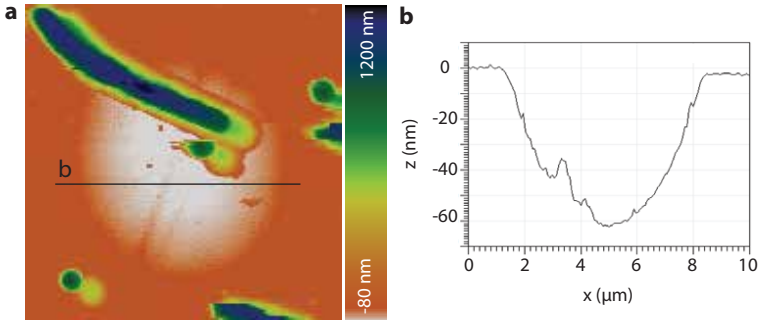

Figure 3.15: Liquid AFM characterization of a graphene drum with a deposited bacterium a) AFM image of the sample. b) Line scan across the drum, as indicated by a black line in a), shows a maximum deflection of 60 nm.

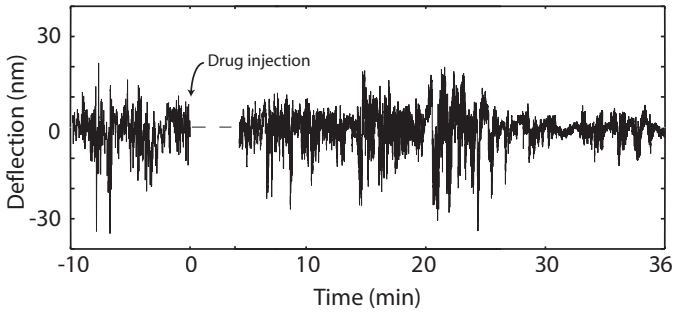

Figure 3.16: Measurement of *E. coli* nanomotion with exfoliated graphene before and after adding DNP antibiotic.

ment indicates, that also 2D materials other than CVD bilayer graphene can be suitable candidates for nanomotion detection.

BIBLIOGRAPHY

[1] Glass, L. & Mackey, M. From clocks to chaos: the rhythms of life. (Princeton University Press,1988), http://catdir.loc.gov/catdir/description/prin021/87032803.html

[2] Longo, G., Alonso-Sarduy, L., Rio, L., Bizzini, A., Trampuz, A., Notz, J., Dietler, G. & Kasas, S. Rapid detection of bacterial resistance to antibiotics using AFM cantilevers as nanomechanical sensors. *Nat Nanotechnol.* **8**, 522-6 (2013), https://www.ncbi.nlm.nih.gov/pubmed/23812189

[3] Kohler, A., Venturelli, L., Longo, G., Dietler, G. & Kasas, S. Nanomotion detection based on atomic force microscopy cantilevers. *The Cell Surface.* **5** (2019)

[4] Venturelli, L., Kohler, A., Stupar, P., Villalba, M., Kalauzi, A., Radotic, K., Bertacchi, M., Dinarelli, S., Girasole, M., Pesic, M., Bankovic, J., Vela, M., Yantorno, O.,

Willaert, R., Dietler, G., Longo, G. & Kasas, S. A perspective view on the nanomotion detection of living organisms and its features. *J Mol Recognit*. pp. e2849 (2020), https://www.ncbi.nlm.nih.gov/pubmed/32227521

[5] Jülicher, F. Mechanical oscillations at the cellular scale. *Comptes Rendus De L'Académie Des Sciences-Series IV-Physics-Astrophysics*. **2**, 849-860 (2001)

[6] Ruggeri, F., Mahul-Mellier, A., Kasas, S., Lashuel, H., Longo, G. & Dietler, G. Amyloid single-cell cytotoxicity assays by nanomotion detection. *Cell Death Discovery*. **3**, 17053 (2017), https://doi.org/10.1038/cddiscovery.2017.53

[7] Willaert, R., Vanden Boer, P., Malovichko, A., Alioscha-Perez, M., Radotić, K., Bartolić, D., Kalauzi, A., Villalba, M., Sanglard, D., Dietler, G., Sahli, H. & Kasas, S. Single yeast cell nanomotions correlate with cellular activity. *Science Advances*. **6**, eaba3139 (2020), https://advances.sciencemag.org/content/advances/6/26/eaba3139.full.pdf

[8] Kohler, A., Venturelli, L., Kannan, A., Sanglard, D., Dietler, G., Willaert, R. & Kasas, S. Yeast Nanometric Scale Oscillations Highlights Fibronectin Induced Changes in C. albicans. *Fermentation*. **6**, 28 (2020), https://dx.doi.org/10.3390/fermentation6010028

[9] Cadart, C., Venkova, L., Recho, P., Lagomarsino, M. & Piel, M. The physics of cell-size regulation across timescales. *Nature Physics*. **15**, 993-1004 (2019), https://doi.org/10.1038/s41567-019-0629-y

[10] Li, M., Xi, N., Wang, Y. & Liu, L. Advances in atomic force microscopy for single-cell analysis. *Nano Research*. **12**, 703-718 (2019)

[11] Martínez-Martín, D., Fläschner, G., Gaub, B., Martin, S., Newton, R., Beerli, C., Mercer, J., Gerber, C. & Müller, D. Inertial picobalance reveals fast mass fluctuations in mammalian cells. *Nature*. **550**, 500-505 (2017), https://dx.doi.org/10.1038/nature24288

[12] Krieg, M., Fläschner, G., Alsteens, D., Gaub, B., Roos, W., Wuite, G., Gaub, H., Gerber, C., Dufrêne, Y. & Müller, D. Atomic force microscopy-based mechanobiology. *Nature Reviews Physics*. **1**, 41-57 (2019), https://doi.org/10.1038/s42254-018-0001-7

[13] Arbore, C., Perego, L., Sergides, M. & Capitanio, M. Probing force in living cells with optical tweezers: from single-molecule mechanics to cell mechanotransduction. *Biophysical Reviews*. **11**, 765-782 (2019)

[14] Otto, O., Rosendahl, P., Mietke, A., Golfier, S., Herold, C., Klaue, D., Girardo, S., Pagliara, S., Ekpenyong, A., Jacobi, A., Wobus, M., Töpfner, N., Keyser, U., Mansfeld, J., Fischer-Friedrich, E. & Guck, J. Real-time deformability cytometry: on-the-fly cell mechanical phenotyping. *Nature Methods*. **12**, 199-202 (2015), https://dx.doi.org/10.1038/nmeth.3281

[15] Bennett, I., Pyne, A. & McKendry, R. Cantilever Sensors for Rapid Optical Antimicrobial Sensitivity Testing. *ACS Sensors*. **5**, 3133-3139 (2020), https://doi.org/10.1021/acssensors.0c01216

[16] Syal, K., Iriya, R., Yang, Y., Yu, H., Wang, S., Haydel, S., Chen, H. & Tao, N. Antimicrobial Susceptibility Test with Plasmonic Imaging and Tracking of Single Bacterial Motions on Nanometer Scale. *ACS Nano*. **10**, 845-52 (2016), https://www.ncbi.nlm.nih.gov/pubmed/26637243

[17] Steeneken, P., Dolleman, R., Davidovikj, D., Alijani, F. & Zant, H. Dynamics of 2D Material Membranes. *2D Materials*. **8** (2021)

[18] Rosłoń, I., Dolleman, R., Licona, H., Lee, M., Šiškins, M., Lebius, H., Madauß, L., Schleberger, M., Alijani, F., Zant, H. & Steeneken, P. High-frequency gas effusion through nanopores in suspended graphene. *Nature Communications*. **11**, 6025 (2020), https://doi.org/10.1038/s41467-020-19893-5

[19] Davidovikj, D., Slim, J., Cartamil-Bueno, S., Zant, H., Steeneken, P. & Venstra, W. Visualizing the Motion of Graphene Nanodrums. *Nano Letters*. **16**, 2768-2773 (2016), https://doi.org/10.1021/acs.nanolett.6b00477

[20] Lissandrello, C., Inci, F., Francom, M., Paul, M., Demirci, U. & Ekinci, K. Nanomechanical motion of Escherichia coli adhered to a surface. *Appl Phys Lett*. **105**, 113701 (2014), https://www.ncbi.nlm.nih.gov/pubmed/25316924

[21] Barker, C., Pruss, B. & Matsumura, P. Increased motility of Escherichia coli by insertion sequence element integration into the regulatory region of the flhD operon. *Journal Of Bacteriology*. **186**, 7529-7537 (2004)

[22] Leatham, M., Stevenson, S., Gauger, E., Krogfelt, K., Lins, J., Haddock, T., Autieri, S., Conway, T. & Cohen, P. Mouse Intestine Selects Nonmotile flhDC Mutants of Escherichia coli MG1655 with Increased Colonizing Ability and Better Utilization of Carbon Sources. *Infection And Immunity*. **73**, 8039-8049 (2005), https://journals.asm.org/doi/abs/10.1128/IAI.73.12.8039-8049.2005

[23] Sowa, Y., Rowe, A., Leake, M., Yakushi, T., Homma, M., Ishijima, A. & Berry, R. Direct observation of steps in rotation of the bacterial flagellar motor. *Nature*. **437**, 916-919 (2005)

[24] Bremer, E., Silhavy, T. & Weinstock, G. Transposable lambda placMu bacteriophages for creating lacZ operon fusions and kanamycin resistance insertions in Escherichia coli. *Journal Of Bacteriology*. **162**, 1092-1099 (1985), https://journals.asm.org/doi/abs/10.1128/jb.162.3.1092-1099.1985

[25] Karczmarek, A., Baselga, R., Alexeeva, S., Hansen, F., Vicente, M., Nanninga, N. & Den Blaauwen, T. DNA and origin region segregation are not affected by the transition from rod to sphere after inhibition of Escherichia coli MreB by A22. *Molecular Microbiology*. **65**, 51-63 (2007)

[26] Japaridze, A., Gogou, C., Kerssemakers, J., Nguyen, H. & Dekker, C. Direct observation of independently moving replisomes in Escherichia coli. *Nature Communications*. **11**, 1-10 (2020)

[27] Wu, F., Japaridze, A., Zheng, X., Wiktor, J., Kerssemakers, J. & Dekker, C. Direct imaging of the circular chromosome in a live bacterium. *Nature Communications*. **10**, 2194 (2019), https://doi.org/10.1038/s41467-019-10221-0

[28] Wang, X. & Sherratt, D. Independent Segregation of the Two Arms of the *Escherichia coli ori* Region Requires neither RNA Synthesis nor MreB Dynamics. *Journal Of Bacteriology*. **192**, 6143-6153 (2010), https://journals.asm.org/doi/abs/10.1128/JB.00861-10

[29] Visscher, K., Schnitzer, M. & Block, S. Single kinesin molecules studied with a molecular force clamp. *Nature*. **400**, 184-189 (1999), https://doi.org/10.1038/22146

[30] Ryu, W., Berry, R. & Berg, H. Torque-generating units of the flagellar motor of Escherichia coli have a high duty ratio. *Nature*. **403**, 444-447 (2000), https://doi.org/10.1038/35000233

[31] Mandadapu, K., Nirody, J., Berry, R. & Oster, G. Mechanics of torque generation in the bacterial flagellar motor. *Proceedings Of The National Academy Of Sciences*. **112**, E4381-E4389 (2015), https://www.pnas.org/content/pnas/112/32/E4381.full.pdf

[32] Barrett, T., Mok, W., Murawski, A. & Brynildsen, M. Enhanced antibiotic resistance development from fluoroquinolone persisters after a single exposure to antibiotic. *Nature Communications*. **10**, 1-11 (2019)

[33] WHO No Time to Wait: Securing the future from drug-resistant infections. (2019)

[34] Van Belkum, A., Burnham, C., Rossen, J., Mallard, F., Rochas, O. & Dunne, W. Innovative and rapid antimicrobial susceptibility testing systems. *Nature Reviews Microbiology*. **18**, 299-311 (2020), https://dx.doi.org/10.1038/s41579-020-0327-x

[35] Cobb, R., Chao, R. & Zhao, H. Directed evolution: Past, present, and future. *AIChE Journal*. **59**, 1432-1440 (2013)

[36] Gauger, E., Leatham, M., Mercado-Lubo, R., Laux, D., Conway, T. & Cohen, P. Role of Motility and the flhDC Operon in Escherichia coli MG1655 Colonization of the Mouse Intestine. *Infection And Immunity*. **75**, 3315-3324 (2007), https://iai.asm.org/content/iai/75/7/3315.full.pdf

[37] Louise Meyer, R., Zhou, X., Tang, L., Arpanaei, A., Kingshott, P. & Besenbacher, F. Immobilisation of living bacteria for AFM imaging under physiological conditions. *Ultramicroscopy*. **110**, 1349-1357 (2010), https://dx.doi.org/10.1016/j.ultramic.2010.06.010

[38] Blake, P., Hill, E., Neto, A., Novoselov, K., Jiang, D., Yang, R., Booth, T. & Geim, A. Making graphene visible. *Applied Physics Letters*. **91**, 063124 (2007), https://aip.scitation.org/doi/abs/10.1063/1.2768624

[39] Balaev, A., Dvoretski, K. & Doubrovski, V. Refractive index of escherichia coli cells. (SPIE,2002), https://doi.org/10.1117/12.475627

[40] Liu, P., Chin, L., Ser, W., Ayi, T., Yap, P., Bourouina, T. & Leprince-Wang, Y. Real-time Measurement of Single Bacterium's Refractive Index Using Optofluidic Immersion Refractometry. *Procedia Engineering*. **87** pp. 356-359 (2014), https://www.sciencedirect.com/science/article/pii/S1877705814028653

[41] Suk, J., Piner, R., An, J. & Ruoff, R. Mechanical Properties of Monolayer Graphene Oxide. *ACS Nano*. **4**, 6557-6564 (2010), https://doi.org/10.1021/nn101781v

[42] Davidovikj, D., Alijani, F., Cartamil-Bueno, S., Van Der Zant, H., Amabili, M. & Steeneken, P. Nonlinear dynamic characterization of two-dimensional materials. *Nature Communications*. **8** (2017), https://dx.doi.org/10.1038/s41467-017-01351-4

[43] Castellanos-Gomez, A., Singh, V., Zant, H. & Steele, G. Mechanics of freely-suspended ultrathin layered materials. *Annalen Der Physik*. **527**, 27-44 (2015)

[44] Maali, A., Cohen-Bouhacina, T., Hurth, C., Jai, C., Boisgard, R. & Aimé, J. Dynamic AFM in Liquids: Viscous Damping and Applications to the Study of Confined Liquids. *Applied Scanning Probe Methods XII: Characterization*. pp. 149-164 (2009), https://doi.org/10.1007/978-3-540-85039-77

[45] Wood, T., González Barrios, A., Herzberg, M. & Lee, J. Motility influences biofilm architecture in Escherichia coli. *Applied Microbiology And Biotechnology*. **72** pp. 361-367 (2006)

4

4

MICROWELL-ENHANCED OPTICAL DETECTION OF SINGLE BACTERIA

All that is gold does not glitter,
Not all those who wander are lost.

John Tolkien

Bacteria that are resistant to antibiotics present an increasing burden on healthcare. To address this crisis, novel rapid antibiotic susceptibility testing (AST) methods are eagerly needed. Here, we present an optical AST technique that determines bacterial viability within one hour on single bacteria. The method is based on measuring the intensity fluctuations of a reflected laser focused on a bacterium that is trapped in reflective microwells. Using numerical simulations, we show that both refraction and absorption of light by the bacterium contribute to the observed signal. By administering antibiotics that kill the bacteria, we show that the variance of the detected fluctuations vanishes within one hour, indicating the potential of this technique for rapid sensing of bacterial antibiotic susceptibility. We envisage the use of this method for massively parallelizable AST tests and fast detection of antibiotic resistance in microorganisms.

This chapter has been sent to an academic journal and is currently under review.

ANTIBIOTIC resistance in microorganisms is one of the biggest challenges that mankind is facing [1]. Most common antibiotic susceptibility testing (AST) methods are based on the detection of the growth rate of the pathogenic organisms or changes in the concentration of a marker molecule in solution [2]. In a clinical setting, the commonly adapted AST methods include measurement of the turbidity of the growth solution, its carbon dioxide content, or the diameter of the inhibition zone around an antibiotic disk [3]. These methods, are the 'gold standards' in the clinic, and have been used for over half of a century for their reliable and reproducible determination of minimum inhibitory concentrations (MICs) of an antibiotic. However, such conventional methods are slow due to their dependency on the growth rate of the pathogenic microorganism. As a result, AST methods typically require between 16 to 48 hours before any results can be obtained [4], and for slowly growing pathogens, this waiting time may take up to weeks [5]. The slow growth also causes delays in determining the pathogen identity (typically by MALDI-TOF mass spectometry) [6] and prescribing the right antibiotic to the patient. Numerous studies are being conducted to shorten the time between isolation of the pathogen and performing a rapid AST test [7, 8]. The target is to prescribe antibiotics on the same day as the diagnosis, which essentially means that AST shall be performed within 8 hours or less [9], and ideally even within an hour.

Various new methods have shown potential to obtain AST results faster than traditional methods [10–12]. These include full genome screening, microfluidic-based assays [8, 13] and nanomotion based techniques [14, 15]. Many of these emerging technologies obtained positive results in a laboratory setting, but face issues in clinical practice, where low cost and high throughput are key factors. Optical phenotypic monitoring techniques, which encompass the detection of the motion of (groups of) motile pathogens, are interesting for their potential of performing AST within a few hours. In 2019, Bennett and colleagues [16] showed that bacteria passing through a laser beam shining through growth medium can induce sudden changes in the laser intensity. The authors showed that the rate of these events is correlated to the density of the bacterial suspension, via its effect on the likelihood of a cell crossing the laser beam. Although this technique is promising, at low bacterial concentrations the rate of crossing events reduces, which increases measurement times needed for collecting sufficient statistics.

Here, we present an reflectometric read-out technique to perform AST of weakly trapped motile bacteria to enhance the sensitivity of measurements. The technique detects bacterial motility via intensity variations in the laser light when bacteria cross the path of the laser beam that is reflected from a silicon surface. By patterning the surface with microwells that physically localise the bacteria near the laser focus, we demonstrate that the signal can be significantly enhanced. Finally, we show that our reflectomotric read-out system can be used for fast detection of the susceptibility of motile bacteria to antibiotics, opening a new route for rapid AST.

4.1. OPTICAL DETECTION OF SINGLE MOTILE BACTERIA

The experiments were performed on silicon samples that were placed inside a cuvette containing motile MG1655 *E.coli* in LB medium. We recorded the intensity of the reflected 633 nm He-Ne red laser light (see Methods), that was focused on the silicon surface to a spot of 4 μm in diameter, using a laser reflectometry setup as depicted in Figure

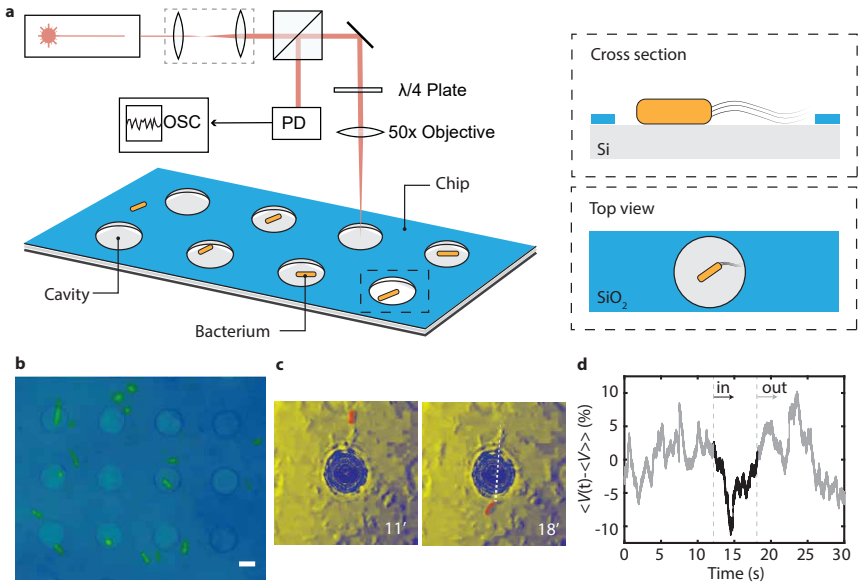

Figure 4.1: *Laser detection method for motile bacteria.*
a) Schematic illustration of interferometric read-out system and the Si/SiO_2 substrate used to localize bacteria in the pre-patterned microwells with 8 μm diameter and 285 nm depth. Bacteria on the patterned surface experience trapping, and stay longer inside the cavities than outside. b) Optical image of the fabricated microwells with fluorescent labelled bacteria, scalebar 5 micron. c) In-situ false-colored optical microscope image of a microwell with a *E.coli* cell in LB suspension crossing a laser focused on the microwell, imaged at two time points. The *E.coli* swimming path trough the microwell is indicated by a dotted white line. d) Drop in the detected signal during the bacterium crossing the laser path depicted on panel c)(signal highlighted in black). OSC: oscilloscope, PD: photodiode.

4.1. The presence of a bacterium in the focal region could be determined from the modulation of the intensity of the light that returned to the photodiode. Time-intensity data were collected for 30', and the signal variance $\sigma^2 = < (V(t) - < V(t) >)^2 >$ was used as a metric to compare various traces where the brackets stand for the time average of the photodiode signal $V(t)$.

When an *E.coli* bacterium passed through the laser focus, sudden fluctuations in the light intensity were recorded. In Figure 4.1c-d we simultaneously acquired the signal intensity and performed optical tracking of a cell (false colored in the figure). We observe sudden increased fluctuations when a bacterium crosses the laser focus. Such fluctuations were not observed when bacteria were absent (see Supplementary Note 1). In the presence of motile bacteria, the fluctuations amounted up to a ten percent of the total light intensity incident on the photodiode (see also Supplementary Note 1). Similar observations were made earlier [16] on cantilever sensors. However, when we measured on flat silicon bacteria crossed the laser focus only rarely during the 30' observation windows (see Fig. 4.2b).

To enhance signal fluctuations, we introduce micro-patterned silicon substrates, using microwells (see Fig. 4.1a) to localize the bacteria. Such microwells are known to be

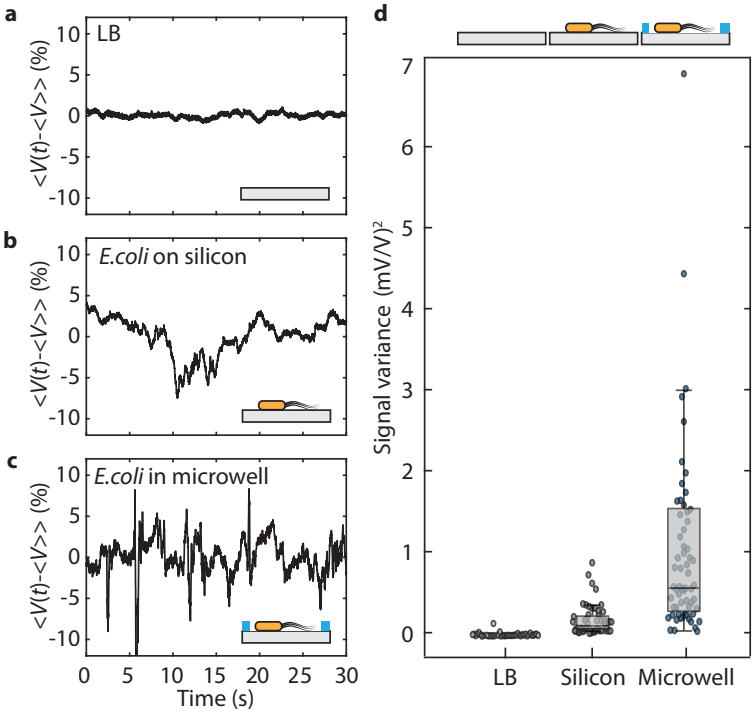

Figure 4.2: *Experiments on silicon surface and in microwells.*
a-c) Typical signals recorded in three cases: a) a control measurement on flat silicon with Lysogeny Broth (LB) without bacteria; b) on flat silicon surface with LB containing bacteria, and c) with the laser focused on a micro-well containing bacteria. Corresponding illustrations are shown in bottom right corners. d) Signal fluctuations appear only when bacteria are present, and the signal is prolonged and amplified when the surface is patterned with microwells. Measurements are collected on reflective bare silicon, both with only growth medium LB (light grey, $n = 43$) and in the presence of bacteria (dark grey, $n = 54$). Furthermore, measurements are performed on micro-patterned wells (blue, $n = 67$) in the presence of bacteria.

able to trap the bacteria for prolonged time, and can thus be used to maintain them in close vicinity of both the laser focus and the silicon surface [17]. While focusing the laser in a microwell, we observed that the signal appeared in prolonged 'bursts': periods of increased fluctuations followed by a period of relative rest. As a result, individual traces in this case showed much higher fluctuations (see Fig. 4.2c). We performed the three different experiments in LB growth medium: without bacteria on bare silicon (the control experiment), with bacteria on bare silicon, and with the laser focused on a micro-patterned cavity, typical traces are shown in Figs. 4.2a-c. Statistical analysis of the variance of each of the traces is shown in Figure 4.2d. Whereas traces on bare silicon show a variance that is only slightly higher than that in the control experiment, measurements on microwell substrates show a significantly higher variance. We thus conclude that the probability for detecting laser intensity variations due to bacteria crossing the laser path was significantly enhanced by performing the experiment in the microwells. The localization of the bacteria inside the microwells is further confirmed by microscopic imaging on transparent PDMS samples with the same geometry as the silicon (see Supplemental Note 2), in which we find a 50% higher probability of finding a bacterium inside a well than outside.

4.2. RELATION BETWEEN BACTERIUM SIZE AND READ-OUT SIGNAL

The finding that signal fluctuations are due to bacteria crossing the laser path, also suggests that the strength of the read-out signal should be dependent on the size of the bacteria. Since the laser beam is larger than the bacterium diameter, changing the bacterium shape or size is expected to also cause a different light refraction and absorption by the cell. In order to test this hypothesis, we measured the signal of shape-manipulated *E.coli* cells. We grew the bacteria in the presence of low doses of A22 [18] and Cephalexin [19], which change the cells into spherical and tubular shapes respectively.

In Figure 4.3a-b *E.coli* bacteria with different sizes are compared. Normal rod-shaped *E.coli* cells had a length of 3.4 ± 0.6 micron ($n = 51$), while spherical A22 exposed cells had a diameter of 4.2 ± 0.6 ($n = 34$). The cells that are exposed to Cephalexin mainly grew along the longitudinal axis, forming tubular shapes with a length of 10 ± 2.2 ($n = 43$) microns. As expected, changes in cell shape can influence the observed signal fluctuations.

4.3. THE ROLE OF POSITION, ABSORPTION AND REFRACTION IN SIGNAL DETECTION

To obtain an understanding of the experimental observations, we consider that light intensity fluctuations can be attributed to two main sources: firstly, the absorption of the laser light by a bacterium, and secondly, refraction of light at the boundary between the bacterium and the medium. Light refracting from the bacterial cell boundary is caused by the difference in the refractive indices of the cell and the surrounding medium. Typical values of the refractive index for *E.coli* range from 1.39 ± 0.05, while values for LB medium have been reported as 1.335 ± 0.03 [20–22]. Light travelling through a bacterium is absorbed more than in the surrounding liquid, a property which is typically used in cell counting experiments by optical density (OD) measurements [23–25]. For *E.coli* cells we

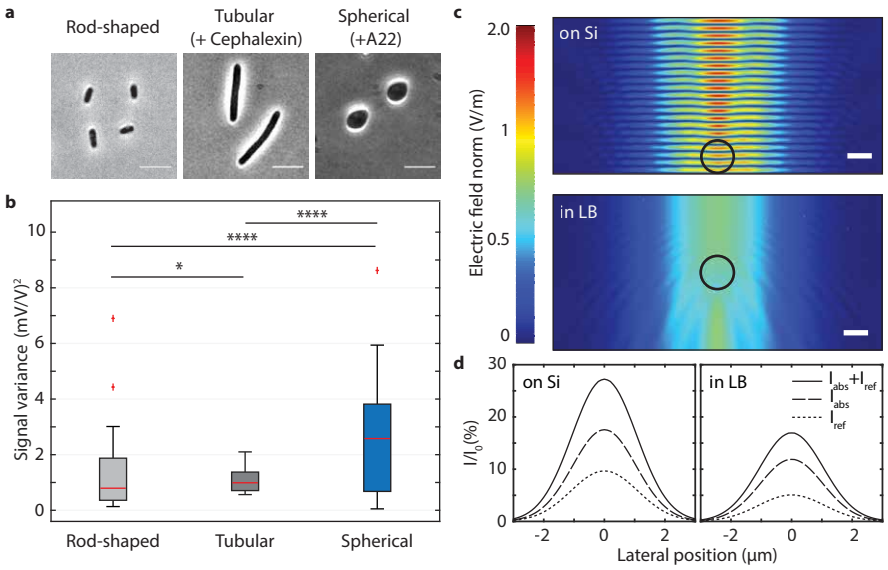

Figure 4.3: *Cell size and position determine the amount of light that is attenuated.*
a) Fluorescent microscopy images of the three different sized *E.coli* cells used in our experiments. The scalebar is 5 μm and significance is expressed using the asterisk convention. b) Measurements were performed on etched microwells with different cell sizes: normal rod shaped cells (3.4 micron in length), spherical cells (4.2 micron diameter) and long tubal cells (10 micron in length). Boxplot whiskers extend to maximum 1.5 times the inter-quartile distance and outliers are indicated with crosses. Red horizontal line represents the median values. c) Simulated electric field amplitude E of a focused 633 nm laser beam around an *E.coli* cell (indicated by a black circle) on a perfectly reflective silicon surface (top graph), and freely suspended in LB medium (bottom graph). The laser is incident from the top of the plot and the silicon surface is at the bottom of the top plot. Scalebar is 1 μm and laser beam waist is 4μm, similar to experimental conditions. d) Fraction of the incident laser power that is attenuated ($I_{\text{abs}} + I_{\text{ref}}$) by absorption ($I_{\text{abs}}$) and refraction ($I_{\text{ref}}$) as a function of the lateral position of the cell, both in case of on the reflective silicon surface (left) and freely suspended in the growth medium (right).

used an attenuation coefficient of $\mu = 1.1 \times 10^5$ m^{-1} (see Methods).

Based on these estimates, we performed COMSOL finite element simulations to explore the influence of a bacterium on the optical field and to find what portion of light is attenuated by a single bacteria passing through a focused laser beam (see also Supplementary Fig. 3). In these simulations, the distortion and intensity change of a Gaussian beam with a waist diameter of 4 μm was calculated in LB medium, both without and in the presence of an *E.coli* bacterium. In Figure 4.3c, the electric field amplitude E is shown both for the case where the bacterium is near the silicon surface and for the case that it is far from any surface, where simulations are performed in 2D and the cell is represented by a black circle. The interference between incident and reflected light waves results in a prominent standing wave near the silicon surface. In the absence of the silicon substrate there is no standing wave and the refraction caused by the bacterium alone can be observed more clearly. This calculation is repeated for various positions of the cell relative to the laser, to simulate a bacterium swimming through the centre of the beam

(see also Supplementary Note 3). Furthermore, we calculated the absorption of the electric field I_{abs} by the bacterium for all lateral positions by integrating the power loss p over the cell area A, $I_{abs} = \int_A pA$, which is shown in Figure 4.3d as a percentage of the total incoming optical power I_0. We also computed the amount of radiation I_{ref} that is refracted by an angle greater than 45 degrees (the limit due to the numerical aperture of the lens), i.e. the light not returning to the detector, again as a function of the lateral position of the bacterium. Outside of the laser beam, obviously, the bacterium does not absorb or refract light. In the center of the laser beam though, up to 18 % of the incoming light is absorbed and up to 10 % is refracted if the bacterium is on the silicon surface. In experiments, typical oscillations are 10% and the highest variations we observe are 20% of the total signal amplitude, which suggests that both absorption and refraction by the cells play a role. Notably, in most cases in our experiments, the cells did not cross the beam exactly in the middle and hence the reported values should be regarded as an upper limit for the absorption and refraction values. Besides the fact that it is impossible to focus the laser to a small spot size throughout the liquid, the bacteria close to the silicon surface yield a signal that is twice higher than freely in LB (see Figure 4.3d).

4.4. ANTIBIOTIC SUSCEPTIBILITY OF SINGLE CELLS

Finally, to see if this method can be applied for testing the efficacy of antibiotics, we compared the signal of live bacteria on bare silicon and on patterned microwells, to the signal after exposure to chloramphenicol, an antibiotic that blocks protein synthesis [26] and ciprofloxacin, an antibiotic that blocks the activity of DNA gyrases [27]. In Figure 4.4, the signal variances before and after administering the antibiotic for both cases are shown. When bacteria were swimming close to a surface patterned with microwells, in approximately one hour after the addition of antibiotics there was a significant drop in the signal. In the case when bacteria were swimming on a silicon surface, no significant change could be observed after addition of the chloramphenicol. To test the efficacy of the technique in detecting antibiotic resistance, we also performed an additional experiment on *E. coli* with *KanR* resistance gene, and did not observe a change in the variance of the signal after administering Kanamycin (see Supplementary Note 4) even after several hours of incubation, demonstrating that the technique is able to demonstrate the resistance of these bacteria against this antibioticum.

4.5. DISCUSSION AND CONCLUSION

We presented an optical detection technique to measure the viability of single bacterial cells. Our method is based on the attenuation of the laser signal when a bacteria runs through its focal plane. To extend the time during which a bacterium motility can be measured in the laser spot, we introduced microwells in the silicon surface with 285 nm depth and 8μm diameter. Because the bacteria are trapped at predetermined spots in the microwells, the bacteria stay longer near the laser spot (Figure 4.1a), and cause significantly larger signal variance.

In order to explain our experimental observations, we performed numerical studies, and concluded that the variations in the reflected signal can be explained by a combination of refraction and absorption of the laser light by the *E. coli* cell. Peak variations in

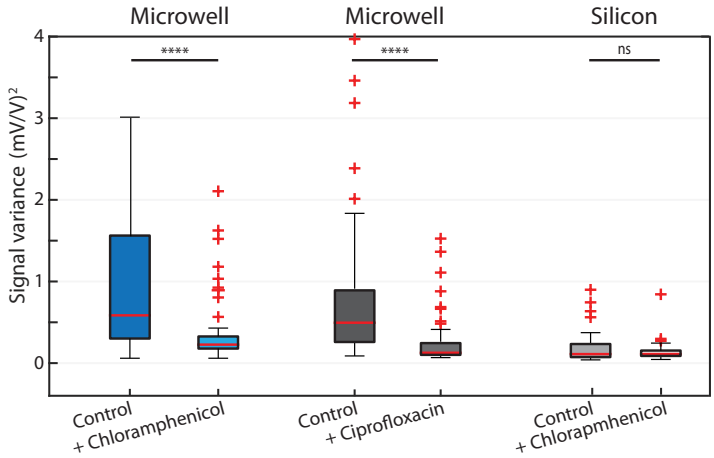

Figure 4.4: *Effect of antibiotics on the observed signal amplitude.*
Signals before and after administering various antibiotics. After 1h after administering Chloramphenicol (34μg/ml) and after 3h after administering Ciprofloxacin (20μg/ml). On the etched microwells (blue, n = 67), after administering antibiotics (chloramphenicol, light blue bars (n=67), or ciprofloxacin, dark grey bars (n=200)) a significant drop of the initial signal ($p < 10^{-5}$, ****) can be observed for susceptible bacteria. For measurements on bare silicon (grey, n = 54) no significant difference ($p = 0.94$, ns) was measured after exposure to the antibiotic (light grey, n = 54). Boxplot whiskers extend to maximum 1.5 times the interquartile distance and outliers are indicated with crosses. Red horizontal line represents the median values. Measurements are compared using a two-tailed Wilcoxon ranksum test.

signal during experiments (up to 20%) were of comparable magnitude as the maximum variations we expected based on the simulations (maximum 28%). Since the laser beam is focused with an 0.55 NA objective to a 4 μm spot, creating of conical bundle with a 46° angle, we are mostly sensitive to bacteria close to the focal point. This could partially explain the lower signal variations in our experiment. The light beam quickly spreads wider further away from the surface. For example, at 10 μm from the surface the light beam cross section is already 12.7 μm, i.e. about 10 times larger than the cross section of a typical bacterium, and the signal from a bacterium crossing far away from the focal point is reduced tenfold. Therefore, bacteria need to be close to the focal point to be detected. Moreover, finite element simulations show that near a reflective surface bacterial motion results in larger signal fluctuations than in the free volume.

The variance in measurements of the bacteria described here is directly linked to the motility of the pathogens under study. We believe that the high-speed nature of this technique could be helpful for developing rapid diagnostic tools for detection as well as AST of motile pathogens. For example, in urinary tract infections by *E.coli* (which accounts to 75% of infections) [28], we envisage our technique to be highly efficient. It is important to highlight that we could detect susceptibility to an antibiotic within hours, which is significantly quicker than existing detection techniques based on growth rate of bacteria typically taking a day [29]. The presented simulations provide a better understanding of the interaction between light and cells and of the optimal conditions for optical detection, which can further accelerate works on next-generation AST tests.

4.6. METHODS

Sample preparation. All experiments we performed on MG1655(+IS1) *E. coli* cells, described earlier [30]. Experiments with Kanamycin resistant *E.coli* cells were performed on MG1655(*kanR*) cells described earlier [15]. The *E. coli* cells, were grown in LB medium overnight at 30°C to reach the late exponential phase. The next day before performing experiment, the culture was refreshed (1:100 volume) for 2.5 hours on fresh LB medium at 30°C reach an optical density (OD600) between OD=0.2–0.3. The chamber was filled with the solution and left for 15 minutes horizontal position to deposit the bacteria on the surface. For experiments where antibiotics were used, antibiotics were dissolved in LB and incubated with bacteria for 1h. Chloramphenicol was used at 34μmg/ml, Ciprofloxacin at 20μg/ml and Kanamycin at 25μg/ml final concentration. An optical microscope (Keyence VHX-7000) was used to inspect the sample. The chamber was placed in the interferometric setup that was equipped with Attocube ECSx5050 nano positioners that allow automated scanning. The motion of the bacterium caused changes in the optical path, that were monitored by a photodiode and an oscilloscope (Rohde & Schwarz RTB2004). At each measured point on the substrate, a trace was recorded for 30 seconds with 50'000 datapoints. The measurements were performed in an air-conditioned room with a temperature of 21°C. The substrates were either 5x5 mm^2 silicon chips, or 5x5 mm^2 silicon chips with a 285 nm layer of silicon oxide. The latter were patterned with circular cavities by a reactive ion etch, where silicon acted as a stop layer, creating cavities with a diameter of 8 μm, described earlier [15].

Bacterial shape manipulation. In order to grow the *E.coli* cells into spherical shapes, low doses of the A22 drug were added to the to LB. On the day of the experiment, the cell culture was refreshed (1:100 volume) in the presence of A22 drug (5μg/ml final concentration) for 1.5 hours on fresh LB medium at 30°C reach an optical density (OD600) between OD=0.2–0.3. A22 inhibits the MreB polymerization, thereby disrupting the typical rod shape of *E. coli* [18]. These spherical cells remain physiologically active and can replicate and divide [31, 32]. In order to grow the cells into tubular shapes, low doses of cephalexin drug (25μg/ml final) were added to the to LB and cells were grown for 1 hours on fresh LB medium at 30°C. Cephalexin blocks cell division but allows cells to grow in length [19].

Optical Microscopy. To measure the sizes of *E.coli* cells we used Nikon Ti-E microscope with a 100X CFI Plan Apo Lambda Oil objective with an NA of 1.45 equipped with a phase ring. Images were captured by Andor Zyla USB3.0 CMOS Camera.

Statistics. Since the data reported in the paper are not normally distributed, we relied on non-parametric tests for statistics. We represent the median and quartiles of data in boxplots, in accordance with the use of non-parametric tests. We use a rank sum test for comparison between measurement sets. We used MATLAB's built-in functions for statistical analysis. All statistical tests were two-sided. On all figures, the following conventions are used: not significant (NS) $0.05 < P$, *$0.01 < P < 0.05$, **$0.001 < P < 0.01$, ***$0.0001 < P < 0.001$, ****$P < 0.0001$. We report a significant difference in results if $P < 0.01$.

Laser interferometry. A red laser (λ_{red} = 632.8 nm) focused with a 4 μm spot size on the sample was used for detection of the amplitude of the cell motion, where the position-dependent optical absorption of the cell results in an intensity modulation of the reflected red laser light, that was detected by a photodiode [33]. The incident red laser power was 3 mW.

Calculation of linear attenuation coefficient. The optical density (OD) of a sample is defined as the logarithm of the ratio between the incident and transmitted laser power, that is: $OD = log_{10}(I_1/I_0)$. This means that at $OD = 1$, a fraction $x = 0.1$ of the incident light is transmitted. A measurement of $OD = 1$ corresponds to approximately 10^9 bacteria /mL in a 1 cm cuvette [34].The fraction of light x that is transmitted by a single bacterium can thus be expressed as $x = (I_1/I_0)^{\sigma_c/\sigma_t}$, where σ_c is the physical cross section of the cuvette and σ_t is the total cross section of n bacterial cells in suspension with each a physical cross section σ, i.e. $\sigma_t = n\sigma$. We wish to compute the linear attenuation coefficient μ, which relates the transmitted laser power to the distance d travelled through a bacterium by the following expression: $I(d) = I_0 \cdot e^{-\mu d}$. This can be rewritten into $\mu = -ln(x)/d$. From the measured physical cross section of a single bacterium ($A \approx 1 \times 2\mu m^2$) [35] and the cross section of the cuvette ($A = 1$ cm^2), we find that a single bacterium absorbs around $x = 11\%$ of the incoming light and an attenuation coefficient of $\mu = -ln(x)/d = 1.1 \times 10^5$ m^{-1} for *E.coli* cells with average diameter $d = 1\mu$m.

Data processing. The signal obtained from the photodiode voltage due to the variations in reflected intensity of the red laser is recorded by an oscilloscope. The time trace of the photodiode voltage V_{pd}(t) was normalized by division over its average, $V_{norm}(t) = V_{pd}(t)/ < V_{pd}(t) >$, after which a linear fit was subtracted from the data to eliminate the effects of drift during the measurements.

4.7. ANNEX

In the main text the results of measurements on bare silicon and in etched wells are described. Here, we show typical traces for each of the cases as a supplement to the data presented in the main text.

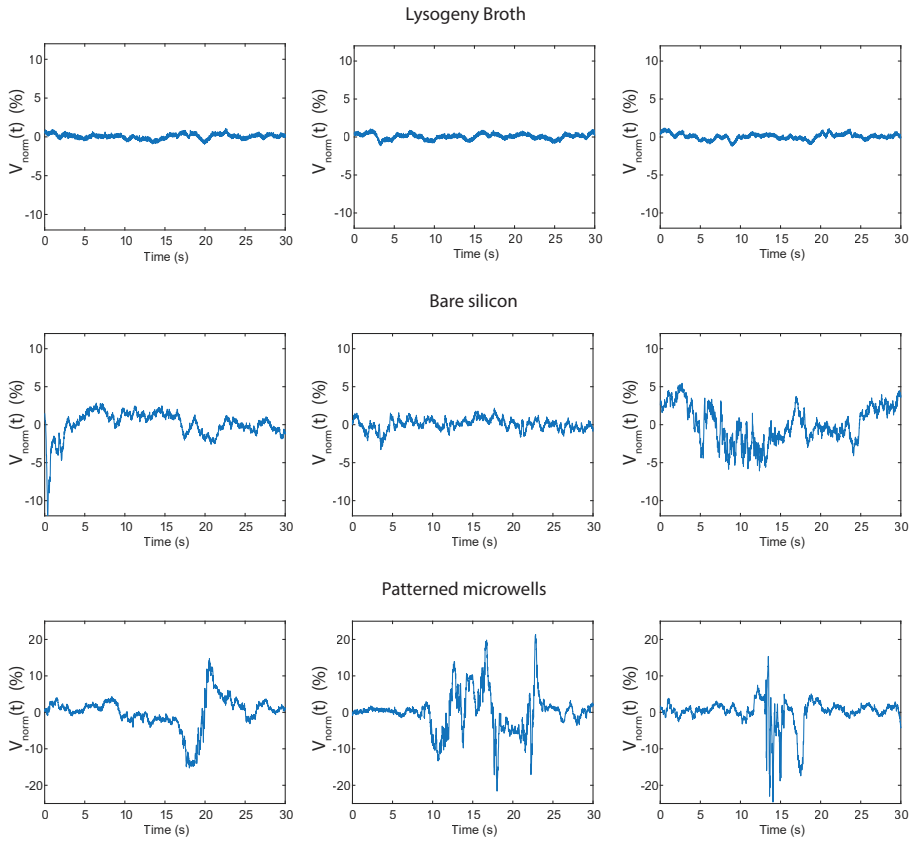

Figure 4.5: Impact of substrate on observed signal, extended graphs to figure 2 in the main text. Each graph shows a measurements performed on single position or microwell during 30 seconds.

CONFIRMATION OF WEAK TRAPPING IN WELLS BY MICROSCOPY USING TRANSPARENT PDMS PATTERNS.

PDMS substrates, with the same geometry as the silicon chips used in the main text, were prepared to validate microscopically that the cells are weakly trapped within the 285nm deep wells by measuring residence times inside the wells with respect to outside. The moulded PDMS cavities are transparent, allowing for the use of a transilumination microscope to visualize the cells. These samples were placed under a Nikon Ti-E microscope with a 100X CFI Plan Apo Lambda Oil objective with an NA of 1.45 equipped with a phase ring. Videos of 120s were recorded to observe the residence of the cells. These videos were analyzed using a MATLAB script to track the cells and compare occupation of areas inside and outside of the wells. A raw video frame and the result of the cell recognition algorithm are shown in figure 4.6a. The areas where cells are present are marked white. Then, a mask is applied to find if a cell is inside or outside of a well. For each movie frame, we calculated the cell count normalized by the mask area, $A_{\text{cell}}/A_{\text{mask}}$, both in-

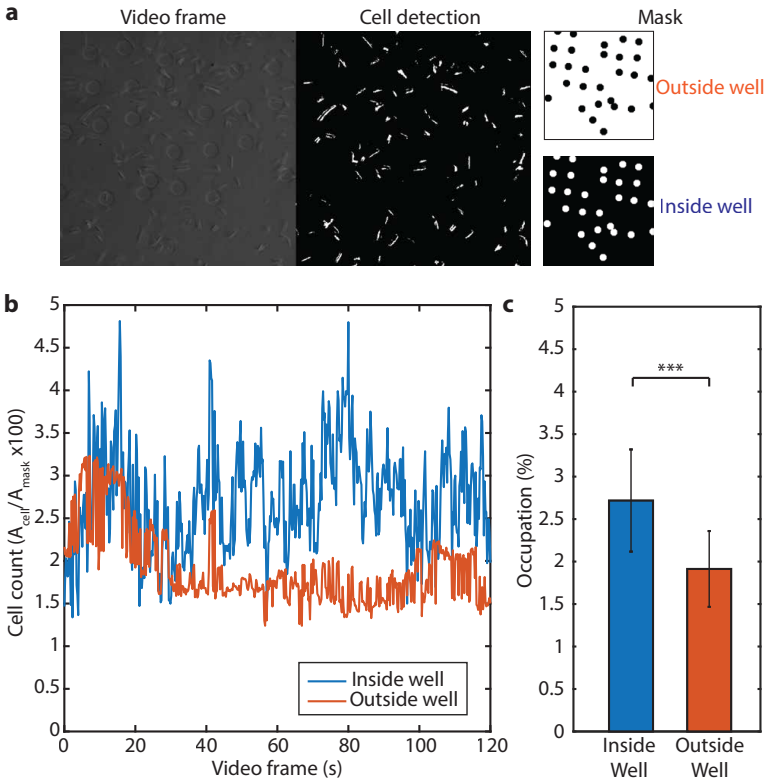

Figure 4.6: Occupation of 285nm deep PDMS wells by *E.coli* cells. a) A raw video frame and the result of the cell detection algorithm used for analysis. b) The percentage of the total area that is occupied by cells is calculated both inside and outside of wells for the entire length of the video. c) The occupation of wells is approximately 50% higher than of the surrounding area.)

side and outside of the wells, as shown in figure 4.6b and c. The occupation of wells is approximately 50% higher than of the surrounding area, confirming a weak trapping of the cells.

EXTENDED SIMULATION DATA FROM COMSOL OF A LASER BEAM TIGHTLY FOCUSED ON A BACTERIUM.

COMSOL simulations were performed to estimate the light scattered and absorbed by a single bacterium in a tightly focused beam. Here, we show several beam profiles at varying lateral position of the bacterium, which were used to obtain figure 3c and 3d in the main text.

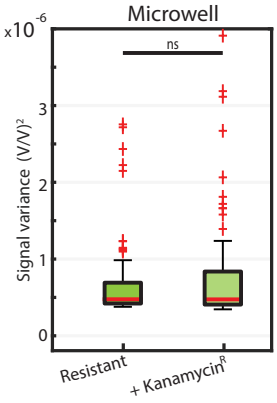

Figure 4.8: Signals before and 1 hour after administering kanamycin (25ug/ml final concentration) to MG1655(*kanR*) resistant cells. There is no signal drop observed for kanamycin resistant strains ((light green, n=84)($p = 0.53$, ns))

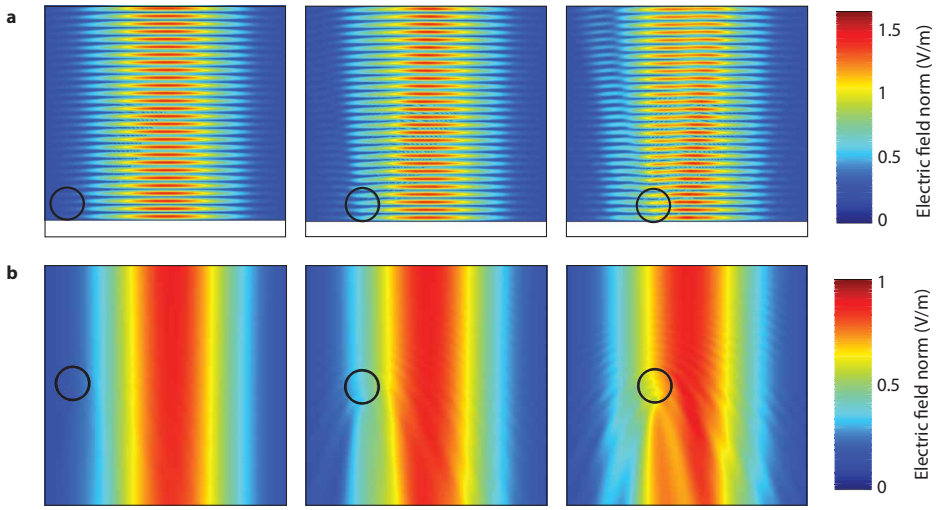

Figure 4.7: Simulation of a circular bacterium at varying lateral position with respect to a tightly focused laser beam. Extended simulation results to figure 2 in the main text are shown of the electric field norm E, at lateral positions $x = -3$,$x = -2$, and $x = -1\mu$m with respect to the centre of the beam.

DETECTING ANTIBIOTIC RESISTANCE WITH MICRO-WELLS

Experiments were performed on *E.coli* cells with a chromosomal *KanR* resistance gene exposed to Kanamycin. As it can be observed in figure 4.8, no change in the signal variance is seen after exposure to antibiotic, showing that the platform can potentially be used for fast detection of antibiotic resistance with single cell resolution.

MEASUREMENTS ON 2.5 MICRON DEEP MICRO-WELLS

We also performed experiments on deeper micro-wells to verify whether the depth might have influence on trapping. For this purpose we prepared micro-wells that are 2.5 micron deep, rather than 285 nm that was used in the main text. As it can be observed in figure 4.9, trapping events that last more than 10 seconds occur in the deeper wells, during which signal fluctuations can be recorded.

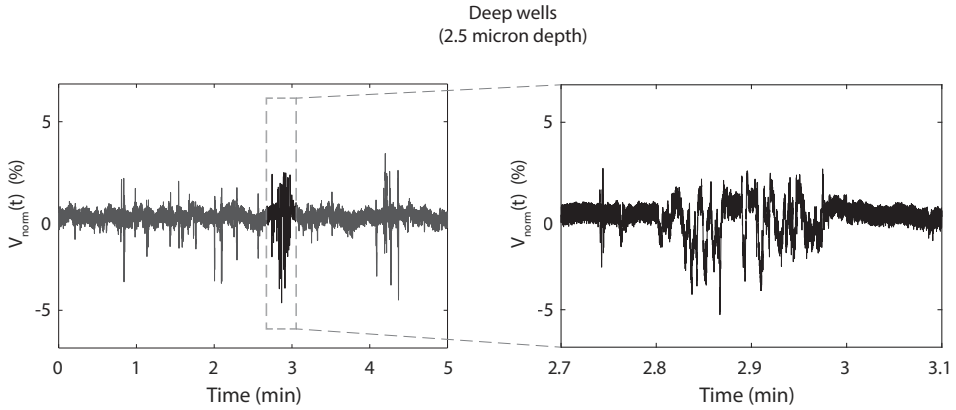

Figure 4.9: Signals recorded 2.5 micron deep microwells. The signal was recorded for 5 minutes. A trapping event is indicated on the left panel, and the signal is shown in higher detail on the right.

BIBLIOGRAPHY

[1] J. O'Neill, "Tackling drug-resistant infections globally: final report and recommendations," 2016.

[2] L. B. Reller, M. Weinstein, J. H. Jorgensen, and M. J. Ferraro, "Antimicrobial Susceptibility Testing: A Review of General Principles and Contemporary Practices," *Clinical Infectious Diseases*, vol. 49, pp. 1749–1755, 12 2009.

[3] H. Leonard, R. Colodner, S. Halachmi, and E. Segal, "Recent advances in the race to design a rapid diagnostic test for antimicrobial resistance," *ACS sensors*, vol. 3, no. 11, pp. 2202–2217, 2018.

[4] S. Puttaswamy, S. K. Gupta, H. Regunath, L. P. Smith, and S. Sengupta, "A comprehensive review of the present and future antibiotic susceptibility testing (AST) systems," *Arch Clin Microbiol*, vol. 9, no. 3, 2018.

[5] L. Hall, K. P. Jude, S. L. Clark, and N. L. Wengenack, "Antimicrobial susceptibility testing of mycobacterium tuberculosis complex for first and second line drugs by broth dilution in a microtiter plate format," *JoVE (Journal of Visualized Experiments)*, no. 52, p. e3094, 2011.

[6] T.-Y. Hou, C. Chiang-Ni, and S.-H. Teng, "Current status of MALDI-TOF mass spectrometry in clinical microbiology," *journal of food and drug analysis*, vol. 27, no. 2, pp. 404–414, 2019.

[7] G. D. Kaprou, I. Bergšpica, E. A. Alexa, A. Alvarez-Ordóñez, and M. Prieto, "Rapid methods for antimicrobial resistance diagnostics," *Antibiotics*, vol. 10, no. 2, p. 209, 2021.

[8] Ö. Baltekin, A. Boucharin, E. Tano, D. I. Andersson, and J. Elf, "Antibiotic susceptibility testing in less than 30 min using direct single-cell imaging," *Proceedings of the National Academy of Sciences*, vol. 114, no. 34, pp. 9170–9175, 2017.

[9] A. van Belkum, T. T. Bachmann, G. Lüdke, J. G. Lisby, G. Kahlmeter, A. Mohess, K. Becker, J. P. Hays, N. Woodford, K. Mitsakakis, *et al.*, "Developmental roadmap for antimicrobial susceptibility testing systems," *Nature Reviews Microbiology*, vol. 17, no. 1, pp. 51–62, 2019.

[10] A. van Belkum, C.-A. D. Burnham, J. W. Rossen, F. Mallard, O. Rochas, and W. M. Dunne, "Innovative and rapid antimicrobial susceptibility testing systems," *Nature Reviews Microbiology*, vol. 18, no. 5, pp. 299–311, 2020.

[11] F. Zhang, J. Jiang, M. McBride, X. Zhou, Y. Yang, M. Mo, J. Peterman, T. Grys, S. E. Haydel, N. Tao, *et al.*, "Rapid antimicrobial susceptibility testing on clinical urine samples by video-based object scattering intensity detection," *Analytical Chemistry*, vol. 93, no. 18, pp. 7011–7021, 2021.

[12] Z. A. Khan, M. F. Siddiqui, and S. Park, "Current and emerging methods of antibiotic susceptibility testing," *Diagnostics*, vol. 9, no. 2, p. 49, 2019.

[13] R. M. Humphries, "Update on susceptibility testing: genotypic and phenotypic methods," *Clinics in Laboratory Medicine*, vol. 40, no. 4, pp. 433–446, 2020.

[14] L. Venturelli, A.-C. Kohler, P. Stupar, M. I. Villalba, A. Kalauzi, K. Radotic, M. Bertacchi, S. Dinarelli, M. Girasole, M. Pešić, *et al.*, "A perspective view on the nanomotion detection of living organisms and its features," *Journal of Molecular Recognition*, vol. 33, no. 12, p. e2849, 2020.

[15] I. E. Rosłoń, A. Japaridze, P. G. Steeneken, C. Dekker, and F. Alijani, "Probing nanomotion of single bacteria with graphene drums," *Nature Nanotechnology*, pp. 1–6, 2022.

[16] I. Bennett, A. L. Pyne, and R. A. McKendry, "Cantilever sensors for rapid optical antimicrobial sensitivity testing," *ACS sensors*, vol. 5, no. 10, pp. 3133–3139, 2020.

[17] C. Probst, A. Grünberger, W. Wiechert, and D. Kohlheyer, "Polydimethylsiloxane (PDMS) sub-micron traps for single-cell analysis of bacteria," *Micromachines*, vol. 4, no. 4, pp. 357–369, 2013.

[18] A. Varma and K. D. Young, "In Escherichia coli, MreB and FtsZ direct the synthesis of lateral cell wall via independent pathways that require PBP 2," *Journal of bacteriology*, vol. 191, no. 11, pp. 3526–3533, 2009.

[19] N. Maki, J. E. Gestwicki, E. M. Lake, L. L. Kiessling, and J. Adler, "Motility and chemotaxis of filamentous cells of Escherichia coli," *Journal of Bacteriology*, vol. 182, no. 15, pp. 4337–4342, 2000.

[20] B. Gul, S. Ashraf, S. Khan, H. Nisar, and I. Ahmad, "Cell refractive index: Models, insights, applications and future perspectives," *Photodiagnosis and Photodynamic Therapy*, vol. 33, p. 102096, 2021.

[21] K. Stevenson, A. F. McVey, I. B. Clark, P. S. Swain, and T. Pilizota, "General calibration of microbial growth in microplate readers," *Scientific reports*, vol. 6, no. 1, pp. 1–7, 2016.

[22] A. E. Balaev, K. Dvoretski, and V. A. Doubrovski, "Refractive index of Escherichia coli cells," in *Saratov Fall Meeting 2001: Optical Technologies in Biophysics and Medicine III*, vol. 4707, pp. 253–260, SPIE, 2002.

[23] P. Liu, L. Chin, W. Ser, T. Ayi, P. Yap, T. Bourouina, and Y. Leprince-Wang, "An optofluidic imaging system to measure the biophysical signature of single waterborne bacteria," *Lab on a Chip*, vol. 14, no. 21, pp. 4237–4243, 2014.

[24] P. Y. Liu, L. Chin, W. Ser, H. Chen, C.-M. Hsieh, C.-H. Lee, K.-B. Sung, T. Ayi, P. Yap, B. Liedberg, *et al.*, "Cell refractive index for cell biology and disease diagnosis: past, present and future," *Lab on a Chip*, vol. 16, no. 4, pp. 634–644, 2016.

[25] Y. P. Liu, *Refractive Index Distribution of Single Cell and Bacterium Usingan Optical Diffraction Tomography System*. PhD thesis, Université Paris-Est, 2016.

[26] O. Pongs, R. Bald, and V. A. Erdmann, "Identification of chloramphenicol-binding protein in Escherichia coli ribosomes by affinity labeling," *Proceedings of the National Academy of Sciences*, vol. 70, no. 8, pp. 2229–2233, 1973.

[27] D. C. Hooper and G. A. Jacoby, "Topoisomerase inhibitors: fluoroquinolone mechanisms of action and resistance," *Cold Spring Harbor perspectives in medicine*, vol. 6, no. 9, p. a025320, 2016.

[28] A. L. Flores-Mireles, J. N. Walker, M. Caparon, and S. J. Hultgren, "Urinary tract infections: epidemiology, mechanisms of infection and treatment options," *Nature reviews microbiology*, vol. 13, no. 5, pp. 269–284, 2015.

[29] A. Vasala, V. P. Hytönen, and O. H. Laitinen, "Modern tools for rapid diagnostics of antimicrobial resistance," *Frontiers in Cellular and Infection Microbiology*, vol. 10, p. 308, 2020.

[30] E. J. Gauger, M. P. Leatham, R. Mercado-Lubo, D. C. Laux, T. Conway, and P. S. Cohen, "Role of motility and the flhDC operon in Escherichia coli MG1655 colonization of the mouse intestine," *Infection and immunity*, vol. 75, no. 7, pp. 3315–3324, 2007.

[31] F. Wu, A. Japaridze, X. Zheng, J. Wiktor, J. W. Kerssemakers, and C. Dekker, "Direct imaging of the circular chromosome in a live bacterium," *Nature communications*, vol. 10, no. 1, pp. 1–9, 2019.

[32] A. Japaridze, C. Gogou, J. W. Kerssemakers, H. M. Nguyen, and C. Dekker, "Direct observation of independently moving replisomes in Escherichia coli," *Nature communications*, vol. 11, no. 1, pp. 1–10, 2020.

[33] A. Castellanos-Gomez, R. van Leeuwen, M. Buscema, H. S. van der Zant, G. A. Steele, and W. J. Venstra, "Single-layer MoS2 mechanical resonators," *Advanced Materials*, vol. 25, no. 46, pp. 6719–6723, 2013.

[34] B. Volkmer and M. Heinemann, "Condition-dependent cell volume and concentration of Escherichia coli to facilitate data conversion for systems biology modeling," *PloS one*, vol. 6, no. 7, p. e23126, 2011.

[35] M. Riley, "Correlates of smallest sizes for microorganisms," in *Size limits of very small microorganisms: proceedings of a workshop*, vol. 3, p. 21, National Academies Press Washington DC, USA, 1999.

5

5

GRAPHENE DRUMS AS SENSORS OF INDIVIDUAL BACTERIA – OPPORTUNITIES AND CHALLENGES FOR APPLICATION

I'll hold onto the world tight someday.
I've got one finger on it now; that's a beginning.

Ray Bradbury

Graphene drum enabled nanomotion detection can play a central role in probing life at micro and nanoscale. By combining micro and nanomechanical systems with optics, nanomotion sensors have bridged the gap between mechanics and cellular biophysics, and have allowed investigation of processes involved in metabolism, growth, and structural organisation of a large class of micro-organisms, ranging from neurons to colonies of bacterial cells. Using graphene drums these processes can now potentially be resolved at the single-bacteria level. In this perspective, we discuss the key achievements of nanomotion spectroscopy, and peek forward into the prospects for application of this single-cell technology in clinical settings. Furthermore, we discuss the steps required for implementation and look into applications beyond bacterial sensing.

This chapter is to be published in an academic journal.

INTRODUCTION

SINCE the discovery of cells by Robert Hooke and Antoni van Leeuwenhoek, mankind's understanding of biological systems at the cellular level has kept pace with the progress in microscopic tools to observe and study such systems. It is not surprising that advancements such as cryogenic electron-microscopy [1] and fluorescence microscopy [2] were pivotal in the development of cellular science. Yet, the observation of organelles and cellular processes *in vivo* remains a significant challenge [3], since certain processes in cells cannot be easily visualized due to their small amplitudes and high levels of noise.

In this light, the recent realization that even single-cellular organisms generate small mechanical fluctuations with a broad spectrum of frequencies, might be viewed as a next step in our technical advancement of studying cellular processes. Inspired by the Atomic Force Microscopy (AFM) experiments performed by Longo and colleagues [4], who revealed that populations of living bacterial cells (100-1,000 cells) generate nanomotion on cantilever sensors, in our lab we developed the tools to use graphene drums as sensors [5] capable of recording the beating of even individual bacteria. In short, our nanomotion sensors encompass an ultra-thin suspended two-dimensional (2D) membrane with relatively low stiffness ($k = 0.1$ N/m) that is sensitive enough to transduce forces as small as a picoNewtons - even in the oxygenated liquid environment that is required to keep the cells alive. We showed that when alive, single-bacteria emit small nanometer-scale vibrations that can be recorded by these nanomechanical sensors. Such vibrations might provide insight into the metabolic activity and processes taking place inside a single cell.

In this perspective paper we first highlight the scientific achievements of the nanomotion technique, especially when applied to single cells. We then address the prospects for application of single-cell nanomotion technology in clinical settings, where it can enable Rapid Antibiotic Susceptibility Testing (RAST), by demonstrating the feasibility of graphene based RAST, on single-cell nanomotion signals from clinical isolates of five different species. Next, we highlight the challenges in performing high-throughput graphene based RAST for leveraging their extreme sensitivity to its full extent, and discuss application of alternative read-out techniques and materials for single-cell nanomotion sensors. Finally, we summarize the wide range of possibilities to use this technology in various fields beyond bacterial sensing, ranging from probing fundamental biophysical processes responsible for the generation of nanomotion to yeast activity monitoring and protein force sensing.

5.1. RECENT ADVANCES IN NANOMOTION SPECTROSCOPY

Nanomotion spectroscopy consists of attaching micro-organisms to a mechanical structure and measuring the nanoscale vibrations that the organism induces [6]. Cantilever sensors have been first used to detect the nanomotion of groups of bacteria, but also of various other cells, such as yeasts and eukaryotes [7]. The technique attracted particular interest for screening of slowly growing pathogens [8]. The cantilever is moved by the forces produced by the live specimen (Figure 5.1), and the deflection is recorded via the reflection of a laser on a 4-quadrant photo diode or through coupling with fibre optics [9].

Recently, a new method has been introduced for probing nanomotion of single bac-

teria. By using suspended graphene drums [5], the mechanical time-amplitude data trace of a single bacterium adhered to the drum can be obtained using laser interferometry (Figure 5.1b,c). In this technique, the vibrations induced by the single bacterium moves the mechanical receiver which in turn changes the optical characteristics of the cavity underneath the graphene. As a result, the drum displacement can be read-out optically by measuring the intensity of the reflected light. Schematics of both setups can be seen in Figure 5.1 alongside a typical drum deflection trace caused by a single bacterium. In approximation, the deflection δx then depends on the force F exerted by the bacterium on the flexible support, $F \approx k\delta x$, where the out-of-plane stiffness k of the flexible support determines the sensitivity.

Graphene drums Graphene drums have interesting properties that make them candidates to play the role of flexible support for nanomotion enabled activity detection. They are ultra-thin, are virtually mass-less, have very low stiffness but at the same time have high tensile strength which prevents them from breaking under tension from the liquid environment [10]. Important aspects for further improvement of this kind of detection method are threefold: first, the size of the sensitive area needs to match the object of interest. By matching the size of the detector to that of the specimen, effects of background environmental signals can be minimized. The displacement detector also needs to be highly compliant (i.e. have low mechanical stiffness). A low stiffness allows the detector to be easily moved by any external impetus, therefore increasing the minimal detectable force. Finally, appropriate optical properties are required in order to translate the microbial motion effectively into a readable signal. A perfect device for nanomotion detection combines these characteristics in the most efficient manner. For this reasons, we have rationalized that graphene sensors are an ideal candidate to play the role of flexible support for noise enabled nanomotion detection, owing to the ultimately thin nature of graphene, its low stiffness but simultaneously high tensile strength which prevents it from breaking under high tension.

Data analysis The typical approach for analysing nanomotion time data consists of two steps, of which the first is a drift subtraction. Typically, this is done by subtracting a linear fit from the raw data, over a range of several seconds to minutes. Subsequently, the data is plotted or analyzed, for which the variance σ^2 is most commonly used as metric [11, 12], although more elaborate metrics have also been conceived [6]. In nanomotion-based bacterial motility and viability testing, the change in variance is generally expressed with respect to a control sample. That means, that changes and differences in nanomotion are compared to a reference value of the variance exhibited by this control sample.

Cantilevers are generally covered by high densities of bacteria, such that the recorded signal is high enough to be detected, consisting of typical ensemble averages of 100 to 1000 cells. This makes it difficult to discern specific signals from single cells, but does provide an average representation of an entire population, especially when incubation times are prolonged. This may allow for the detection, in real-time, of bacterial variants such as persisting cells. On the other hand, by obtaining a distinctive signal from single cells, not only could we start using nanomotion for identification and analysis of mix-

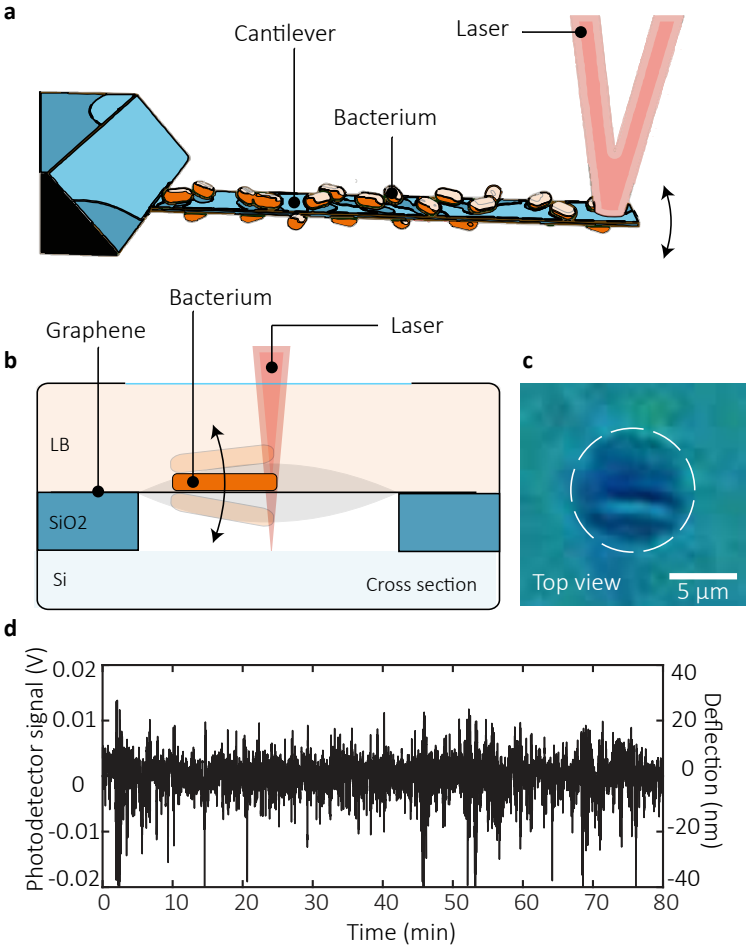

Figure 5.1: Nanomotion of bacterial cells was first detected by measuring groups of cells adhered to cantilever sensors (a). b) With graphene drums, it is possible to observe the nanomotion of even single bacterial cells. c) An optical image of a bacterial cell attached to a graphene drum. The drum is outlined by a dashed white circle. d) Nanomotion signal obtained by measuring a single cell for more than an hour. Large oscillations occur with an amplitude of up to 40 nm. Figures adapted from [5, 11].

tures, but it would also allow us to look deeper into the cellular mechanisms that cause this variance. Two studies have performed Fast Fourier Transform (FFT) analysis of the cellular signals and found a $1/f^{\alpha}$ type of signal, which is more common among biological samples [5, 13]. Despite the apparent similarity of the signals at first sight, it is an area worth exploring to see if more intricate signal analysis techniques can distinguish or identify different cells solely by the emitted nanomotion.

5.2. ROAD TO APPLICATION IN CLINICAL SETTING

Accurate identification and Antibiotic Susceptibility Testing (AST) of bacteria is crucial for clinical microbiology laboratories to guide appropriate treatment and infection control. However, culture-based AST methods, which are commonly used, are time-consuming, require one or more days to identify resistant pathogens and even longer to provide antibiotic susceptibility profiles [14]. In parallel, incubation periods in blood culture systems commonly range from 1 day to 3 days [15]. An additional challenge is that some pathogenic bacteria are fastidious, which means that they are micro-organisms that are difficult to impossible to grow in laboratory conditions because they have complex or restricted nutritional and environmental requirements, such as bacteria from the *Legionella* or the *Bartonella* genera [16]. As a result, broad-spectrum antibiotics are often administered to patients, while physicians still await AST results.

The implementation of faster wide-spectrum AST technologies will have a large impact on clincal outcomes [17]. This is because early and precise differential diagnosis of infections is critical for reducing morbidity and mortality of patients, as well as for reducing healthcare costs [18]. In the long-term, it leads to a societal benefit of reduced development of antibiotic resistance by making sure the right antibiotic is given for for the correct duration and with the right formulation. Applications of nanomotion spectroscopy in clinical setting as RAST sensors [19] is of great interest, and might even lead to simultaneous identification and susceptibility testing of bacteria, reducing the time and resources required for the testing process. Most importantly, a key challenge lies in the robustness and throughput levels of such a technique before it can be widely introduced in clinical practice.

Industrial landscape Current wide-scale operating platforms such as the bioMérieux Vitek 2 and the BD Phoenix already generate relatively rapid results (typically in 10-18h), but require a standardized microbial sample, which still requires culturing of the specimen for 24-48h after identification of the pathogen [20]. There are multiple platforms under development for rapid AST technologies, with time to result below 6 hours [21]. Optical detection platforms, such as Gradientech and BacteriScan, are the most similar to the widespread systems already in use in clinical practice [22, 23]. These platforms optically determine turbidity changes of the incubated sample and generate AST results within 3 hours. However, these new platforms do not have the ability to perform simultaneous identification or test directly on non-urine samples.

Another branch of emerging technologies bases its rapid AST on bacterial DNA extraction and subsequent genomic testing, such as the platforms of GenomeKey and Day Zero Diagnostics [24, 25]. This approach is suitable for simultaneous identification and

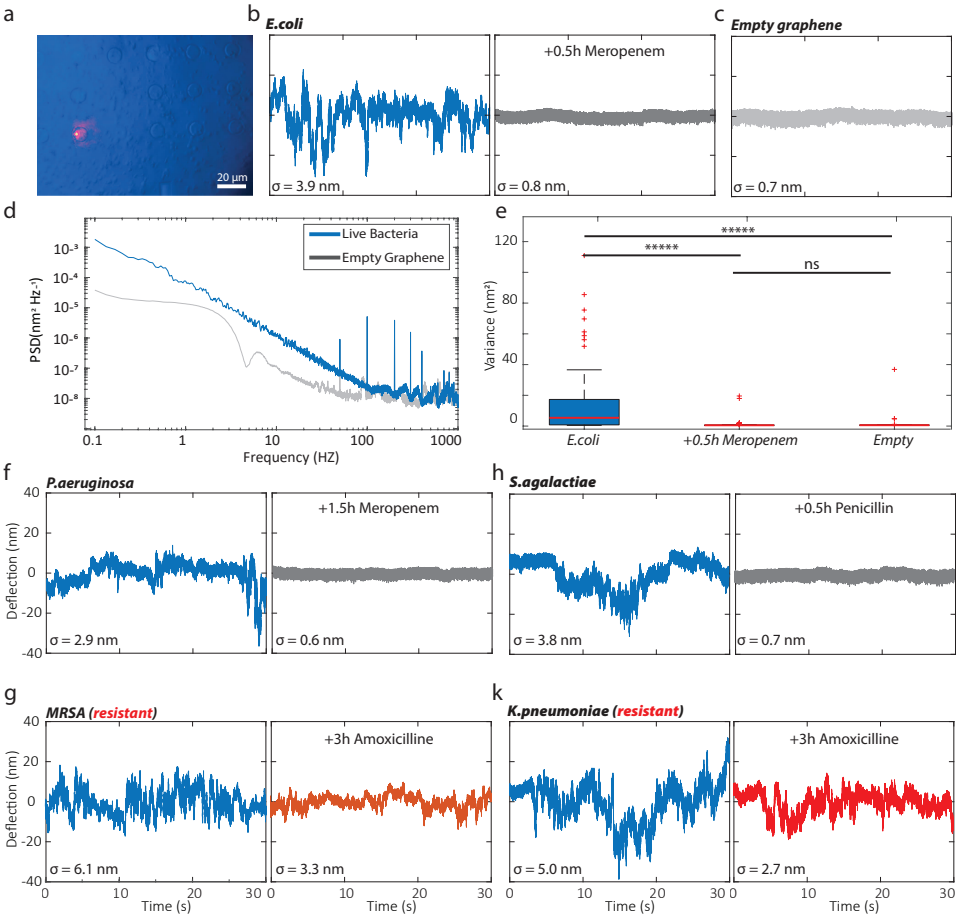

Figure 5.2: Experiments on clinical isolates of various bacteria species. (a) a snapshot of the RAST sample showing graphene drums in the presence of bacteria; (b) nanomotion from clinical isolates of *E.coli* before and after adding Meropenem; (c) nanomotion of an empty graphene drum ; (d) comparison between power spectral density (PSD) of a graphene drum with and without bacteria; (e) Box plot showing the statistical analysis performed on a number of graphene drums with and without antibiotic. The statistical data are collected from 80 measurements; (f) nanomotion of clinical isolates of *P.Aeruginosa* before and after adding Meropenem; (h) nanomotion of clinical isolates of *S.agalactiae* before and after adding Penicilin; (g) nanomotion of *MRSA* before and after adding Amoxicillin; (h) nanomotion of *K.Pneumoniae* before and after adding Amoxicillin.For each species a 30s initial trace is shown in blue, followed by a trace in gray (susceptible) or red (resistant) recorded after administering a bactericidal concentration of the antibiotic. Meropenem was used at a final concentration of 1 μg/mL, Penicillin at 0,125 μg/mL, and Amoxicillin at 60 μg/mL. The value of motion amplitude σ is shown next to each trace.

susceptibility testing at an increased throughput, and might offer a way to work directly with non-purified specimens if sufficient sensitivity is achieved. Genomic techniques rely on a library of DNA sequences encoding the resistance, which need to be known upfront to allow for detection of a resistance. However, genes are not necessarily expressed, which might lead to disagreements between genomic and culture AST results.

Nanomotion spectroscopy techniques are under development by SoundCell and Resistell, from which the latter is currently conduction clinical test in a tertiary-care hospital [26]. Resistell is developing a cantilever based nanomotion method whereas SoundCell bases the readout on graphene drums. These technologies might provide rapid AST within 2 hours as well as simultaneous identification and susceptibility testing, but increasing throughput would require microfluidics accommodating multiple cantilevers or arrays of drums.

Trials on clinical strains Here, we show the applicability of the graphene RAST on different classes of clinically relevant bacterial strains. We performed measurements on isolates of *Escherichia coli, Klebsiella pneumoniae, Methicillin-resistant Staphylococcus aureus (MRSA), Streptococcus agalactiae* and *Pseudomonas aeruginosa*. By this selection we covered strains that have the highest frequency of incidence and high prevalence of both infection and resistances [27]. These species covered both gram negative (*E. coli, P. aeruginosa , K. pneumoniae*) and positive (MRSA , S.agalactiae), as well as motile and non-motile strains. For each species, we confirm the presence of nanomechanical fluctuations (Figure 5.2). The obtained nanomotion signals were processed following the procedure outlined above and discussed in [5] which involves calculating the variance σ^2 of the signal, or its motion amplitude σ, which is a measure of bacteria viability before and after adding an antibiotic. A high value of σ means the bacteria are metabolically active and alive, while a value close to baseline, that is nanomotion of the suspended graphene alone (see 5.2c), means they are not. In Figure 5.2d, we also show the difference in the power spectral density (PSD) of drum with and without bacteria, which are clearly different.

In all cases we added various antibiotics close to the breakpoint values (1 μg Meropenem at 1 μg/mL for *E. coli* and *P.Auruginosa*, Penicillin at 0,125 μg/mL for *S.agalactiae*, and Amoxicillin at 60 μg/mL for *MRSA* and *K.Pneumoniae* (both highly resistant strains), and remeasured the same cells after just half an hour to two hours. For cases where the strains were susceptible, even within half an hour a significant signal drop was observed (see Figure 5.2b-h). The signals recorded on susceptible cells after adding antibiotics were indistinguishable from that of an empty graphene drum, indicating that these antibiotics were indeed effective. Importantly, when the experiments were performed with resistant strains (see Figure 5.2g,k) no significant changes were observed. Even after 3 hours of exposure to the drug, the cells still displayed nanomotion significantly higher than the background signal.

Single-cell diagnostics hold the promise of unprecedented precision and turnaround time [28], and in this respect graphene-based nanomotion RAST has a great potential as it may work on samples from clinical isolates, and yields results within mere hours. However, the current graphene RAST technology requires highly skilled personnel for the preparation of the clinical samples, and only one sample at a time can be tested. Fur-

thermore, the trial was performed on clinical isolates with prior identification of species. The development of a RAST platform, thus, requires realization of further steps in terms of high-throughput and lowered manual labour demand from operating personnel.

5.3. OUTLOOK AND DIRECTIONS FOR DEVELOPMENT

Further technical developments of the technique are foreseen in this section, such as nanomotion pattern based cell recognition and alternative read-out techniques for realizing high-throughput sensing. At a more fundamental level, all the root causes of nanomotion have not been untangled yet, despite there's a clear indication that flagellar activity contributes significantly to single bacterium nanomotion [5]. Possible further mechanisms that can be held accountable for nanomotion signals are also looked into in this section.

Parallel read-out with high speed and high throughput To bring single-cell nanomotion spectroscopy into clinical practice, the first step is to enhance the throughput. The read-out, for instance, can be enhanced by engineering a detection methodology for rapid detection of many graphene drums in parallel. Measuring cells one-by-one is a time consuming process and especially for screening purposes it is highly recommended to parallelize the process [29]. This challenge can be tackled by recording the signal from several drums simultaneously, either by a "scanning" over a set of drum positions, or by illuminating multiple drums and recording intensity data at once with multiple detectors (or a camera with sufficiently high frame rate). Scanning over a set of drums allows the use of a photodetector with high dynamic range, whereas the camera approach allows for massively parallelized measurements at the expense of dynamic range. Also prepared read-out cartridges could greatly simplify usage of the technology, and put lower demands on operating personnel, in turn realizing higher throughput and accuracy. Such read-out cartridges could accommodate multiple sensor chips to simultaneously test different antibiotics, at various concentrations to determine microbiologically relevant metrics such as Minimum Inhibitory Concentration (MIC). Ultimately, a measurement system might be expanded in size and throughput to screen multiple cartridges in one session, or conversely shrunk in size to be used as a random access diagnostics tool.

Machine Learning for cell identification It is of great interest whether the nanomotion signals from the drums can be used to identify various bacterial species. For instance differentiating between gram negative and gram positive species, such as *E.coli* and *S. aureus* bacteria in a fast and reliable manner would be of high importance for clinicians. This can now be achieved thanks to single-cell information that graphene nanomotion sensors do obtain [30]. In order to perform this, the use of Artificial Intelligence (AI) algorithms would be ideal. However, for such an approach to be effective, the algorithm must be first trained on a considerable amount of nanomotion data for different types of bacteria species and strains. A potential scheme to realize this vision and to identify if a sample contains resistant or susceptible bacteria, is provided in Figure 5.3a. Once the AI algorithm is trained on a large library of samples including empty drums, differ-

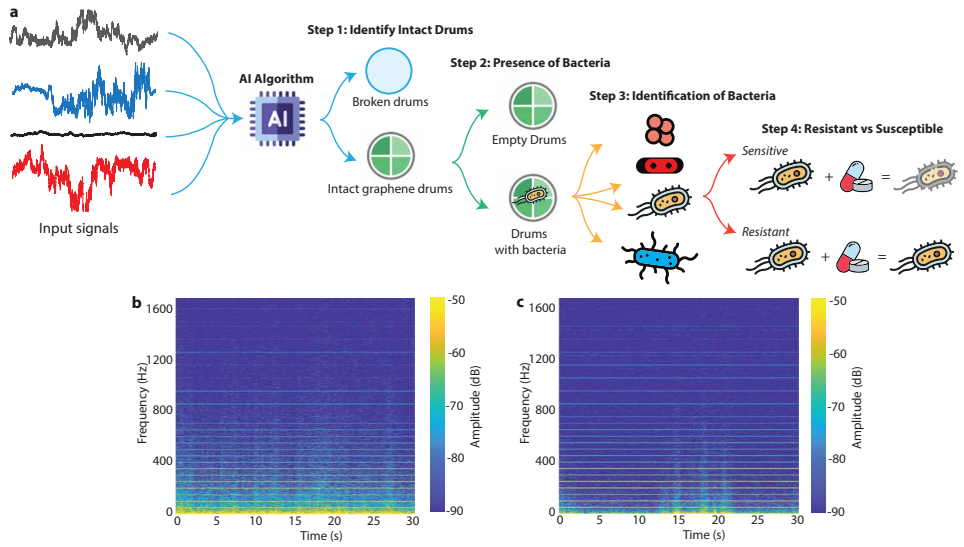

Figure 5.3: Potential process flow for combined identification and RAST based on single-cell nanomotion signals and AI algorithms. a) To determine if an unknown bacterial sample is sensitive or resistant to an antibiotic, nanomotion measurements are first to be checked upon the intactness of the drum and the presence of a bacterium. After these checks are passed, the bacterial species can be classified, and finally its resistance judged. b-c) Spectrograms obtained by applying the short-term fourier transform to nanomotion measurement traces of a control (b) and antibiotic treated (c) bacterium. The low frequency components (< 200 Hz) clearly differentiates the two spectograms. Such spectograms can be used as an input for an AI algorithm to perform swift image based classification. Horizontal lines are at multiples of 50 Hz and due to mains interference.

ent classes of bacteria as well as resistant and susceptible strains, first, a sanity check is performed to recognize if the drum is suspended and suitable for measurement. Then, the algorithm can make distinction between drums that are containing a bacterium or not. Measurements are only valuable when the drum is intact and contains a bacterium. Next, a distinction can be made on the type of bacteria based on the signal they emit. Finally, the control and antibiotic treated data can be compared to obtain a result for the susceptibility test.

First efforts on using Machine Learning for automated classification of susceptible and resistant strains has already been reported [8]. Further development might benefit from pre-processing step of the raw data, such as short-term fourier transform (STFT) analysis [31], to limit the computational effort required for swift image based classification. Figure 5.3b-c show the STFT of a control and test sample and a low frequency component on the spectogram is visible as a differentiating feature. AI is well suited for the analysis of a large volume of data to recognize such patterns that might even not be readily discernible to the human eye.

The use of AI for the identification of bacteria via signals obtained from their nanomotion is motivated by several factors. There is a high automation potential that these algorithms can offer to the process of analyzing nanomotion signals and identifying bacteria, which reduces the reliance on manual labor while increasing efficiency. AI algorithms are capable of adapting to new data and improving its accuracy over time as more data

is collected, making it a suitable tool for the dynamic field of bacterial identification.

Alternative read-out techniques and 2D material substrates In nanomotion experiments reported thus far, two kinds of optical read-out methods have been used to measure deflection of the mechanical lever. Either the angle under which an incoming beam is reflected can be measured, or the change in the reflectivity which causes a light intensity modulation. Both sifnals can be acquired with a photodiode or a high speed camera. In either case the methodology requires for the laser beam to shine through the growth medium, which provokes fierce design requirements on both the measurement chamber and the microscope in terms of materials used and environmental noise suppression, rendering it harder to use outside of academic setting.

The usage of 2D material drums on silicon allows for other read-out techniques, among which specifically electronic read-out embedded on the chip is of interest. Various schemes can be considered, such as capacitive coupling to the membrane [32], embedded strain gauging within the suspended layer [33] and even integrated photonics [34]. Such a read-out system allows the development of this technology into a self-contained lab-on-a-chip platform that includes the processing logic on-board. Such a solution would be especially interesting for point-of-care testing where simplicity and cost of use are major decisive factors [35]. Further research could also be aimed at identifying other viable 2D materials next to graphene. So far, only silicon, mono-, and bilayer graphene have been used as base material for a flexible support, yet there is plethora of different 2D materials that can be used with potential in nanomotion spectroscopy that is unknown [36].

Cell deposition and selectivity Manifold immobilization strategies exist for (targeted) attachment of living cells to a sensitive surface [37], that by themselves can enhance the quality and selectivity of the obtained signal, as long as the cell growth and viability are not hindered. Manipulating the surface characteristics of the graphene to make it selectively sticky to cells would be a development of great benefit. By patterning the adhesive substrate such that only the suspended areas of the graphene accept cells, it could be possible to improve sensitivity and work with smaller aliquots of bacterial samples. If the adhesive surface is also cell- or biomarker-specific, separate areas on one chip could be used for trapping different species. This would allow one to test even complicated samples such as direct patient samples typically containing a mixture of cells.

Probing cellular dynamics as root causes of nanomotion By probing the nanoscale motion, one could investigate which processes occur in single cells without intervening in them. Preliminary analyses of the nanomotion signals [38, 39], have suggested that flagellar activity can be a main contributor to nanomotion [5], but the correlation between the measured signal and its physical source is not unravelled yet. Various processes, such as cell viability [40], osmotic pressure fluctuations, metabolic activity and organelle mechanics might all contribute, as depicted in Figure 5.4, in addition to the environment acting as a possibly equally important contributing factor. Active ion channels transport have been shown to generate nanomotion due to their conformational changes [41]. Furthermore, in eukaryotes intracellular organelles, such as mitochondria,

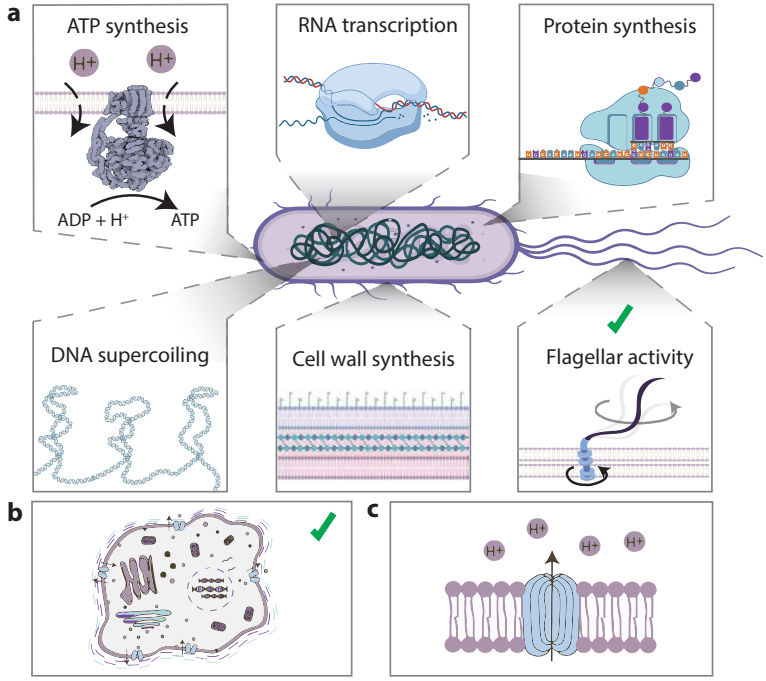

Figure 5.4: Root causes of nanomotion in bacterial cells. a) Various processes in the bacterial cell can be responsible for the mechanical nanomotion observed, such as ATP synthesis, RNA transcription, protein synthesis, DNA supercoiling, cell wall synthesis and activity of flagella and pili. Flagellar activity has been shown to be a major contributor to the observed nanomotion b) Eukaryotes contain intracellular organelles that can generate nanomotion, such as mitochondria, which are responsible for energy generation. c) Active ion channels can also generate nanomotion due to their conformational changes. Figures adapted from [5, 39].

which are responsible for energy generation, also show nanomotion [42]. Combining nanomotion with fluorescent labelled products or organelles [43] is an interesting way to further explore nanomotion causes which might lead to new insights into the root cause.

5.4. APPLICATIONS BEYOND BACTERIAL SENSING

Over the course of the past decade the nanomotion technique has been applied to various different species, and it is applied with success for bacteria, yeast, neurons, and mammalian cells. Most of the research mentioned was performed on AFM cantilevers, rather than graphene drums, the latter so far being only used for detection of single bacterial cells.

Yeasts and bio-industrial applications Yeasts are used in various biotechnological applications, ranging from food production chains to constituents of bioreactor flora [44]. They play a significant role in the industrial production of biofuels and enzymes. For all these applications, it is of major interest to verify the activity and thus productivity of

yeast strains before a bioreactor is populated. Early and massively parallel screening is a good strategy to alter and verify the quality of yeasts with a faster turnover, thus finding superior industrial traits earlier. The nanomotion that can be measured from yeasts, alike bacteria, is most likely directly linked with their metabolic activity [45]. In most cases, a higher metabolic activity will translate into a higher production of the yeast's industrially relevant compound. We envisage therefore, that by probing the nanomotion of the yeast's, the productivity of strains can be directly measured and potentially improved.

Molecular force monitoring The high force sensitivity of graphene might enable sensing beyond the limit of single cells. Some molecules are active as a result of light [46] or fold based temperature or solute concentration [47] and can perform mechanical work. It is interesting to see if graphene membranes could be used as a detector for probing the forces exerted by these molecules during mechanical events, such as DNA supercoiling or protein folding. Here, a significant challenge will lie in the preparation of such samples, and the attachment of the biomolecules onto the graphene surface.

5.5. FINAL REMARKS

In the recent decades a new revolution in cell biology is taking place due to the rapid advancements in microfabrication technology. The wide availability of micro- electromechanical systems (MEMS) since the 1990's has provided researchers a new platform to experimentally study cell mechanics and their mechanobiology. With the development of the graphene drums as sensors for single cells, it is now possible to measure and analyze cellular dynamics on the level of single bacteria. This raises thrilling prospects for usage of nanomotion detection for both identification as well as antibiotic sensceptibility analysis. In our perspective, the development of massively parallel graphene nanomotion sensors can be a gamechanger in this field. The ability to robustly run hundreds or even thousands of nanomotion spectroscopy measurements in parallel would open the way to RAST combined with nanomotion based identification. We hope that the contents of this paper will pave the way towards the developments that one day will make such technology readily available.

5.6. METHODS

Sample preparation. All experiments were performed on anonymous clinical isolates of *E.coli*, *K.Pneumoniae*, *MRSA*, *S. agalactiae* and *P. aeruginosa* cells obtained from the medical microbiology department of the Reinier Haga Medical Centre in Delft. We grew cells in Muller-Hinton Broth overnight at 30 degrees Celsius to reach the late exponential phase. On the day of the experiment, the overnight culture was refreshed (1:100 volume) for 2.5 h in fresh broth at 37 degrees Celsius to reach an optical density (OD600) of 0.2–0.3. Then 10 ml of the refreshed culture was mixed with (3-Aminopropyl)triethoxysilane (APTES, Sigma-Aldrich) to reach a final concentration of 0.1% (volumetric). This acts as a binder between the bacteria and the chips. A chamber with a graphene-covered chip inside was then filled with the solution, which was left for 15 minutes in a horizontal position to deposit the bacteria on the surface. Afterwards, the chamber was flushed

with broth to prevent additional bacteria from depositing and maintain an average coverage of a single bacterium per drum. The setup was equipped with nano positioners (Attocube ECSx5050) that allow for automated scanning over an array of drums. The motion of the bacterium was transduced on the drum and recorded using a digital oscilloscope.

Graphene chip fabrication Experiments are performed on circular suspended graphene membranes. A silicon wafer with a silicon dioxide layer is patterned by etching holes in the silicon dioxide, where the silicon acted as stop layer, resulting in 285 nm deep circular cavities with diameters ranging from 2 to 10 μm. Graphene resonators are fabricated by suspending single and few-layer graphene over circular cavities using a dry transfer technique. Both exfoliated graphene flakes and chemical vapor deposited layers are used as resonator. The samples are annealed in an Argon furnace at 400K to remove all polymer residuals. The setup consists of a red laser aimed and focused at a Fabry-Pérot cavity formed by the bottom silicon layer and the suspended graphene layer. The deflection of the graphene layer along the optical field of the red laser modulates the reflected light intensity that can be read out by a photodiode. The setup allows detection of the absolute deflection of the membrane.

Data processing All data are collected and plotted using MATLAB code. For analysis, the same routines are used as described earlier in [5]. For the short term fourier transform a custom code was written in MATLAB, with the following settings: blackman type window with a length of 2048 and an FFT length of 8192.

BIBLIOGRAPHY

[1] J. L. Milne and S. Subramaniam, "Cryo-electron tomography of bacteria: progress, challenges and future prospects," *Nature Reviews Microbiology*, vol. 7, no. 9, pp. 666–675, 2009.

[2] P. Meyer and J. Dworkin, "Applications of fluorescence microscopy to single bacterial cells," *Research in microbiology*, vol. 158, no. 3, pp. 187–194, 2007.

[3] G.-C. Yuan, L. Cai, M. Elowitz, T. Enver, G. Fan, G. Guo, R. Irizarry, P. Kharchenko, J. Kim, S. Orkin, *et al.*, "Challenges and emerging directions in single-cell analysis," *Genome biology*, vol. 18, pp. 1–8, 2017.

[4] G. Longo, L. Alonso-Sarduy, L. M. Rio, A. Bizzini, A. Trampuz, J. Notz, G. Dietler, and S. Kasas, "Rapid detection of bacterial resistance to antibiotics using afm cantilevers as nanomechanical sensors," *Nature nanotechnology*, vol. 8, no. 7, pp. 522–526, 2013.

[5] I. E. Rosłoń, A. Japaridze, P. G. Steeneken, C. Dekker, and F. Alijani, "Probing nanomotion of single bacteria with graphene drums," *Nature Nanotechnology*, vol. 17, no. 6, pp. 637–642, 2022.

[6] M. I. Villalba, L. Venturelli, R. Willaert, M. E. Vela, O. Yantorno, G. Dietler, G. Longo, and S. Kasas, "Nanomotion spectroscopy as a new approach to characterize bacterial virulence," *Microorganisms*, vol. 9, no. 8, p. 1545, 2021.

[7] S. Kasas, F. S. Ruggeri, C. Benadiba, C. Maillard, P. Stupar, H. Tournu, G. Dietler, and G. Longo, "Detecting nanoscale vibrations as signature of life," *Proceedings of the National Academy of Sciences*, vol. 112, no. 2, pp. 378–381, 2015.

[8] A. Vocat, A. Sturm, G. Jozwiak, G. Cathomen, M. Świątkowski, R. Buga, G. Wielgoszewski, D. Cichocka, G. Greub, and O. Opota, "Nanomotion technology in combination with machine learning: a new approach for a rapid antibiotic susceptibility test for mycobacterium tuberculosis," *Microbes and Infection*, p. 105151, 2023.

[9] J. Zhou, J. Huang, H. Huang, C. Zhao, M. Zou, D. Liu, X. Weng, L. Liu, J. Qu, L. Liu, *et al.*, "Fiber-integrated cantilever-based nanomechanical biosensors as a tool for rapid antibiotic susceptibility testing," *Biomedical Optics Express*, vol. 14, no. 5, pp. 1862–1873, 2023.

[10] P. G. Steeneken, R. J. Dolleman, D. Davidovikj, F. Alijani, and H. S. Van der Zant, "Dynamics of 2D material membranes," *2D Materials*, vol. 8, no. 4, p. 042001, 2021.

[11] S. Kasas, A. Malovichko, M. I. Villalba, M. E. Vela, O. Yantorno, and R. G. Willaert, "Nanomotion detection-based rapid antibiotic susceptibility testing," *Antibiotics*, vol. 10, no. 3, p. 287, 2021.

[12] P. Stupar, "Atomic force microscopy of biological systems: Quantitative imaging and nanomotion detection," tech. rep., EPFL, 2018.

[13] C. Lissandrello, F. Inci, M. Francom, M. Paul, U. Demirci, and K. Ekinci, "Nanomechanical motion of escherichia coli adhered to a surface," *Applied physics letters*, vol. 105, no. 11, p. 113701, 2014.

[14] R. Datar, S. Orenga, R. Pogorelcnik, O. Rochas, P. J. Simner, and A. van Belkum, "Recent Advances in Rapid Antimicrobial Susceptibility Testing," *Clinical Chemistry*, vol. 68, pp. 91–98, 12 2021.

[15] P. P. Bourbeau and M. Foltzer, "Routine incubation of BacT/ALERT FA and FN blood culture bottles for more than 3 days may not be necessary," *Journal of clinical microbiology*, vol. 43, no. 5, pp. 2506–2509, 2005.

[16] M. I. Villalba, P. Stupar, W. Chomicki, M. Bertacchi, G. Dietler, L. Arnal, M. E. Vela, O. Yantorno, and S. Kasas, "Nanomotion detection method for testing antibiotic resistance and susceptibility of slow-growing bacteria," *Small*, vol. 14, no. 4, p. 1702671, 2018.

[17] A. van Belkum, T. T. Bachmann, G. Lüdke, J. G. Lisby, G. Kahlmeter, A. Mohess, K. Becker, J. P. Hays, N. Woodford, K. Mitsakakis, *et al.*, "Developmental roadmap for antimicrobial susceptibility testing systems," *Nature Reviews Microbiology*, vol. 17, no. 1, pp. 51–62, 2019.

[18] J. Hrabák, E. Chudáčková, and R. Walková, "Matrix-assisted laser desorption ionization–time of flight (MALDI-TOF) mass spectrometry for detection of antibiotic resistance mechanisms: from research to routine diagnosis," *Clinical microbiology reviews*, vol. 26, no. 1, pp. 103–114, 2013.

[19] P. Stupar, O. Opota, G. Longo, G. Prod'Hom, G. Dietler, G. Greub, and S. Kasas, "Nanomechanical sensor applied to blood culture pellets: a fast approach to determine the antibiotic susceptibility against agents of bloodstream infections," *Clinical Microbiology and Infection*, vol. 23, no. 6, pp. 400–405, 2017.

[20] S. Brisse, S. Stefani, J. Verhoef, A. Van Belkum, P. Vandamme, and W. Goessens, "Comparative evaluation of the BD Phoenix and VITEK 2 automated instruments for identification of isolates of the burkholderia cepacia complex," *Journal of Clinical Microbiology*, vol. 40, no. 5, pp. 1743–1748, 2002.

[21] A. van Belkum, C.-A. D. Burnham, J. W. Rossen, F. Mallard, O. Rochas, and W. M. Dunne Jr, "Innovative and rapid antimicrobial susceptibility testing systems," *Nature Reviews Microbiology*, vol. 18, no. 5, pp. 299–311, 2020.

[22] C. Malmberg, J. Torpner, J. Fernberg, H. Öhrn, J. Ångström, C. Johansson, T. Tängdén, and J. Kreuger, "Evaluation of the speed, accuracy and precision of the QuickMIC rapid antibiotic susceptibility testing assay with gram-negative bacteria in a clinical setting," *Frontiers in Cellular and Infection Microbiology*, vol. 12, p. 311, 2022.

[23] E. Davaro, A. P. Tomaras, R. R. Chamberland, and T. S. Isbell, "Evaluation of a Novel Light Scattering Methodology for the Detection of Pathogenic Bacteria in Urine," *The Journal of Applied Laboratory Medicine*, vol. 5, pp. 370–376, 03 2020.

[24] C. Rhee, M. A. Baker, R. Tucker, V. Vaidya, M. Holtzman, R. R. Seethala, M. Bentain-Melanson, J. Lenox, A. R. Smith, J. C. Boyer, *et al.*, "Cluster of burkholderia cepacia complex infections associated with extracorporeal membrane oxygenation water heater devices," *Clinical Infectious Diseases*, vol. 75, no. 9, pp. 1610–1617, 2022.

[25] H. Elshazly, Y. Souilmi, P. J. Tonellato, D. P. Wall, and M. Abouelhoda, "MC-GenomeKey: a multicloud system for the detection and annotation of genomic variants," *BMC bioinformatics*, vol. 18, no. 1, pp. 1–14, 2017.

[26] G. Caruana, A. Kritikos, A. Vocat, A. Luraschi, E. Delarze, A. Sturm, M. P. Verge, G. Jozwiak, S. Kushwaha, J. Delaloye, *et al.*, "Investigating nanomotion-based technology (Resistell AST) for rapid antibiotic susceptibility testing among adult patients admitted to a tertiary-care hospital with gram-negative bacteraemia: protocol for a prospective, observational, cross-sectional, single-arm study," *BMJ open*, vol. 12, no. 11, p. e064016, 2022.

[27] C. J. Murray, K. S. Ikuta, F. Sharara, L. Swetschinski, G. R. Aguilar, A. Gray, C. Han, C. Bisignano, P. Rao, E. Wool, *et al.*, "Global burden of bacterial antimicrobial resistance in 2019: a systematic analysis," *The Lancet*, vol. 399, no. 10325, pp. 629–655, 2022.

[28] H. Li, K. Hsieh, P. K. Wong, K. E. Mach, J. C. Liao, and T.-H. Wang, "Single-cell pathogen diagnostics for combating antibiotic resistance," *Nature Reviews Methods Primers*, vol. 3, no. 1, p. 6, 2023.

[29] F. Pujol-Vila, R. Villa, and M. Alvarez, "Nanomechanical sensors as a tool for bacteria detection and antibiotic susceptibility testing," *Frontiers in Mechanical Engineering*, vol. 6, p. 44, 2020.

[30] S. Mendoza, "Identification of bacteria with Artificial Intelligence," *MSc thesis*, 2023.

[31] F. Demir, A. Sengur, and V. Bajaj, "Convolutional neural networks based efficient approach for classification of lung diseases," *Health information science and systems*, vol. 8, pp. 1–8, 2020.

[32] M. Šiškins, M. Lee, D. Wehenkel, R. van Rijn, T. W. de Jong, J. R. Renshof, B. C. Hopman, W. S. Peters, D. Davidovikj, H. S. van der Zant, *et al.*, "Sensitive capacitive pressure sensors based on graphene membrane arrays," *Microsystems & Nanoengineering*, vol. 6, no. 1, p. 102, 2020.

[33] L. Groo, J. Nasser, D. J. Inman, and H. A. Sodano, "Transfer printed laser induced graphene strain gauges for embedded sensing in fiberglass composites," *Composites Part B: Engineering*, vol. 219, p. 108932, 2021.

[34] Y. Su, Y. Zhang, C. Qiu, X. Guo, and L. Sun, "Silicon photonic platform for passive waveguide devices: Materials, fabrication, and applications," *Advanced Materials Technologies*, vol. 5, no. 8, p. 1901153, 2020.

[35] K. J. Land, D. I. Boeras, X.-S. Chen, A. R. Ramsay, and R. W. Peeling, "REASSURED diagnostics to inform disease control strategies, strengthen health systems and improve patient outcomes," *Nature microbiology*, vol. 4, no. 1, pp. 46–54, 2019.

[36] M. C. Lemme, S. Wagner, K. Lee, X. Fan, G. J. Verbiest, S. Wittmann, S. Lukas, R. J. Dolleman, F. Niklaus, H. S. van der Zant, *et al.*, "Nanoelectromechanical sensors based on suspended 2d materials," *Research*, vol. 2020, 2020.

[37] N. Gupta, V. Renugopalakrishnan, D. Liepmann, R. Paulmurugan, and B. D. Malhotra, "Cell-based biosensors: Recent trends, challenges and future perspectives," *Biosensors and Bioelectronics*, vol. 141, p. 111435, 2019.

[38] W. Chomicki, "Development of an AFM-based nanomotion detection device for microbiological samples," tech. rep., EPFL, 2019.

[39] A. Kohler, L. Venturelli, G. Longo, G. Dietler, and S. Kasas, "Nanomotion detection based on atomic force microscopy cantilevers," *The Cell Surface*, vol. 5, p. 100021, 2019.

[40] H. Al-Madani, H. Du, J. Yao, H. Peng, C. Yao, B. Jiang, A. Wu, and F. Yang, "Living sample viability measurement methods from traditional assays to nanomotion," *Biosensors*, vol. 12, no. 7, p. 453, 2022.

[41] L. Alonso-Sarduy, P. De Los Rios, F. Benedetti, D. Vobornik, G. Dietler, S. Kasas, and G. Longo, "Real-time monitoring of protein conformational changes using a nanomechanical sensor," *PLoS One*, vol. 9, no. 7, p. e103674, 2014.

[42] P. Stupar, W. Chomicki, C. Maillard, D. Mikeladze, A. Kalauzi, K. Radotić, G. Dietler, and S. Kasas, "Mitochondrial activity detected by cantilever based sensor," *Mechanical Sciences*, vol. 8, no. 1, pp. 23–28, 2017.

[43] M. Cieśluk, P. Deptuła, E. Piktel, K. Fiedoruk, Ł. Suprewicz, P. Paprocka, P. Kot, K. Pogoda, and R. Bucki, "Physics comes to the aid of medicine—clinically-relevant microorganisms through the eyes of atomic force microscope," *Pathogens*, vol. 9, no. 11, p. 969, 2020.

[44] J. Steensels, T. Snoek, E. Meersman, M. P. Nicolino, K. Voordeckers, and K. J. Verstrepen, "Improving industrial yeast strains: exploiting natural and artificial diversity," *FEMS microbiology reviews*, vol. 38, no. 5, pp. 947–995, 2014.

[45] R. G. Willaert, P. Vanden Boer, A. Malovichko, M. Alioscha-Perez, K. Radotić, D. Bartolić, A. Kalauzi, M. I. Villalba, D. Sanglard, G. Dietler, *et al.*, "Single yeast cell nanomotions correlate with cellular activity," *Science advances*, vol. 6, no. 26, p. eaba3139, 2020.

[46] B. Gole, B. Kauffmann, V. Maurizot, I. Huc, and Y. Ferrand, "Light-controlled conformational switch of an aromatic oligoamide foldamer," *Angewandte Chemie International Edition*, vol. 58, no. 24, pp. 8063–8067, 2019.

[47] T. L. Solomon, Y. He, N. Sari, Y. Chen, D. T. Gallagher, P. N. Bryan, and J. Orban, "Reversible switching between two common protein folds in a designed system using only temperature," *Proceedings of the National Academy of Sciences*, vol. 120, no. 4, p. e2215418120, 2023.

6

6

Outlook

POTENTIAL TOPICS FOR FURTHER RESEARCH

In the course of the research that is concluded with this thesis, I have touched upon numerous interesting aspects of forces in nature and their effects on graphene drums. Here, I intend to mention the potential areas of application that I encountered and that have shown great promise to further work on. I have split them in two branches. Concerning the interaction of graphene with micro-/nanoscale objects, I will specifically highlight nano pillar structures and milled pores for separation or sieving purposes. Concerning fluctuations and nonlinearities I will look more deeply into stochastic switching and stochastic resonance.

Depositing structures on suspended graphene Focused electron beam induced deposition (EBID) has the ability to produce nanometer scale silicon oxide based features. Here, we apply EBID with Tetraethylorthosilicaat (TEOS) as a precursor gas to locally deposit silicon dioxide. By this means we can grow tall, high features of arbitrary shape on a suspended membrane. The ability to deposit structures on membranes promises thrilling advances on both fundamental and application level. For example, single high aspect ratio pillars have been manufactured by EBID surface deposition of SiO_2 on graphene drums, see Figure 6.1a-b. Structures that are the size and shape of single bacteria could be deposited to study the mechanical interaction with the graphene membranes and understand better how the position of the bacterium impacts the signal quality.

These pillars by themselves can also provide a next generation of AFM probes, which might allow scanning in deeper trenches or even full 3D scanning. By using these suspended atomically thin graphene membranes in AFM application, one can profit from the beneficial material and geometric properties of suspended graphene. Graphene membranes are characterized by high resonant frequencies f and low Q-factor, leading to a short settling time Q/f that allows fast probe control and high scanning speeds [1]. Moreover, graphene membranes are easily driven to amplitudes at which their stiffness becomes nonlinear. Operation in this regime would lower the chances of snap-in when faced with suddenly changing surface height. We believe that this will prevent so called 'snap-in' and enable faster scanning speeds, yielding higher quality surface imaging and a better experience. We succeeded in producing a tip with a radius of 50 nm and a height of 10 μm on a suspended single layer of graphene.

Recently standing waves in graphene nanodrums have been visualized [3], giving a detailed view on the mode structure. It is of both fundamental and practical interest to extend this study towards travelling waves on the surface of atomically thin materials. Measurements of these phenomena might lead to a more complete understanding of energy transfer between degenerate modes. Practically, obtaining a travelling wave on the surface is also of interest to allow full 3D motion of structures attached onto the atomically thin layer. The setup described in this thesis can be adapted to measure the travelling wave in a two-point measurement.

Pores for separation and sieving Porous graphene offers unexplored possibilities for sieving, as discussed in Chapter 1. Besides separating particles of different sizes, porous graphene can also be used to trap the particles of interest at the location of a single pore in the membrane (Figure 6.1c). The image shows an electron micrograph of graphene

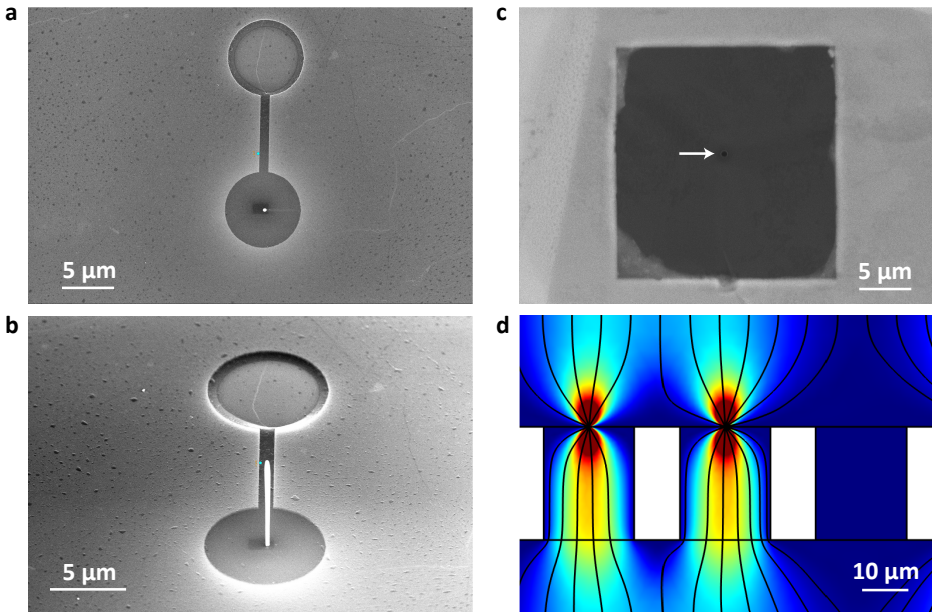

Figure 6.1: *Structures on suspended graphene devices.*
a) Electron microscope top and side view (b) of a dumbbell shaped cavity covered by bilayer graphene with a high aspect ratio pillar on the suspended graphene. The pillar is made from silicon by electron beam induced deposition (EBID). It can be inferred that the drum is still suspended by comparison with the top drum, which is collapsed. c) A nanopore with a diameter of 400 nm is milled in the graphene in the middle of a 20 micron square graphene window (pore is indicated by a white arrow). The graphene covers a single silicon through-hole, such that sieving can be performed by making a fluid flow solely through the milled perforation in the graphene. d) Schematic side-view of a device geometry that features an array of three graphene covered windows with singular holes in the centre. The side view is overlayed by a 2D COMSOL simulation of the water velocity magnitude through the device [2]. The black lines represent the flow lines and the colors represent fluid velocity. The third channel shows no flow, as it is simulated to be blocked by a trapped particle.

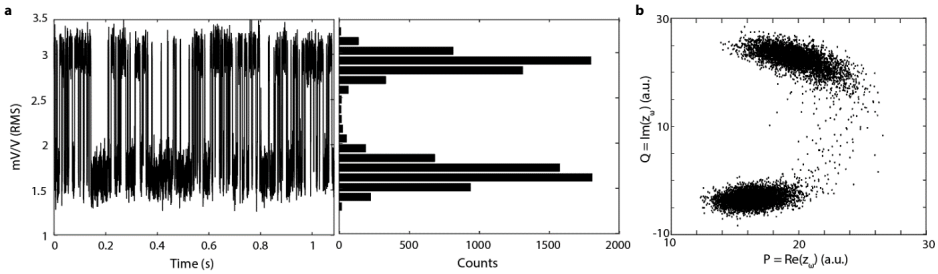

Figure 6.2: *Strongly driven graphene resonators exhibit stochastic switching.*
a) Stochastic switching between two stable equilibria with a switching frequency of 160Hz. b) Visualization of the escape paths between the stable equilibria in the phase plane.

suspended over a 20x20 μm^2 hole etched in a silicon chip. A single 200 nm wide pore is milled in the middle of the suspended graphene. An exemplary application would be to trap single bacteria at the center of drums by running a fluid through the pore, thus accelerating the screening time required for a clinical sample. Simulations of the velocity magnitude through an array of porous graphene, see Figure 6.1d, indicate how the flow might trap individual particles exactly on the pore. [2].

6

Stochastic switching and resonance By means of stochastic resonance, weak periodic signals can be amplified to a detectable level thanks to an increase of the signal to noise ratio [4]. This happens because of synergic coupling between the stochastic switching rate between the two equilibria and the frequency of the external signal. Experimental results at frequencies below 1 Hz have been previously obtained using cantilevers [5]. A strongly driven graphene resonator shows a Duffing response with two stable equilibria, that can as well be used as a platform for stochastic resonance. Weak perturbations of the resonator can consequently lead to a switch from one equilibrium to another. Figure 6.2 shows an example of such switching between the stable attractors in a strongly driven graphene resonator. The amplitude between the high and low states is translated in the difference between the two stable states rather than the actual amplitude of the signal. Therefore, otherwise unreadable subthreshold information can be amplified to a measurable level. We observe switching rates in the orders of 100 to 1000 Hz that can be tuned to obtain stochastic resonance in the audible frequency range near room temperature (see Figure 6.2).

Stochastic switching might offer a way of probing weak biological signals that would be otherwise unreadable. One possibility to amplify weak signals is to combine nonlinear dynamic effects with noise to generate stochastic resonance. Although graphene membranes in liquid are heavily damped and obtaining a mechanical duffing response seems unfeasible, it should be possible to use the optomechanical nonlinearities to engineer double-well potentials that would accomodate amplification of weak periodic signals [6, 7]. It would be interesting to see if such a concept could be used to amplify for example the nanomotion at the single bacteria level.

BIBLIOGRAPHY

[1] J. D. Adams, B. W. Erickson, J. Grossenbacher, J. Brugger, A. Nievergelt, and G. E. Fantner, "Harnessing the damping properties of materials for high-speed atomic force microscopy," *Nature nanotechnology*, vol. 11, no. 2, pp. 147–151, 2016.

[2] S. Rodenhuis, "Probing nanomotion and comparing antibiotic efficacy of a single E. coli bacterium on silicon and graphene," *Master of Science Thesis*, 2021.

[3] D. Davidovikj, J. J. Slim, S. J. Cartamil-Bueno, H. S. Van Der Zant, P. G. Steeneken, and W. J. Venstra, "Visualizing the motion of graphene nanodrums," *Nano letters*, vol. 16, no. 4, pp. 2768–2773, 2016.

[4] R. J. Dolleman, P. Belardinelli, S. Houri, H. S. van der Zant, F. Alijani, and P. G. Steeneken, "High-frequency stochastic switching of graphene resonators near room temperature," *Nano letters*, vol. 19, no. 2, pp. 1282–1288, 2019.

[5] W. J. Venstra, H. J. Westra, and H. S. Van Der Zant, "Stochastic switching of cantilever motion," *Nature communications*, vol. 4, no. 1, p. 2624, 2013.

[6] M. H. de Jong, J. Li, C. Gärtner, R. A. Norte, and S. Gröblacher, "Coherent mechanical noise cancellation and cooperativity competition in optomechanical arrays," *Optica*, vol. 9, no. 2, pp. 170–176, 2022.

[7] F. Wu, J. Halatek, M. Reiter, E. Kingma, E. Frey, and C. Dekker, "Multistability and dynamic transitions of intracellular min protein patterns," *Molecular systems biology*, vol. 12, no. 6, p. 873, 2016.